University of Alberta

Drop Removal from Solid Surfaces: Shedding and Evaporation

by

Seyed Farshid Chini

A thesis submitted to the Faculty of Graduate Studies and Research
in partial fulfillment of the requirements for the degree of

Doctor of Philosophy

Mechanical Engineering Department

Spring 2013
Edmonton, Alberta

Dedication

This thesis is dedicated to my parents who introduced me to the joy of loving from birth. Parents, you are the most precious things in my life. Mother, I will never forget the sacrifices you made. You have always believed in me and have been my inspiration in life. I thank you for your unconditional love. Father, having always been a strong support in my life, you have also been a source of motivation and strength during the moments of despair. The life lessons for which you have taught me are undeniable and irreplaceable.

I would like to thank my brother, Ali, for the many childhood memories we have shared. Ali, through the good and the bad you have always had my back. I feel supported by being around you. I would also like to dedicate this thesis to my grandparents for making my life glorious with their existence.

Finally, I would like to thank my beautiful fiancé, Mehrvash, for always being kind and lovely for me. Please never doubt my love for you.

I would also like to express a special word of thanks to my supervisor Dr. Amirfazli who tirelessly listened to my ideas and offered encouragements when it was most needed. Without his patience, understanding and support the completion of this work would have been impossible. I also expand my thanks to all my friends in Iran and Canada.

Abstract

The drop removal from solid surfaces is studied. Removal of a drop from its substrate may be gradually (*e.g*. evaporation) or all at once (*e.g*. shedding). In this thesis, drop adhesion force as a base for understanding the all at once removal of a drop from its substrate, and drop evaporation at room temperature as one of the gradual removal mechanisms are studied in detail. The drop adhesion force may be found by calculating the summation of surface tension forces along the contact line. For that a model is developed which is applicable to any shape drop as long as contact line is convex everywhere. The model developed requires the value of left and right contact angles observed in the 2-D side view images which is asymmetric. For that a method (*i.e. SPPF*) was developed to measure the contact angle of asymmetric drops. Regarding the evaporation study, as a first step and to minimize the number of parameters, evaporation of suspended micro-liter drops is studied. Evaporation of such a case is restricted by movement of vapor from the drop surface, and not the phase change. Literature studies assume the evaporation process is steady-state and convection is small (Maxwell assumptions). It is found that none of the two assumptions are valid. However, for the range of parameters for micro-liter drops, the effect of transient term cancels the effect of convection, and Maxwell assumptions yield accurate results. The convection term discussed above excludes the buoyancy which may potentially increase or decrease the convection and evaporation rate, consequently. It was found that buoyancy is not a dominant factor on evaporation of drops, and the difference between the evaporation of sessile and pendant drops has a different source (evaporation modes). Sessile drops spend longer time in the CWA (constant wetted area) mode. Evaporation is faster in that mode compared to the other mode *i.e.* the CCA (constant contact angle). Uneven evaporation flux distribution along the sessile drop surface was studied using an electrostatic analogy (exterior Dirichlet). It was found that the ratio of the evaporation rate with including the evaporation flux variation to that with neglecting the evaporation flux variation is a function of contact angle, and can be found using the following exponential relation $60.27\theta^{-0.92}$ (θ is in radians).

Acknowledgement

I would like to thank my supervisor Dr. Amirfazli for his support and kind advice. I would also like to thank Dr. Miguel Cabrerizo Vílchez at the University of Granada, Spain, to whom I had some fruitful discussions. I would also like to thank Mr. Guoping Fang and Ms. Denise Thornton for helping me debugging the developed program (SPPF). This thesis was supported by National Sciences and Engineering Research Council of Canada (NSERC) and Canada Research Chair (CRC) program.

Table of Contents

Chapter 1 – Introduction

Drop removal from solid surfaces is a challenge in various areas such as aerospace industry [1], fuel cell technology [2, 3], cleaning industries, wind turbines [4], oil recovery [5, 6], etc. Removal of a drop from its substrate may be gradually (*e.g.* evaporation) or all at once (*e.g.* shedding). In this thesis, drop adhesion force as a base for understanding the all at once removal of a drop from its substrate, and drop evaporation at room temperature as one of the gradual removal mechanisms are studied in detail.

Regarding the adhesion force, the following questions should be answered: what factors contribute to the adhesion force? What tools are needed to measure the factors affecting the adhesion force? Wenzel [7] and Cassie [8] were among the first who studied the adhesion force between a drop and its substrate. They believed that the adhesion occurs on the contact area (solid-liquid interface). Later, experiments in [9-14] rejected the Wenzel and Cassie theories in adhesion, and showed that adhesion force depends on the events at the three-phase line, *e.g.* [15, 16]. Three-phase or contact line is where liquid, air and solid phases meet, and in the case of drops on solid surfaces, it is the perimeter of the solid-liquid interface. The forces at the contact line are surface tension forces. These forces operate at the interface in the tangential direction, and are properties of the material, and a function of temperature [17]. By adding the surface tensions along the contact line the drop adhesion force is found (indirect approach), *e.g.* [18]. It should be noted that some researchers directly measured the adhesion force on drops using AFM (atomic force microscopy) [19-22]. However, direct methods are more expensive and tend to be less accurate, *e.g.* [23].

1.1 Indirect Measurement of Drop Adhesion Force

Indirect methods calculate the summation of surface tension forces along the contact line to find the adhesion force. At any point on the contact line, three operative surface tensions exist. These surface tensions at any point on the contact line lie in a plane which is perpendicular to both the substrate and to the drop contact line at that point. Young (Eq. 1-1) showed that in equilibrium state, at any point on the contact line, in the plane of the substrate, these three surface tensions balance each other as:

$$\boldsymbol{\gamma}_{\boldsymbol{SL}} + \boldsymbol{\gamma} \cos \theta_Y = \boldsymbol{\gamma}_{\boldsymbol{SV}} \tag{1-1}$$

where γ_{SL} , γ and γ_{SV} are solid-liquid, liquid-vapor and solid-vapor surface tensions, respectively; and θ_Y is the Young's or intrinsic contact angle (see Fig. 1-1a). Contact angle is the angle between the solid surface and liquid-air interface, measured through the liquid phase. It should be noted that when contact line advances or recedes on a surface, due to the surface roughness and heterogeneity, different contact angles may be observed. The largest and smallest possible contact angles on a surface are called advancing θ_A and receding θ_R contact angles, accordingly (see Fig. 1-1b). According to Eq. 1-1, in equilibrium, the summation of surface tension forces on the substrate plane and along the contact line (or adhesion force) becomes zero. Assuming the solid surface is flat and perfectly homogenous, one has $\oint_{Contact\ Line} \boldsymbol{\gamma_{SL}}\, \boldsymbol{dl} = \oint_{Contact\ Line} \boldsymbol{\gamma_{SV}}\, \boldsymbol{dl} = 0$, as integrals are along the contact line and contact line is a closed curve. As such, the only contributor to the adhesion force becomes the on the substrate plane projection of γ. If the value of contact angle along the contact line or $\theta(\varphi)$, is uniform (φ is the azimuthal angle, see. Fig. 1-1a) the summation of the projections of $\boldsymbol{\gamma}$ on the substrate plane and along the contact line becomes zero, *i.e.* $\oint_{Contact\ Line} \boldsymbol{\gamma} \cos\theta(\varphi)\, \boldsymbol{dl} = 0$.

An external force parallel to the drop substrate deforms the drop and makes the $\theta(\varphi)$ non-uniform along the contact line (*e.g.* see Fig. 1-1b); therefore, the summation of $\gamma \cos\theta(\varphi)$ along the contact line becomes non-zero, *i.e.* $\oint_{Contact\ Line} \boldsymbol{\gamma} \cos\theta(\varphi)\, \boldsymbol{dl} \neq 0$. On homogeneous surfaces, the value of $\oint_{Contact\ Line} \boldsymbol{\gamma} \cos\theta(\varphi)\, \boldsymbol{dl}$ is equal to the adhesion force. As such, the adhesion force is a function of $\boldsymbol{\gamma}$, contact line's length (l), and contact angle values along the contact line, $\theta(\varphi)$. The value of $\boldsymbol{\gamma}$ is known for different liquids. It should be noted that literature has suggested some approximate relations for calculating the adhesion force without measuring l and $\theta(\varphi)$. However, as will be shown in Chapter 2, these approximate relations are applicable only for drops with specific contact line shapes (*e.g.* circular, elliptical, parallel-sided, or contact lines with at least one axis of symmetry). For drops with arbitrary contact line shapes, the value of l and $\theta(\varphi)$ are needed to measure the adhesion force, and as will be shown below these measurements are not straight forward. In this thesis specific tools are developed for measuring the contact line's length and contact angle values.

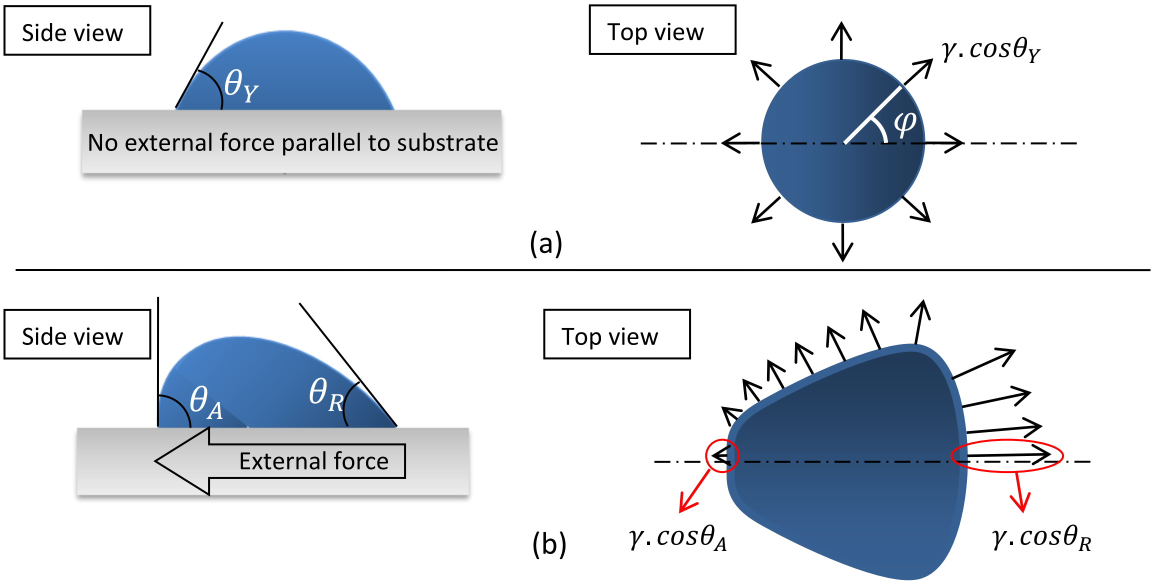

Fig. 1-1 Side and top views of drops on a smooth surface are shown where (a) no external force parallel to the substrate plane is on the drop. Contact angle along the contact line is uniform, so the summation of surface tension forces along the contact line is zero. (b) A parallel to the substrate external force is on the drop and advancing (θ_A) and receding (θ_R) contact angles are shown, the summation of surface tension forces on the drop (or adhesion force) is against the external force. Please note that the surface tensions are the ones operative on the drop and their reactions are operative on the substrate.

1.2 Contact Line's Length Measurement

Regarding the contact line's length measurement, one may think that this is a redundant task as the top view image of the drop can show the contact line.

However, the problem arises for drops with contact angles larger than 90^o where the contact line is not observable from the top view image. The only exception is for axisymmetric drops with known volume [24]. As will be shown in Chapter 2, a methodology is developed which reconstruct the contact line using the 2-D side view images, the challenge was resolving the perspective error which occurred during interpreting the 2-D side view images.

1.3 Contact Angle Measurement

As shown above the value of contact angle is needed to find the adhesion force, it is worth mentioning that the application of contact angle measurement is not limited to adhesion force measurement *e.g* [18, 25-30]. As explained briefly here and in details in Chapter 3 the challenge in measuring the contact angle is for asymmetric drops (*e.g*. Fig. 1-1b), which is the case in adhesion force measurement (axisymmetrical in this context means that the left and right side contact angles in the 2D side view image are equal). In general, contact angle measurement methods found in literature can be grouped into tensiometry and goniometry methods. As will be shown in details in Chapter 3, tensiometry methods find the Young's contact angle using Eq. 1-1. A complete list of tensiometry methods can be found in [31]. But, the observed or apparent contact angle (θ_a in Fig. 1-2) is not necessarily equal to the Young's contact angle e.g. [7, 8, 32-37] and the apparent contact angle is needed in measuring the adhesion force.

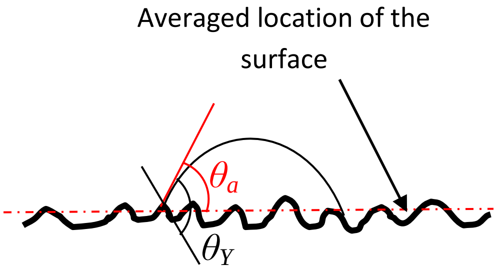

Fig. 1-2 Apparent (θ_a) and intrinsic or Young (θ_Y) contact angles on a rough surface are shown.

1.3.1 Goniometry Methods

In goniometry methods contact angle is observed and measured from the 2-D side view image of the drop on the solid surface. As such, the apparent contact angle is measured. Modern literature methods for measuring the contact angle of drops (and in general pendant and captive drops and bubbles) can be categorized into two groups: (i) analytical-image processing and, (ii) exclusively image processing methods. Both of the analytical-image processing and exclusively image processing methods are explained in details in Chapter 3. In summary, analytical-image processing methods (*e.g. ADSA*, axisymmetric drop shape analysis, developed by Rotenberg *et al.* [38] and its succeeding versions [38-42]) are limited to axisymmetric drops. As shown in Fig. 1-1b, for adhesion measurement application drops are not symmetrical; therefore, analytical-image processing methods are not useful.

Exclusively image processing methods are potentially able to measure the contact angle of any drop with any shape (axisymmetric or not). Therefore, image processing methods can be versatile when implemented properly. The state-of-the-art exclusively image processing methods are susceptive to human error as user should pick the contact and a few boundary points manually *e.g.* [43-53]. Other exiting drawbacks are explained in details in Chapter 3. In summary, exclusively image processing methods are potentially superior to analytical-image processing methods. However, as explained earlier, the state-of-the-art exclusively image processing methods are susceptible to human error. Also, they are not suitable for automated computer implementation or process of a set of image files in a folder. In Chapter 3 an exclusively image processing method is developed to measure the contact angle of asymmetrical drops with addressing the shortcomings explained here.

1.4 Evaporation of Drops in Room Conditions

In some applications removing the whole drop all at once is either not possible or not desirable, *e.g.* ink jet printing [54]. Instead, liquid should be removed from the surface gradually and/or with minimum applied force. Evaporation in room temperature requires no applied force and driven energy will be provided from the surrounding air and/or substrate. As such, for such applications evaporation in room temperature can be promising.

Evaporation in room temperature has a broad application in cleaning industries, PEM (Proton Exchange Membrane) fuel cells [2, 3, 55], protective coatings [56, 57], heat exchangers [58], printing processes [59, 60], surface patterning [61], dispensing small particles, fabricating nano-features. The goal of studying the evaporation is finding the evaporation rate and evaporation time. For most of the above mentioned applications, drops are on solid surfaces. Existence of a solid surface adds extra variables to the factors affecting the evaporation, *e.g*. thermal conductivity of the substrate [62, 63] or variation of the evaporation flux across the drop surface [64]. To comprehensively study the evaporation of drops, as the first step, and to limit the complication due to presence of a surface, it will be wise to first study a spherical and suspended drop (later effect of presence of a solid surface will be combined). The goal of studying the evaporation of suspended and spherical drops, in a quiescent environment, in this thesis is answering the following two questions: Is evaporation a purly diffusive mechanism (as assumed in literature) or a diffusive-convective? Is the evaporation a steady-state mechanism (as assumed in literature) or a transient? It should be noted that according to literature studies, *e.g.* [25, 65-78], drop evaporation is assumed to be a pure-diffusive and steady-state mechanism and these two assumptions are known as Maxwell assumptions.

1.4.1 Evaporation of Suspended Drops

Studying the evaporation of fully isolated and suspended drops in a quiescent environment is important in understanding the drop evaporation fundamentally. During the evaporation of drops, the following two steps take place [74]: (i) phase change of the liquid from liquid to vapor at the surface of the drop which can be found using Clausius-Clapeyron equation; and (ii) transport of the vapor in air.

Literature shows that evaporation of suspended drops in room temperature, atmospheric conditions and in quiescent air is controlled by the second step [79-81], *i.e.* transport of vapor in the surrounding and not the phase change.

1.4.1.1 Maxwell’s Assumption for Evaporation of Suspended Drops

The movement of vapor in the surrounding can be decomposed to convection (bulk motion of vapor) and diffusion. Literature assumes the bulk motion of vapor (convection) is negligible and evaporation is governed only by diffusion of vapor into air. Also, the evaporation process is assumed as steady-state. These assumptions were taken by Maxwell for evaporation from a wet-bulb thermometer. Sreznevsky [82] adapted Maxwell’s assumptions to the evaporation of drops. After that, Maxwell assumptions are widely used for finding the evaporation flux of drops, *e.g.* [25, 65-78].

Regarding the steady-state assumption, the original experiment of Maxwell, took 2-3 days and the vapor flux rate became relatively steady after approximately 45min. However, for a micro-liter drop where the lifetime is in the order of minutes, assuming a quasi-steady process may not be a good assumption. This is further investigated in Chapter 4 by considering a heat analogy problem *i.e.* a semi-infinite slab which initially is at a uniform temperature [83].

Regarding the non-convective assumption, Guena *et al.* [84, 85], from observing an identical evaporation behavior for sessile and hanging drops of the same type concluded convection is small during the evaporation of micro-liter drops. However, the “buoyancy” is a better term for the observation mentioned in [84, 85], and not the “convection”. Buoyancy is ascending or descending the vapor due to the weight of vapor relative to air, and has opposite effects on sessile and pendant drops [86]. Buoyancy changes the evaporation rate through changing the convection (see Chapter 5). So, such experiments cannot approve or disprove the effect of convection on evaporation of micro-liter drops. It should also be noted that the effect of buoyancy is neglected in Maxwellian studies. To understand and distinguish between buoyancy and convection reader is referred to the problem of evaporation in Stefan tube with gravity [87] where the buoyancy-driven convective flux is compared with the convective flux. Using the Péclet number concept, it can be shown that the evaporation of micro-liter drops is not pure diffusive (this is shown in Chapter 4).

In summary, the validity of Maxwell assumption for micro-liter drops is not fully appreciated. As such, the two assumptions taken by Maxwell should be relaxed. In Chapter 4, by including the convective and transient terms, a transient and convective (TC) model is developed to explain the evaporation of suspended micro-drops (drops not touching a surface) in room temperature, normal atmospheric condition and quiescent environment (*i.e.* no external airflow).

It should be noted that this model is not accurate for drops levitated with electromagnetic energy *e.g.* [88], or falling drops at terminal velocity [89]. As the electromagnetic energy slows the evaporation rate [90] and falling a drop increases the evaporation rate [91]. The proper experiment is a drop which is suspended from a knot or crossover of two wires *e.g.*[92] as the external effects are minimal.

1.4.1.2 Assumptions for Evaporation of Suspended Drops

Kelvin effect is assumed to be negligible (according to Kelvin's the vapor pressure should be higher on the drop surface than on a planar liquid surface). This is a reasonable assumption as for micro-liter drops, as drop radius in this thesis is larger than $0.01\mu m$, Kelvin's effect is not important [93, 94]; for drops smaller than $0.01\mu m$ see Ivchenko [95-98]. Surface cooling will not be studied in this thesis (surface cooling is the drop surface temperature decreases during the evaporation). In [92], it was shown that for some liquids (*e.g.* water drops) surface cooling is as low as $3-4^oC$; and for some liquids (*e.g.* heptane) surface cooling is as high as 20^oC.

The buoyancy effect, which is completely neglected in Maxwell based models, is also neglected in Chapter 4 where a model for studying the evaporation of suspended drops is developed. For fully spherical drops the buoyancy effect should not be significant. The reason is that for example, if the liquid vapor is lighter than air, buoyancy increases the evaporation rate of the top half of the drop while its effect on the bottom half is the opposite. For sessile and pendant drops the effect of buoyancy may be considerable. The buoyancy effect for sessile and pendant drops is studied in Chapter 5.

1.4.1.3 Effect of Buoyancy on Evaporation of Sessile and Pendant Drops

Potentially, buoyancy may increase or decrease the evaporation rate through changing the convection that occurs [79, 84, 86, 99, 100]. Buoyancy can be caused by temperature [100], or density [86] variations. The latter is of interest in evaporation of drops in room condition [86]. There are opposing theories on the effect of density-driven buoyancy on drop evaporation [79, 80, 85, 101]. To observe the importance of buoyancy on drop evaporation, literature studies have compared the evaporation rate of sessile and pendant drops at similar experimental situation (similar liquid type and volume). For example, consider water as the liquid. Water vapor is lighter than air. Therefore, during the evaporation of sessile water drops buoyancy may potentially increase the evaporation rate; whereas for pendant water drops, buoyancy moves the vapor back to the drop and may potentially decrease the evaporation rate. As such, if buoyancy is a considerable factor affecting the evaporation, sessile water drops should evaporate faster than pendant water drops. In general, depending on the relative to air weight of vapor, sessile and pendant water drops should evaporate at different rates. Now, the question to be answered is how large is the effect of buoyancy on evaporation?

Literature studies do not have unanimity on the effect of buoyancy on drop evaporation. Through the comparison, some literature has observed a notable difference between evaporation rate of sessile and pendant drops and suggested that buoyancy’s effect is important. For example, in [99, 100] using the Schlieren imaging technique, it was suggested that in evaporation of liquid hydrocarbons the effect of buoyancy is important. However, some studies observed a negligible or no difference between the evaporation rate of sessile and pendant drops *e.g.* [84, 85, 101, 102]. In other words, there is no systematic study in literature which can answer the following questions: Is there a notable difference between evaporation of pendant and sessile drops (similar volume and substrate)? Is buoyancy a dominant factor in evaporation of micro-liter drops at room condition? In Chapter 5 this matter will be investigated through a systematic experiment.

The next factor which affects the evaporation rate of drops and will be explained is existence of the solid substrate. Including the effects of the solid substrate enables one to develop a model to predict the evaporation rate of sessile drops.

1.4.2 Evaporation of Sessile Drops

The presence of a solid substrate affects the evaporation rate [62]. As such, compared to the suspended/levitated drop case, studying the evaporation of sessile drops requires more considerations. One of the considerations is the variation of evaporation flux on the drop surface. For a sessile drop, the evaporation flux changes from a maximum value at the contact line to a minimum at the drop apex [59, 64, 103-109], see Fig. 1-3.

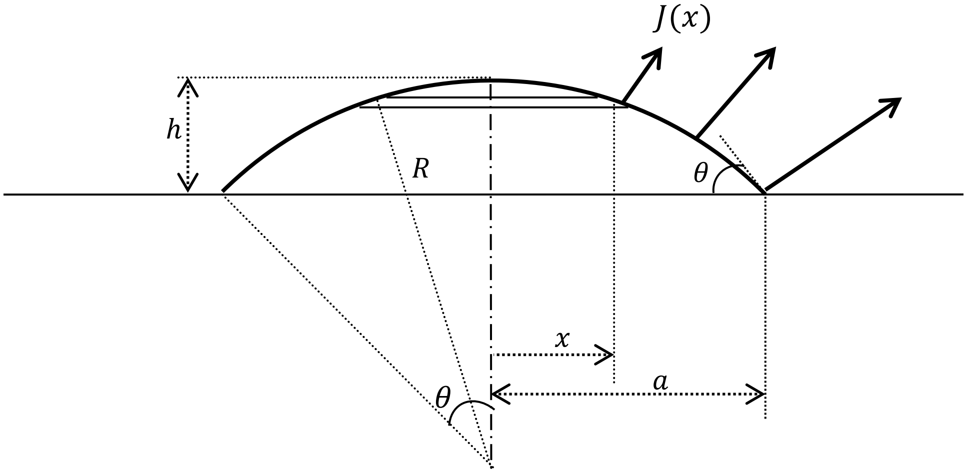

Fig. 1-3 Variation of evaporation flux along the drop surface is shown. $J(x)$ is the evaporation flux at x. Evaporation flux is at its maximum at the contact line. It is assumed that drop has a spherical cap shape with radius R.

There are two categories of studies in literature to find the evaporation flux distribution across the drop surface: (i) flow visualization techniques and (ii) solutions based on electrostatic analogies.

As will be explained, flow visualization techniques, as done, are not proper to find the evaporation flux distribution across the drop surface. In flow visualization techniques, the flow inside an evaporating drop is attributed to the Marangoni flow [50]. From that, it was concluded that the evaporation flux increases from apex to the contact line [76]. The explanation is as follows. Surface tension is temperature dependent and decreases by increasing the temperature. Therefore, the higher evaporation rate near the contact line may cause a lower temperature at the contact line and Marangoni flow, accordingly. Flow visualization techniques cannot provide the magnitude of the evaporation flux distribution on the drop surface. Also, due to the following two reasons flow visualization techniques cannot even provide a complete explanation for the higher evaporation rate near the contact line. First, the flow inside the drop may have a different source *e.g.* capillary flow due to seed particles used for visualization [59]. Second, the temperature decrease may be attributed to the thermal conductivity of the substrate [62].

Using electrostatic analogies and relating the vapor concentration and evaporation flux to electrostatic potential and electrostatic field, studies in literature have tried to find the evaporation flux distribution on the drop surface, *e.g.* [64]. The two electrostatic analogy problems mentioned in literature are: (i) the problem of finding the electrostatic fields and charge densities in two-dimensional corners and along the edges [107], and (ii) Dirichlet problem for a domain bounded by two intersecting spheres, or capacitance of an equiconvex lens [108].

The first electrostatic analogy was mentioned in [109]. As the first electrostatic analogy problem was for flat conducting surfaces, it is only usable for small contact angles where the drop surface is nearly flat.

The second electrostatic analogy was mentioned in [64, 84, 85, 104]. This analogy problem is valid for spherical cap shape geometries. The spherical shape for the drop is not a major limitation especially for small drops, as for small (micro-liter) drops, *i.e.* Bo <<1, drops have spherical cap shapes ($Bo = \frac{\rho_L g L^2}{\gamma}$, where Bo is Bond number, ρ_L is the liquid density, g is the acceleration gravity, and L is a characteristic length which is equal to $\frac{3V}{A}$ for drops, V and A are drop volume and radius accordingly). This analogy (the Dirichlet problem) is an appropriate analogy for the evaporation of micro-liter sessile drops. The analogy details are vaguely mentioned in literature (derivation details are scarce), and remained unsolved. This matter is addressed in Chapter 6.

After finding the evaporation rate, evaporation time should be calculated. In the case of fully spherical (suspended) drops, the only changing geometrical parameter was the drop radius. As such, finding a radius versus time relation can lead to finding the evaporation time (solving for time when drop radius is zero). For micro-liter sessile drops, drop has a spherical cap shape. Any two of the drop height, wetted diameter and contact angle are needed to explain the drop volume change. During the evaporation of pure drops from horizontal surfaces, only one of the following two drop shape changes is observed at a time [72]: (i) decrease of the wetted diameter with constant θ; and (ii) constant wetted diameter with decreasing θ (each of these drop evolution cases is called an evaporation mode [65, 69, 70, 75]). Therefore, during the evaporation of sessile drops only one independent geometrical parameter may change. By finding a relation for the changing parameter (*e.g.* wetted diameter) versus time and solving for time when the changing parameter is zero one may find the evaporation time.

As mentioned above, for finding the evaporation time of sessile drops, knowing the evaporation mode is needed. According to literature, the value of contact angle [25, 67, 103, 104], the value of contact angle hysteresis (the difference between advancing, θ_A, and receding, θ_R contact angles) [72, 110], the value of θ_R [66], surrounding air pressure [71, 94] and viscosity are named as the physical elements affecting the evaporation mode.

To develop a model to explain the evaporation time of sessile drops, evaporation mode at which the drop evaporates should be identified [111]. In this Thesis, two sessile drop evaporation relations for the two possible modes are developed (one for evaporation in constant wetted diameter and one for evaporation in constant contact angle). Knowing the evaporation mode and using the developed relation one may find the evaporation time of sessile drops. Knowing the physical elements affecting the evaporation mode and their level of influence is important to predict the evaporation mode. In future work, the physical elements affecting the evaporation mode may be studied.

1.5 Objectives

- Developing a model to measure the adhesion force between a drop and its substrate
- Developing a method to measure the contact angle of asymmetric drops
- Developing a model for evaporation of suspended spherical drops at room condition
- Evaluating the effect of buoyancy on evaporation of micro-liter drops at room condition
- Developing a model for calculating the variation of evaporation flux along the drop surface of sessile drops

1.6 References

[1] Tan, S. C., 2005, "Effects of large droplet dynamics on airfoil impingement characteristics," 43rd AIAA Aerospace Sciences Meeting and Exhibit - Meeting Papers, Anonymous pp. 8389-8401.

[2] Lan, H., Friedrich, M., Armaly, B. F., 2008, "Simulation and Measurement of 3D Shear-Driven Thin Liquid Film Flow in a Duct," International Journal of Heat and Fluid Flow, **29**(2) pp. 449-459.

[3] Kumbur, E. C., Sharp, K. V., and Mench, M. M., 2006, "Liquid Droplet Behavior and Instability in a Polymer Electrolyte Fuel Cell Flow Channel," Journal of Power Sources, **161**(1) pp. 333-345.

[4] White, E. B., and Schmucker, J. A., 2008, "A Runback Criterion for Water Drops in a Turbulent Accelerated Boundary Layer," Journal of Fluids Engineering, Transactions of the ASME, **130**(6) .

[5] Kolev, V. L., Kochijashky, I. I., Danov, K. D., 2003, "Spontaneous Detachment of Oil Drops from Solid Substrates: Governing Factors," Journal of Colloid and Interface Science, **257**(2) pp. 357-363.

[6] Kralchevsky, P. A., Danov, K. D., Kolev, V. L., 2005, "Detachment of Oil Drops from Solid Surfaces in Surfactant Solutions: Molecular Mechanisms at a Moving Contact Line," Industrial and Engineering Chemistry Research, **44**(5) pp. 1309-1321.

[7] Wenzel, R. N., 1949, "Surface Roughness and Contact Angle," Journal of Physical & Colloid Chemistry, **53**(9) pp. 1466-1467.

[8] Cassie, A. B. D., 1948, "Contact Angles," Discussions of the Faraday Society, **3**pp. 11-16.

[9] Gao, L., and McCarthy, T. J., 2009, "An Attempt to Correct the Faulty Intuition Perpetuated by the Wenzel and Cassie "Laws"," Langmuir, **25**(13) pp. 7249-7255.

[10] Gao, L., and McCarthy, T. J., 2007, "How Wenzel and Cassie were Wrong," Langmuir, **23**(7) pp. 3762-3765.

[11] Pease, D. C., 1945, "The Significance of the Contact Angle in Relation to the Solid Surface," Journal of Physical Chemistry, **49**(2) pp. 107-110.

[12] Bartell, F. E., and Shepard, J. W., 1953, "Surface Roughness as Related to Hysteresis of Contact Angles. II. the Systems Paraffin-3 Molar Calcium Chloride Solution-Air and Paraffin-Glycerol-Air," Journal of Physical Chemistry, **57**(4) pp. 455-458.

[13] Bartell, F. E., and Shepard, J. W., 1953, "Surface Roughness as Related to Hysteresis of Contact Angles. I. the System Paraffin-Water-Air," Journal of Physical Chemistry, **57**(2) pp. 211-215.

[14] Extrand, C. W., 2003, "Contact Angles and Hysteresis on Surfaces with Chemically Heterogeneous Islands," Langmuir, **19**(9) pp. 3793-3796.

[15] Gao, L., and McCarthy, T. J., 2009, "Wetting 101°," Langmuir, **25**(24) pp. 14105-14115.

[16] Cheng, D. F., and McCarthy, T. J., 2011, "Using the Fact that Wetting is Contact Line Dependent," Langmuir, **27**(7) pp. 3693-3697.

[17] Princen, H. M., 1999, "Spinning Drop Method Applied to Three-Phase Fluid Equilibria," Langmuir, **15**(21) pp. 7386-7391.

[18] Antonini, C., Carmona, F. J., Pierce, E., 2009, "General Methodology for Evaluating the Adhesion Force of Drops and Bubbles on Solid Surfaces," Langmuir, **25**(11) pp. 6143-6154.

[19] Chen, S. C., and Lin, J. F., 2008, "Detailed Modeling of the Adhesion Force between an AFM Tip and a Smooth Flat Surface Under Different Humidity Levels," Journal of Micromechanics and Microengineering, **18**(11) .

[20] Rabinovich, Y. I., Adler, J. J., Ata, A., 2000, "Adhesion between Nanoscale Rough Surfaces. I. Role of Asperity Geometry," Journal of Colloid and Interface Science, **232**(1) pp. 10-16.

[21] Rabinovich, Y. I., Adler, J. J., Ata, A., 2000, "Adhesion between Nanoscale Rough Surfaces: II. Measurement and Comparison with Theory," Journal of Colloid and Interface Science, **232**(1) pp. 17-24.

[22] Freitas, A. M., and Sharma, M. M., 2001, "Detachment of Particles from Surfaces: An AFM Study," Journal of Colloid and Interface Science, **233**(1) pp. 73-82.

[23] Yadav, P. S., Bahadur, P., Tadmor, R., 2008, "Drop Retention Force as a Function of Drop Size," Langmuir, **24**(7) pp. 3181-3184.

[24] Alvarez, J. M., Amirfazli, A., and Neumann, A. W., 1999, "Automation of the Axisymmetric Drop Shape Analysis-Diameter for Contact Angle Measurements," Colloids and Surfaces A: Physicochemical and Engineering Aspects, **156**(1-3) pp. 163-176.

[25] McHale, G., Rowan, S. M., Newton, M. I., 1998, "Evaporation and the Wetting of a Low-Energy Solid Surface," Journal of Physical Chemistry B, **102**(11) pp. 1964-1967.

[26] Kugel, G., Klettke, T., Goldberg, J. A., 2007, "Investigation of a New Approach to Measuring Contact Angles for Hydrophilic Impression Materials," Journal of Prosthodontics, **16**(2) pp. 84-92.

[27] Dogan Buzoglu, H., Calt, S., and Gümüsderelioglu, M., 2007, "Evaluation of the Surface Free Energy on Root Canal Dentine Walls Treated with Chelating Agents and NaOCl," International Endodontic Journal, **40**(1) pp. 18-24.

[28] Kontakiotis, E. G., Tzanetakis, G. N., and Loizides, A. L., 2007, "A Comparative Study of Contact Angles of Four Different Root Canal Sealers," Journal of Endodontics, **33**(3) pp. 299-302.

[29] Daffonchio, D., Thaveesri, J., and Verstraete, W., 1995, "Contact Angle Measurement and Cell Hydrophobicity of Granular Sludge from Upflow Anaerobic Sludge Bed Reactors," Applied and Environmental Microbiology, **61**(10) pp. 3676-3680.

[30] Salaün, F., Devaux, E., Bourbigot, S., 2009, "Application of Contact Angle Measurement to the Manufacture of Textiles Containing Microcapsules," Textile Research Journal, **79**(13) pp. 1202-1212.

[31] Neumann, A.W., 1996, "Applied Surface Thermodynamics," CRC Press, New York, USA, .

[32] Oguz, H. N., and Sadhal, S. S., 1988, "Effects of Soluble and Insoluble Surfactants on the Motion of Drops." Journal of Fluid Mechanics, **194**pp. 563-579.

[33] Amirfazli, A., Keshavarz, A., Zhang, L., 2003, "Determination of Line Tension for Systems Near Wetting," Journal of Colloid and Interface Science, **265**(1) pp. 152-160.

[34] Rusanov, A. I., 1999, "Classification of Line Tension," Colloids and Surfaces A: Physicochemical and Engineering Aspects, **156**(1-3) pp. 315-322.

[35] Bateni, A., Laughton, S., Tavana, H., 2005, "Effect of Electric Fields on Contact Angle and Surface Tension of Drops," Journal of Colloid and Interface Science, **283**(1) pp. 215-222.

[36] Marmur, A., 1997, "Line Tension and the Intrinsic Contact Angle in Solid-Liquid-Fluid Systems," Journal of Colloid and Interface Science, **186**(2) pp. 462-466.

[37] Baxter, S., 1950, "Wetting and Contact-Angle Hysteresis," Nature, **165**(4188) pp. 198.

[38] Rotenberg, Y., Boruvka, L., and Neumann, A. W., 1983, "Determination of Surface Tension and Contact Angle from the Shapes of Axisymmetric Fluid Interfaces," Journal of Colloid and Interface Science, **93**(1) pp. 169-183.

[39] Del Río, O. I., and Neumann, A. W., 1997, "Axisymmetric Drop Shape Analysis: Computational Methods for the Measurement of Interfacial Properties from the Shape and Dimensions of Pendant and Sessile Drops," Journal of Colloid and Interface Science, **196**(2) pp. 136-147.

[40] Kalantarian, A., David, R., and Neumann, A. W., 2009, "Methodology for High Accuracy Contact Angle Measurement," Langmuir, **25**(24) pp. 14146-14154.

[41] Bateni, A., Susnar, S. S., Amirfazli, A., 2004, "Development of a New Methodology to Study Drop Shape and Surface Tension in Electric Fields," Langmuir, **20**(18) pp. 7589-7597.

[42] Hoorfar, M., and W. Neumann, A., 2006, "Recent Progress in Axisymmetric Drop Shape Analysis (ADSA)," Advances in Colloid and Interface Science, **121**(1-3) pp. 25-49.

[43] Li, L., Kang, W., and Ye, D., 2007, "A contact angle measurement method for the droplets in EWOD-based chips," Proceedings of the 2nd IEEE International Conference on Nano/Micro Engineered and Molecular Systems, IEEE NEMS 2007, Anonymous pp. 1071-1075.

[44] Goclawski, J., and Urbaniak-Domagala, W., 2007, "The method of solid-liquid contact angle measurement using the images of sessile drops with shadows on substratum," Proceeding of the 3rd International Conference of Young Scientists "Perspective Technologies and Methods in MEMS Design", MEMSTECH 2007, Anonymous pp. 135-140.

[45] Bortolotti, M., Brugnara, M., Volpe, C. D., 2009, "Numerical Models for the Evaluation of the Contact Angle from Axisymmetric Drop Profiles: A Statistical Comparison," Journal of Colloid and Interface Science, **336**(1) pp. 285-297.

[46] Iliev, S., and Pesheva, N., 2006, "Nonaxisymmetric Drop Shape Analysis and its Application for Determination of the Local Contact Angles," Journal of Colloid and Interface Science, **301**(2) pp. 677-684.

[47] Bateni, A., Susnar, S. S., Amirfazli, A., 2003, "A High-Accuracy Polynomial Fitting Approach to Determine Contact Angles," Colloids and Surfaces A: Physicochemical and Engineering Aspects, **219**(1-3) pp. 215-231.

[48] Schuetter, S., Shedd, T., Doxtator, K., 2006, "Measurements of the Dynamic Contact Angle for Conditions Relevant to Immersion Lithography," Journal of Microlithography, Microfabrication and Microsystems, **5**(2) .

[49] Stalder, A. F., Kulik, G., Sage, D., 2006, "A Snake-Based Approach to Accurate Determination of both Contact Points and Contact Angles," Colloids and Surfaces A: Physicochemical and Engineering Aspects, **286**(1-3) pp. 92-103.

[50] Xu, C., and Prince, J. L., 1998, "Snakes, Shapes, and Gradient Vector Flow," IEEE Transactions on Image Processing, **7**(3) pp. 359-369.

[51] Anonymous "Contact Angle Measurements using the Drop Shape Method," .

[52] Woodward R. P., "Dispensing Method and Apparatus for Dispensing very SmallQuantities of Fluid." (US 6579497) .

[53] Anonymous "Image Tool Version 3.0," .

[54] Thomas, J. E., and McKnight, J. K., 1984, "Ink Evaporation Prevention Means for Ink Jet Print Head," (4412233) .

[55] Ous, T., and Arcoumanis, C., 2007, "Visualisation of Water Droplets during the Operation of PEM Fuel Cells," Journal of Power Sources, **173**(1) pp. 137-148.

[56] Nguyen, T. A. H., Nguyen, A. V., Hampton, M. A., 2012, "Theoretical and Experimental Analysis of Droplet Evaporation on Solid Surfaces," Chemical Engineering Science, **69**(1) pp. 522-529.

[57] Panwar, A. K., Barthwal, S. K., and Ray, S., 2003, "Effect of Evaporation on the Contact Angle of a Sessile Drop on Solid Substrates," Journal of Adhesion Science and Technology, **17**(10) pp. 1321-1329.

[58] Semenov, S., Starov, V. M., Rubio, R. G., 2011, "Evaporation of Sessile Water Droplets: Universal Behaviour in Presence of Contact Angle Hysteresis," Colloids and Surfaces A: Physicochemical and Engineering Aspects, **391**(1-3) pp. 135-144.

[59] Deegan, R. D., Bakajin, O., Dupont, T. F., 1997, "Capillary Flow as the Cause of Ring Stains from Dried Liquid Drops," Nature, **389**(6653) pp. 827-829.

[60] Ihnen, A. C., Petrock, A. M., Chou, T., 2011, "Crystal Morphology Variation in Inkjet-Printed Organic Materials," Applied Surface Science, **258**(2) pp. 827-833.

[61] Fischer, B. J., 2002, "Particle Convection in an Evaporating Colloidal Droplet," Langmuir, **18**(1) pp. 60-67.

[62] Dunn, G. J., Wilson, S. K., Duffy, B. R., 2009, "The Strong Influence of Substrate Conductivity on Droplet Evaporation," Journal of Fluid Mechanics, **623**pp. 329-351.

[63] David, S., Sefiane, K., and Tadrist, L., 2007, "Experimental Investigation of the Effect of Thermal Properties of the Substrate in the Wetting and Evaporation of Sessile Drops," Colloids and Surfaces A: Physicochemical and Engineering Aspects, **298**(1-2) pp. 108-114.

[64] Deegan, R. D., Bakajin, O., Dupont, T. F., 2000, "Contact Line Deposits in an Evaporating Drop," Phys. Rev. E, **62**(1 B) pp. 756-765.

[65] Shi, L., Shen, P., Zhang, D., 2009, "Wetting and Evaporation Behaviors of Water-Ethanol Sessile Drops on PTFE Surfaces," Surface and Interface Analysis, **41**(12-13) pp. 951-955.

[66] Soolaman, D. M., and Yu, H. Z., 2005, "Water Microdroplets on Molecularly Tailored Surfaces: Correlation between Wetting Hysteresis and Evaporation Mode Switching," Journal of Physical Chemistry B, **109**(38) pp. 17967-17973.

[67] Song, H., Lee, Y., Jin, S., 2008, "Sessile drop evaporation on surfaces of various wettability," 2008 Proc. ASME Micro/Nanoscale Heat Transfer Int. Conf., MNHT 2008, Anonymous **PART A,** pp. 445-451.

[68] Liu, C., Bonaccurso, E., and Butt, H., 2008, "Evaporation of Sessile Water/Ethanol Drops in a Controlled Environment," Phys. Chem. Chem. Phys., **10**(47) pp. 7150-7157.

[69] Shanahan, M. E. R., and Bourgès, C., 1994, "Effects of Evaporation on Contact Angles on Polymer Surfaces," International Journal of Adhesion and Adhesives, **14**(3) pp. 201-205.

[70] Shin, D. H., Lee, S. H., Jung, J. -., 2009, "Evaporating Characteristics of Sessile Droplet on Hydrophobic and Hydrophilic Surfaces," Microelectronic Eng., **86**(4-6) pp. 1350-1353.

[71] Cioulachtjian, S., Launay, S., Boddaert, S., 2010, "Experimental Investigation of Water Drop Evaporation Under Moist Air Or Saturated Vapour Conditions," Int. J. Thermal Sci., **49**(6) pp. 859-866.

[72] Picknett, R. G., and Bexon, R., 1977, "The Evaporation of Sessile Or Pendant Drops in Still Air," Journal of Colloid and Interface Science, **61**(2) pp. 336-350.

[73] Birdi, K. S., Vu, D. T., and Winter, A., 1989, "A Study of the Evaporation Rates of Small Water Drops Placed on a Solid Surface," Journal of Physical Chemistry, **93**(9) pp. 3702-3703.

[74] Fang, X., Li, B., Petersen, E., 2005, "Factors Controlling the Drop Evaporation Constant," Journal of Physical Chemistry B, **109**(43) pp. 20554-20557.

[75] Bourgès-Monnier, C., and Shanahan, M. E. R., 1995, "Influence of Evaporation on Contact Angle," Langmuir, **11**(7) pp. 2820-2829.

[76] Erbil, H. Y., McHale, G., and Newton, M. I., 2002, "Drop Evaporation on Solid Surfaces: Constant Contact Angle Mode," Langmuir, **18**(7) pp. 2636-2641.

[77] Rowan, S. M., Newton, M. I., and McHale, G., 1995, "Evaporation of Microdroplets and the Wetting of Solid Surfaces," Journal of Physical Chemistry, **99**(35) pp. 13268-13271.

[78] Furuta, T., Sakai, M., Isobe, T., 2009, "Evaporation Behavior of Microliter- and Sub-Nanoliter-Scale Water Droplets on Two Different Fluoroalkylsilane Coatings," Langmuir, **25**(20) pp. 11998-12001.

[79] Poulard, C., Guéna, G., and Cazabat, A., 2005, "Diffusion-Driven Evaporation of Sessile Drops," Journal of Physics Condensed Matter, **17**(49) pp. S4213-S4227.

[80] Poulard, C., Guéna, G., Cazabat, A., 2005, "Rescaling the Dynamics of Evaporating Drops," Langmuir, **21**(18) pp. 8226-8233.

[81] Maxwell, J.C., 1890, "Collected Scientific Papers,"Cambridge, pp. 628.

[82] Sreznevsky, V., 1882, Zhurnal Fizicheskoi Khimii, **14**(420) pp. 483.

[83] Jiji, L.M., 2003, "Heat Conduction," Begel House Inc., New York, .

[84] Guena, G., Poulard, C., and Cazabat, A., 2007, "The Dynamics of Evaporating Sessile Droplets," Colloid Journal, **69**(1) pp. 1-8.

[85] Guéna, G., Poulard, C., and Cazabat, A., 2007, "The Leading Edge of Evaporating Droplets," Journal of Colloid and Interface Science, **312**(1) pp. 164-171.

[86] Shahidzadeh-Bonn, N., Rafaï, S., Azouni, A., 2006, "Evaporating Droplets," Journal of Fluid Mechanics, **549**pp. 307-313.

[87] Markham, B. L., and Rosenberger, F., 1980, "Velocity and Concentration Distribution in a Stefan Diffusion Tube." Chemical Engineering Communications, **5**(5-6) pp. 287-298.

[88] Mitchem, L., Buajarern, J., Hopkins, R. J., 2006, "Spectroscopy of Growing and Evaporating Water Droplets: Exploring the Variation in Equilibrium Droplet Size with Relative Humidity," J. Phys. Chem. A, **110**(26) pp. 8116-8125.

[89] Pruppacher, H. R., and Rasmussen, R., 1979, "A Wind Tunnel Investigation of the Rate of Evaporation of Large Water Drops Falling at Terminal Velocity in Air." Journal of the Atmospheric Sciences, **36**(7) pp. 1255-1260.

[90] Bhalwankar, R. V., Sathe, A. B., and Kamra, A. K., 2004, "The Evaporation of the Charged and Uncharged Water Drops Suspended in a Wind Tunnel," Proceedings of the Indian Academy of Sciences, Earth and Planetary Sciences, **113**(2) pp. 129-138.

[91] Watts, R. G., 1971, "Relaxation Time and Steady Evaporation Rate of Freely Falling Raindrops," J. Atmos. Sci., **28**pp. 219-225.

[92] Erbil, H. Y., and Dogan, M., 2000, "Determination of Diffusion Coefficient-Vapor Pressure Product of some Liquids from Hanging Drop Evaporation," Langmuir, **16**(24) pp. 9267-9273.

[93] Butt, H., Golovko, D. S., and Bonaccurso, E., 2007, "On the Derivation of Young's Equation for Sessile Drops: Nonequilibrium Effects due to Evaporation," Journal of Physical Chemistry B, **111**(19) pp. 5277-5283.

[94] Thomson, W., 1871, "On the Equilibrium of Vapour at a Curved Surface of Liquid," Philos. Mag., **42**(2) pp. 448-452.

[95] Ivchenko, I. N., 1979, "Evaporation of Spherical Drops Under Conditions of Thermostatic Control of their Surface," Fluid Dynamics, **14**(5) pp. 790-792.

[96] Ivchenko, I. N., and Muradyan, S. M., 1982, "Evaporation of Spherical Drops in a Binary Gas Mixture at Arbitrary Knudsen Numbers," Fluid Dynamics, **17**(1) pp. 92-97.

[97] Ivchenko, I. N., 1984, "The Evaporation and Growth of Spherical Droplets at Intermediate Knudsen Numbers," Fluid Dynamics, **19**(2) pp. 335-337.

[98] Ivchenko, I. N., 1985, "Heat and Mass Transfer during Evaporation Or Condensation Growth of Spherical Drops." High Temperature, **23**(4) pp. 634-638.

[99] Kelly-Zion, P. L., Pursell, C. J., Booth, R. S., 2009, "Evaporation Rates of Pure Hydrocarbon Liquids Under the Influences of Natural Convection and

Diffusion," International Journal of Heat and Mass Transfer, **52**(13-14) pp. 3305-3313.

[100] Kelly-Zion, P. L., Pursell, C. J., Vaidya, S., 2011, "Evaporation of Sessile Drops Under Combined Diffusion and Natural Convection," Colloids and Surfaces A: Physicochemical and Engineering Aspects, **381**(1–3) pp. 31-36.

[101] Guéna, G., Poulard, C., and Cazabat, A., 2007, "Evaporating Drops of Alkane Mixtures," Colloids and Surfaces A: Physicochemical and Engineering Aspects, **298**(1-2) pp. 2-11.

[102] Guéna, G., Poulard, C., and Cazabat, A., 2006, "The Contact Angle of Droplets Evaporating at Ambient Temperature," Applied Mathematics Research eXpress, .

[103] Dhavaleswarapu, H. K., Migliaccio, C. P., Garimella, S. V., 2010, "Experimental Investigation of Evaporation from Low-Contact-Angle Sessile Droplets," Langmuir, **26**(2) pp. 880-888.

[104] Widjaja, E., and Harris, M. T., 2008, "Numerical Study of Vapor Phase-Diffusion Driven Sessile Drop Evaporation," Comput. Chem. Eng., **32**(10) pp. 2169-2178.

[105] Barash, L. Y., Bigioni, T. P., Vinokur, V. M., 2009, "Evaporation and Fluid Dynamics of a Sessile Drop of Capillary Size," Phys. Rev. E, **79**(4) .

[106] Deegan, R. D., 2000, "Pattern Formation in Drying Drops," Phy. Rev. E, **61**(1) pp. 475-485.

[107] Jackson, J.D., 1998, "Classical Electrodynamics,"John Wiley& Sons Inc., pp. 75.

[108] Lebedev, N.N., 1965, "Special Functions and their Applications,"Prentice-Hall Inc., pp. 227.

[109] Berteloot, G., Pham, C. -., Daerr, A., 2008, "Evaporation-Induced Flow Near a Contact Line: Consequences on Coating and Contact Angle," EPL, **83**(1) .

[110] Kulinich, S. A., and Farzaneh, M., 2009, "Effect of Contact Angle Hysteresis on Water Droplet Evaporation from Super-Hydrophobic Surfaces," Applied Surface Science, **255**(7) pp. 4056-4060.

[111] Anantharaju, N., Panchagnula, M., and Neti, S., 2009, "Evaporating Drops on Patterned Surfaces: Transition from Pinned to Moving Triple Line," Journal of Colloid and Interface Science, **337**(1) pp. 176-182.

Chapter 2 - Drop Adhesion Force Applicable to any Arbitrary Shape Drop with Convex Contact Line

2.1 Introduction

Drop removal from solid surfaces is a challenge in various areas such as aerospace [1], fuel cell technology [2, 3], cleaning application [4], wind turbines [5], oil recovery [6, 7], etc. The purpose of this study is to find a general relationship to measure the adhesion force between drops and solid surfaces. According to Wenzel's and Cassie's theories, it was deemed that adhesion force occurs on the contact area (solid-liquid interface). Recently, it has been found that the adhesion force occurs on the contact perimeter and not the contact area [8-15]. In other words, adhesion force from a mechanical perspective manifests at the three-phase line, where liquid, air and solid phases meet [13, 16]. The forces on the contact line are surface tension forces (*i.e.* forces operative at the interface in the tangential direction; these tensions are properties of the interface and a function of temperature [15]). The adhesion force which opposes the external load can be found by integrating the surface tension forces along the contact line. This approach is an indirect approach as the adhesion force is not directly measured. The other approach discussed in literature is direct measuring the adhesion force: applying an external load and directly measuring the opposing force using AFM (atomic force microscopy) [17-20]. It was shown that the direct method is more expensive and less accurate [21]. As such, the indirect approach will be used in this study.

2.2 Indirect Measurement of Drop Adhesion Force

Indirect methods add surface tension forces acting on infinitesimal line elements along the three-phase line, to calculate the adhesion force [16]. At any point on the contact line, one can define three operative surface tensions: liquid-vapor (γ), solid-vapor (γ_{SV}) and solid-liquid (γ_{SL}). These surface tensions at any point on the contact line lie in a plane which is perpendicular both to the substrate and to the drop contact line at that point. Young (Eq. 2-1) showed that in equilibrium state, at any point on the contact line, the projections in the direction parallel to the substrate of these three surface tensions are balanced as:

$$\boldsymbol{\gamma_{SL}} + \boldsymbol{\gamma} \cos \theta_Y = \boldsymbol{\gamma_{SV}} \tag{2-1}$$

where θ_Y is the Young's contact angle (see Fig. 1-1a). In equilibrium, according to Eq. 2-1, at any point on the contact line parallel to the substrate surface tension force is zero. As such, the drop adhesion force, which is the summation of these surface tensions over the contact line, has to be zero.

Assuming the solid substrate is relatively flat, the summation of γ_{SL} and γ_{SV} over the contact line becomes zero i.e. $\oint_{Contact\ Line} \boldsymbol{\gamma_{SL}}\, \boldsymbol{dl} = \oint_{Contact\ Line} \boldsymbol{\gamma_{SV}}\, \boldsymbol{dl} = 0$. The reason is that γ_{SL} and γ_{SV} are operative on the contact line, which is a closed curve. The summation of $\gamma \cos \theta$ over the contact line is not always zero. It is only zero when the contact angle along the contact line, or $\theta(\varphi)$, is uniform; where φ is the azimuthal angle (see. Fig. 2-1a). The followings may change the value of contact angle: applying an external force parallel to the substrate [22] on a drop, adsorption of liquid vapor on to the solid surface [23], the line tension for micron size drops or large drops with local micro size radii of curvature [24, 25], impurities [26], electrostatic potential [27, 28], surface roughness [29] and heterogeneity [30].

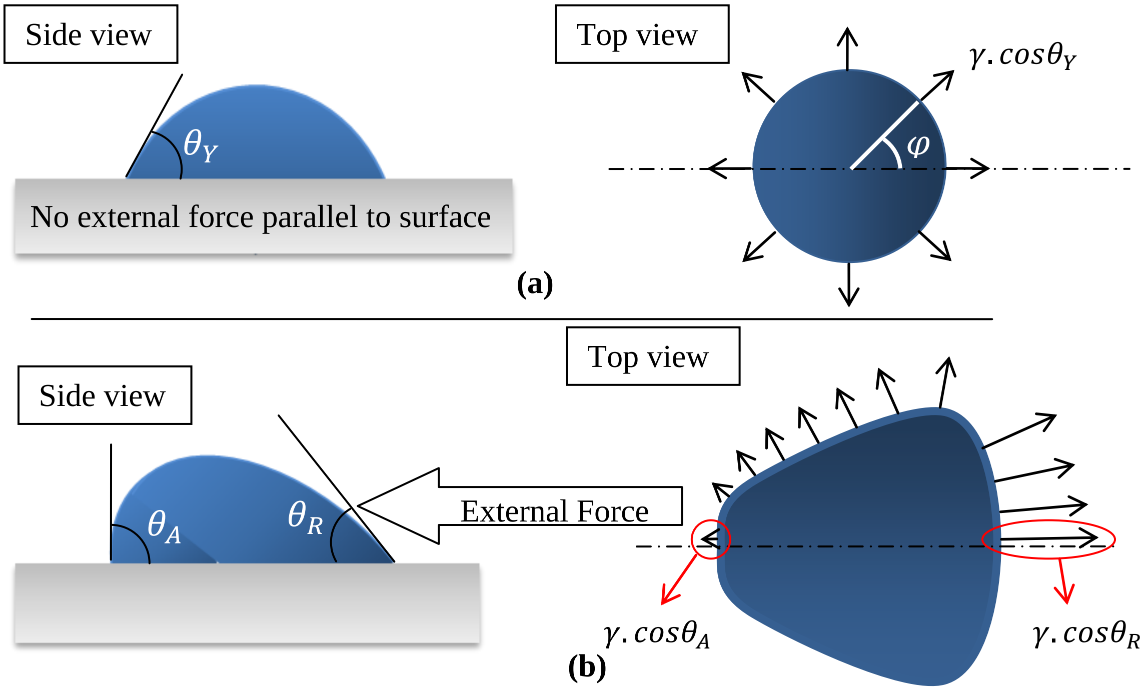

Fig. 2-1 Side and top views of a drop on a smooth surface are shown where (a) no external force parallel to the surface is operative on the drop. Contact angle along the contact line is uniform, and the resultant surface tension force on the drop is zero. (b) A parallel to the substrate external force is operative on the drop and advancing (θ_A) and receding (θ_R) contact angles are shown, the net adhesion force on the drop is against the external force. Note that the surface tensions are operative on the drop and their reactions operate on the drop substrate. $\gamma \cos \theta$ is the projection of surface tension on the plane of substrate.

For a drop on a relatively smooth and homogeneous substrate, the contact angle change is only related to the drop deformation due to an external force parallel to the substrate. Deformation makes the $\theta(\varphi)$ non-uniform along the contact line (*e.g.* see Fig. 2-1b), therefore the summation of $\gamma \cos\theta(\varphi)$ along the contact line becomes non-zero *i.e.* $\oint_{Contact\ Line} \boldsymbol{\gamma} \cos\theta(\varphi)\, \boldsymbol{dl} \neq 0$. The value of $\oint_{Contact\ Line} \boldsymbol{\gamma} \cos\theta(\varphi)\, \boldsymbol{dl}$ is equal to the adhesion force. This value is a function of γ, contact line's length (l), and contact angle along the contact line, $\theta(\varphi)$.

For an arbitrary drop shape, calculating the summation of surface tension forces along the contact line may not be easy. Literature has shown that the summation of surface tension force (or adhesion force) is proportional to the contact angle hysteresis ($\theta_A - \theta_R$), *e.g.* [31]. However, the contact angle hysteresis value does not define the adhesion force accurately. For example, consider two drops with identical contact angle hysteresis values and different shapes or sizes. Contact angle hysteresis values are equal but adhesion forces will be different. Some studies have suggested some approximate relationships which estimate the value of adhesion force. However, the applicability of these relationships is limited to specific contact line shapes (*e.g.* circular), as discussed in the next section.

2.2.1 Circular Contact Lines

One of the earliest approximate relationships for the summation of surface tension forces along the contact line is for drops with circular contact lines [32]:

$$\frac{\boldsymbol{F}}{\boldsymbol{\gamma}R} = k_s(\cos\theta_R - \cos\theta_A) \tag{2-2}$$

where $\boldsymbol{F}$ is the adhesion force, R is the radius of the wetted area and k_s is a constant that should be found experimentally or analytically. As will be shown even for this simple geometry there is no consistent k_s value in literature. Using a finite element model and assuming that $\cos\theta$ linearly varies along the contact line, Brown *et al.* [33], found that k_s should be $\pi/2$. The experimental cases that were used in [33] were consistent with the k_s value found using the finite element model. Using the same assumption for $\cos\theta$, Extrand and Gent [34] found that k_s should be $4/\pi$ and validated the value using experiments. Chen *et al.* [35] assumed that θ linearly changes from its advancing to receding value, using this assumption they suggested that k_s should be equal to π, experiments in [36-38] are consistent with the value found in [35].

2.2.2 Parallel Sided and Elliptical Contact Lines

For drops with parallel sided and elliptical contact lines, the following approximate relationship for the summation of surface tension forces along the contact line is suggested [39]:

$$\frac{\boldsymbol{F}}{\boldsymbol{\gamma}w} = k_e(\cos\theta_R - \cos\theta_A) \tag{2-3}$$

where w is the maximum width of the drop and k_e is a constant. Similar to circular drop, for elliptical and parallel sided drops there is no consistent value for k_e and different values between 1 and π are suggested in literature. For instance, Elsherbini and Jacobi [40] used a third-degree polynomial fit to the $\cos\theta$ values along the contact line and found $k_e = \frac{48}{\pi^3}$. Extrand and Kumagai [39] used a linear fit to the $\cos\theta$ values along the contact line and found $k_e = 0.23 + 1.04\ L/w$ (L is the length of the drop). Assuming that the value of contact angle for half of the drop is equal to θ_A and for the rest half contact angle is equal to θ_R, Dussan and Chow [41, 42] found the value of 2 for k_e. It should be noted that Dussan and Chow [41, 42] approach is only valid for highly stretched out drops with low contact angles (lubrication theory is used in their derivations).

2.2.3 Arbitrary Shape Contact Line: General Methodology

Antonini *et al.* [16] pushed the studies one step further and developed a methodology where instead of finding an approximation relation which fits into the experiments, the surface tension acting on an infinitesimal line element is integrated along the contact line to find the adhesion force. They showed that the literature models (*e.g.* Extrand and Kumagai [39]) underestimate the contact line length of non-circular contact lines. They also developed a methodology to find the contact line from 2D side view images taking into account the perspective error in constructing the contact line. Such methodology however, is restricted to drops with at least one axis of symmetry [16].

In this Chapter, basic geometry principles are used to develop a model to find the summation of surface tension forces along the contact line, applicable to both symmetrical and asymmetrical contact line shapes. This model also accounts for the perspective error in recording the contact line of drops with non-circular contact line shapes. As for non-circular drops, actual and observed drop radii are different [16], the following question should be answered as well, that if the actual and observed (in 2-D side view images) contact angles are similar or different? Furthermore, a routine and necessary practice for detecting the contact point is back to front tilt of the camera, *e.g.* [43]. This should be investigated to see if this routine tilt creates any error in measuring the contact angle or not? The following sections discuss, in particular: calculation of the contact line's length, estimation of the surface tension force, re-construction of contact line from 2-D side view images and contact angle distribution along the contact line.

2.3 Contact Line's Length

For a particular contact line, the contact line's length can be found by integration of an infinitesimal arc of a circle, $r_\varphi d\varphi$, where r_φ is the radius at different azimuthal angles [39] *i.e.* $\int_0^{2\pi} r_\varphi d\varphi$. However, for non-circular contact lines, this arc does not correspond to the actual line element along the contact line, as shown in Fig. 2-2. Instead, dl should be used to find the contact line length, and is given by [16]:

$$dl = \sqrt{(dr_\varphi)^2 + (r_\varphi d\varphi)^2} \tag{2-4}$$

where dr_φ is shown in Fig. 2-2. It should be noted that for circular contact lines, dr_φ is zero; therefore, dl and $r_\varphi d\varphi$ are equal.

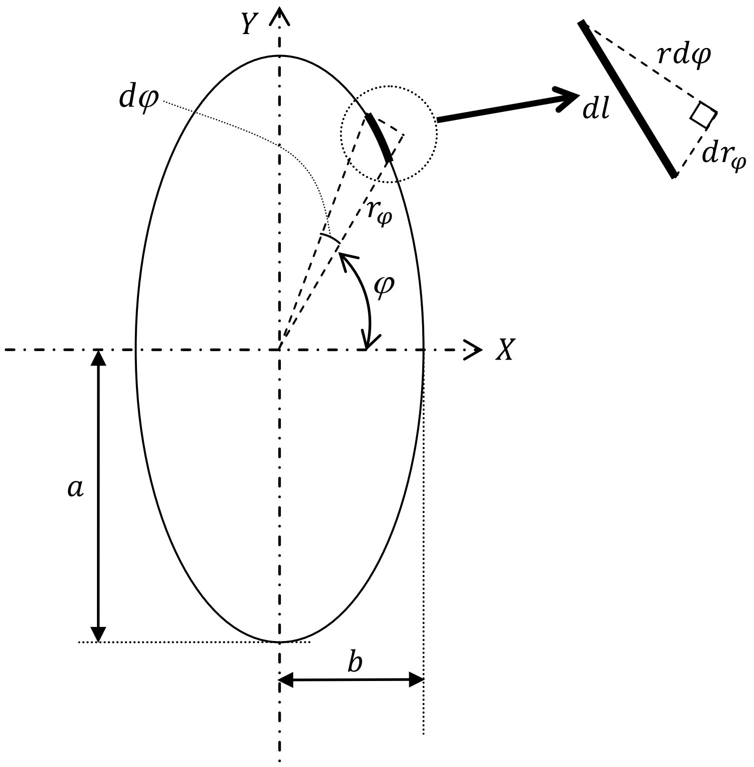

Fig. 2-2 A hypothetical elliptical shape contact line is shown. Integration of $rd\varphi$ over φ (done in [39]) underestimates the contact line's length and dl should be integrated to find the contact line's length [16].

To understand the importance of considering dl rather than $r_{\varphi}d\varphi$ as the length element for calculating the contact line perimeter, consider an elliptical shape contact line. The radius of an ellipse at different azimuthal angles (φ) is given as:

$$r_{\varphi} = \frac{ab}{\sqrt{a^2 \cos^2 \varphi + b^2 \sin^2 \varphi}} \tag{2-5}$$

where a and b are the major and minor radii of the ellipse (see Fig. 2-2). Using Eqs. 2-4 and 2-5 one finds:

$$\int_0^{2\pi} dl = \int_0^{2\pi} r_{\varphi}\, \tau\, d\varphi \tag{2-6}$$

where τ quantifies the difference in length between the line element and the arc of circle, and is given by:

$$\tau = \frac{\sqrt{a^4 \cos^2 \varphi + b^4 \sin^2 \varphi}}{a^2 \cos^2 \varphi + b^2 \sin^2 \varphi} \tag{2-7}$$

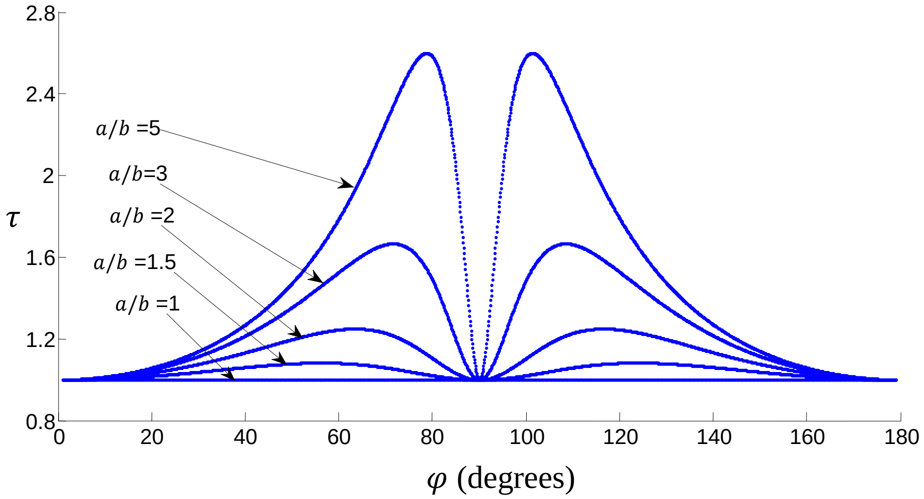

Fig. 2-3 Plot of τ in Eqs. 2-6 and 2-7 with respect to φ (azimuthal angle) at different values of a/b is shown. It is observed that increasing the a/b increases the value of τ.

Figure 2-3 shows the values of τ at different φ for different aspect ratios of the elliptical contact line a/b. For circular contact lines (*i.e.* $a/b = 1$) τ is equal to 1, therefore, the two approaches yield the same result. For elliptical (and in general non-circular) contact lines, the value of τ is always greater than 1 which means that $\int_0^{2\pi} r_\varphi d\varphi$ always underestimates the contact line length.

2.4 Surface Tension Force

The projection of the surface tension vector on the substrate plate, $\gamma \cos \theta(\varphi)$, is perpendicular to the tangent to the contact line, as illustrated in Fig. 2-4. To define to the location of a point on the contact line, in cylindrical coordinate, a origin is needed, *e.g*. point O in Fig. 2-4. In this study, the projection of the apex on the substrate is used as the origin. Drop apex is the only point that is observed in all of the side view images. It should be noted that the direction of $\gamma \cos \theta(\varphi)$ at a point on the contact line is not necessarily the same as the direction of r_φ (*e.g.* see Fig. 2-4). As such, based on the above note and Fig. 2-4, the adhesion force in [39, 40] is modified as [16]:

$$F_x = \gamma \int_0^{2\pi} \cos \psi(\varphi) \cos \theta(\varphi) \sqrt{(\frac{\partial r_\varphi}{\partial \varphi})^2 + r_\varphi^2} \; d\varphi \qquad \text{(2-8,1)}$$

$$F_y = \gamma \int_0^{2\pi} \sin \psi(\varphi) \cos \theta(\varphi) \sqrt{(\frac{\partial r_\varphi}{\partial \varphi})^2 + r_\varphi^2} \; d\varphi \qquad \text{(2-8,2)}$$

where F_x and F_y are adhesion forces in X and Y directions; and $\psi(\varphi)$ is the angle between the $\gamma \cos \theta(\varphi)$ and the X-axis at different azimuthal angles (φ).

Thus, to find the adhesion force on a drop, one needs to express the three variables ψ, θ and r_φ as functions of φ, as well as the length of the contact line.

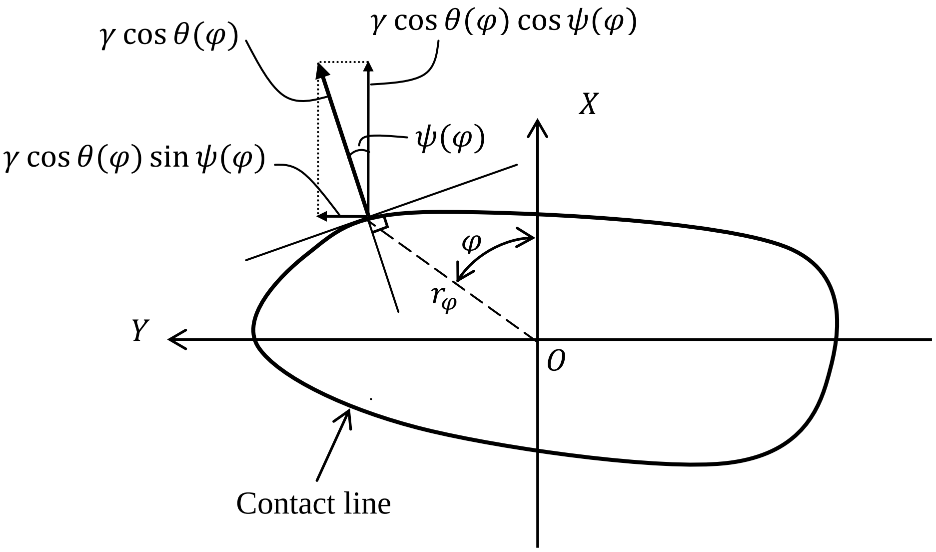

Fig. 2-4 Three-phase line of an arbitrary shape drop is shown. The $\gamma\cos\theta(\varphi)$ is the "projection of γ on the substrate" and is perpendicular to the contact line. $\psi(\varphi)$ is the angle between the X-axis and $\gamma\cos\theta(\varphi)$. O is the projection of the apex on the drop base plane, and r_φ is measured from O in CCW direction.

2.5 Construction of Contact Line from 2-D Side View Images

Regarding the construction of contact line from 2-D side view images, one may think that this is a redundant task as the top view image of the drop can show both the contact line and the drop radius at different azimuthal angles. However, the problem arises for drops with contact angles larger than 90° where the contact line is not observable from the top view image. The only exception is for axisymmetric drops with known volume [44]. As will be shown, using the 2-D side view images (such as the ones in Fig. 2-5) one can find the value of r_φ at different azimuthal angles and reconstruct the contact line.

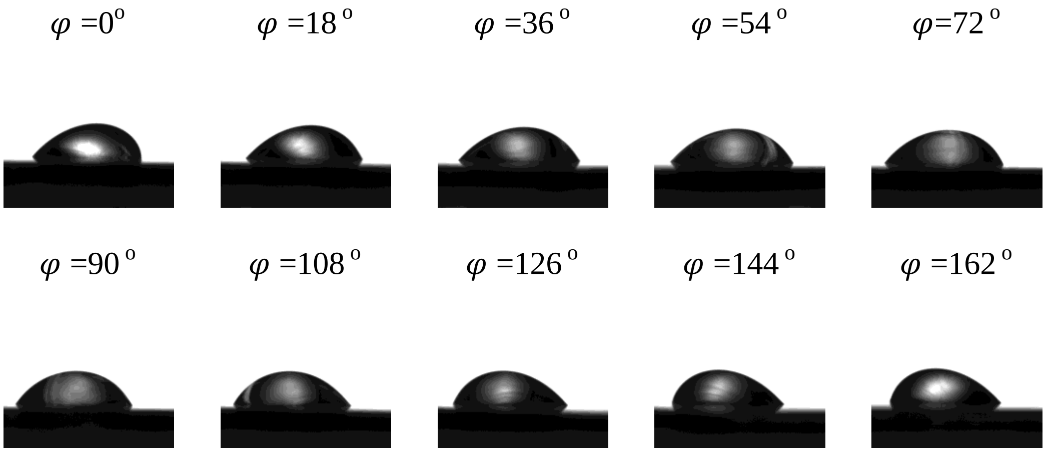

Fig. 2-5 Side view images of a 4µl water drop on aluminum substrate at different azimuthal angles (18^o intervals) are shown.

The challenge in finding the contact line radius, r_φ, from side view images is due to the perspective error in recording the location of the contact line [37, 38]. As shown in Fig. 2-6, when the observer's point of view (*i.e.* the camera) rotates by α degrees around the drop, the actual contact point (c_φ) rotates by φ degrees and not by α degrees. Moreover, as shown in Fig. 2-6b, the actual drop radius (r_φ) may appear longer than the apparent radius (r_α). As such, in reconstruction of the contact line, one measures a radius of length r_α at the azimuthal angle of α degrees, whereas the actual point's radius is r_φ and its associated azimuthal angle is φ (see Fig. 2-6b). The goal of this section is to provide a solution to the above issue (*i.e.* find r_φ and φ for a given α), beyond the state-of-the-art, *i.e.* [16] (see below). It should be noted that telecentric Lenses cannot address this perspective error as they cannot distinguish between c_φ and c_α since these point are along the same line [45].

Antonini *et al.* [16] for the first time developed a relation to find the value of contact line radius (*i.e.* r_φ) as a function of α. They used the fact that the tangent to the contact line at c_φ and observed drop radius (*i.e.* r_α) are perpendicular [16]. The minimization process for finding the r_φ in [16] was limited to drops with at least one axis of symmetry. In [16] particular, it was assumed the azimuthal locations at which observed and actual contact points have radii of the same length (*i.e.* $r_\alpha = r_\varphi$) are separated by an angle equal to π. This assumption holds for drops with at least one axis of symmetry, but this is not necessarily true for non-symmetrical drops (*e.g.* see Fig. 2-6).

Using the fact that the line of sight (or camera's angle) and tangent to the contact line at c_φ are parallel, one can extend the model in [16] to drops with convex contact lines of any arbitrary shape. The contact line convexity is necessary because if the contact line at some region is concave; it would not be entirely visible in the side view images. This is not a restriction, as even if the contact line could be found, finding the contact angle and the plane projection of the surface tension at that region would not be possible, *e.g.* see [46].

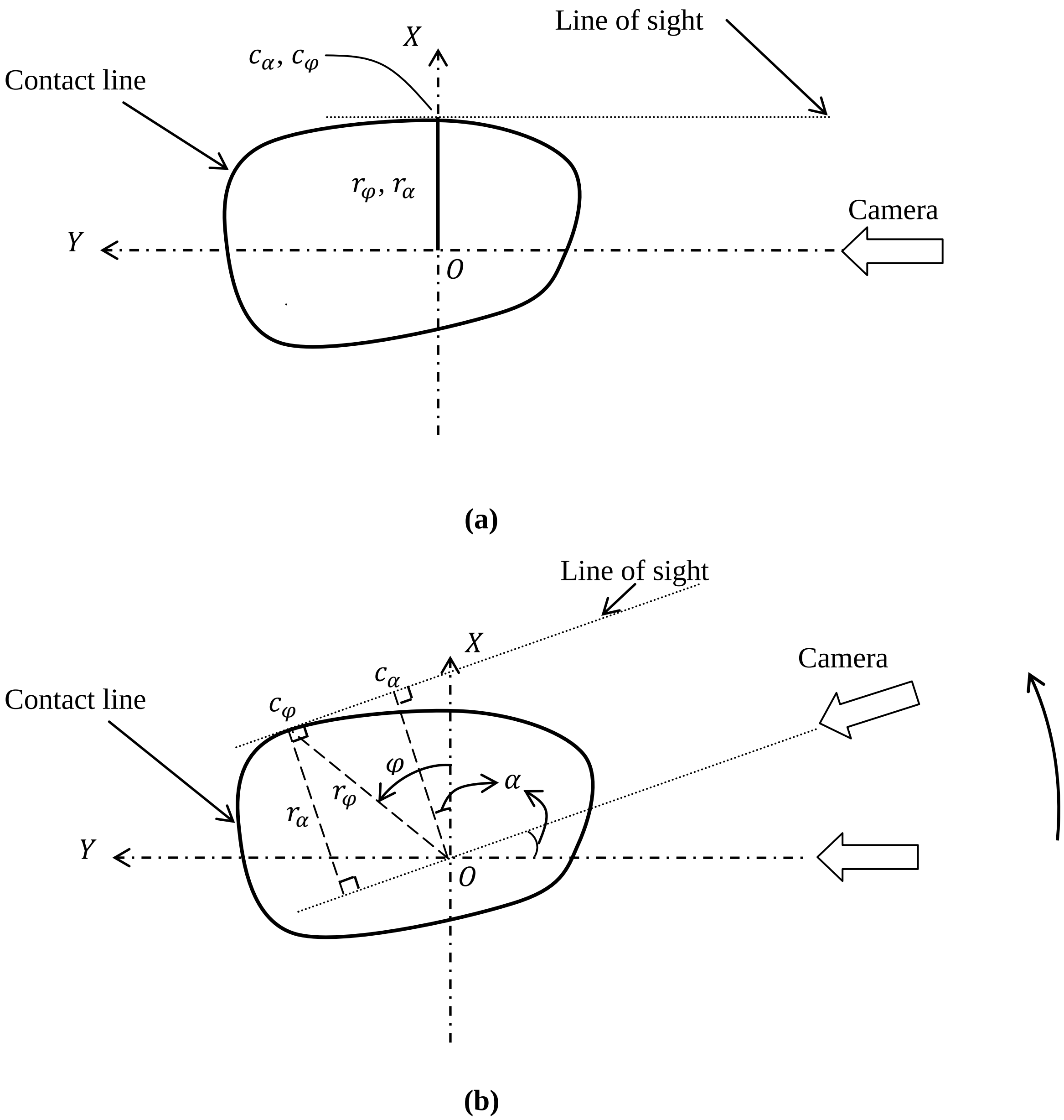

Fig. 2-6 Contact line of a drop with asymmetrical contact line is shown. (a) Camera is perpendicular to the X-axis, the drop radius (*i.e.* r_φ) is perpendicular to the line of sight. As such, the actual and observed contact radii are equal and the actual (c_φ) and observed (c_α) contact points are the same. (b) As camera rotates α degrees from its reference position, the observed drop radius (*i.e.* r_α) becomes shorter than the actual drop radius (*i.e.* r_φ). O is the projection of the apex on the drop base plane.

The proposed methodology needs a reference position for measuring the angle α. At the reference location, the radius Oc_{φ} should be perpendicular to the line of sight (or tangent to the contact line at c_{φ}), *e.g.* position 2 in Fig. 2-7. At this location, the observed and actual drop radii are coincident.

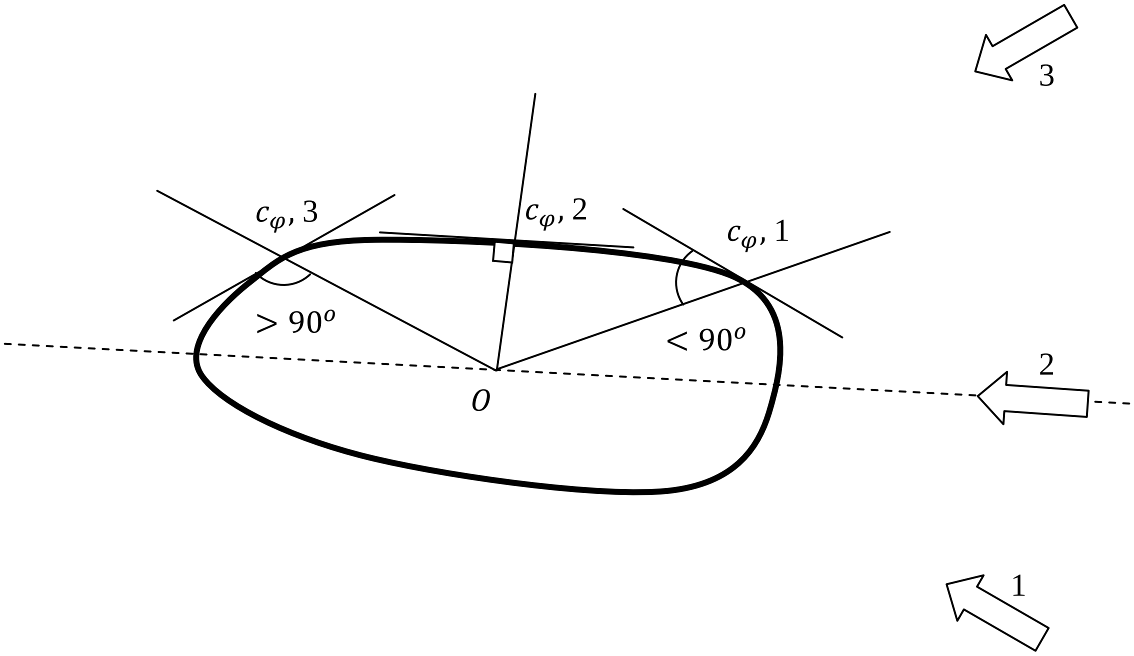

Fig. 2-7 Thick contour represents contact line of an arbitrary drop. By rotating the camera around the drop, (from position 1 to 3) the angle between the drop radius and camera increases from a value smaller than 90^{o} to a value larger than 90^{o}. As such, there is a camera position between 1 and 3 at which the angle between the drop radius and camera's direction is 90^{o}. Position 2 is the reference position for the camera. It should be noted that if camera is at the reference position, by rotating the camera to either side, the recorded drop radius increases. O is the projection of the apex on the drop base plane.

As explained below and shown in Fig. 2-7, for any given point inside the contact line which is a closed curve (*e.g.* O), there exists at least one point (*e.g.* c_φ) at which Oc_φ is perpendicular to the contact line. As shown in Fig. 2-7, where camera is at location 1, the angle between Oc_φ and tangent to the contact line at c_φ is acute ($< 90^o$). By rotating the camera to location 3, the angle becomes obtuse ($> 90^o$). Since the contact line is a smooth closed curve, according to intermediate value theorem (Bolzano's theorem), there must be a location (such as location 2) where Oc_φ is perpendicular to the contact line.

As shown in Figs. 2-6b, the relationship between the observed and the actual drop radii is:

$$r_\alpha = r_\varphi \cos(\varphi - \alpha) \tag{2-9}$$

It should be noted that the camera should be measured from the reference position explained in Fig. 2-7; otherwise Eq. 2-9 is not true. Differentiation of Eq. 2-9 with respect to α yields:

$$r'_\alpha = r_\varphi \sin(\varphi - \alpha) \tag{2-10}$$

where r'_α is the derivative of r_α with respect to α. The combination of Eqs. 2-9 and 2-10 gives:

$$\frac{r'_\alpha}{r_\alpha} = \tan(\varphi - \alpha) \tag{2-11}$$

By knowing the value of the ratio of $\frac{r'_\alpha}{r_\alpha}$, one can find the value of the angle φ corresponding to the camera rotation angle α using Eq. 2-11. In particular, the radius r_α can be approximated by Fourier series expansion:

$$S(\alpha) = \frac{a_0}{2} + \sum_{n=1}^{N} a_n \cos n\alpha + b_n \sin n\alpha \tag{2-12}$$

where $S(\alpha)$ is a parametric approximate for the observed contact line radius, N is the number of terms in the sequence (increasing the value of N, improves the contact line reconstruction up to $N = 6$, as shown in the Appendix A. For very large N values, *e.g.* $N > 14$, the number of Fourier coefficients becomes too large and minimization of Eq. 2-13 is not straightforward), a_0, a_n and b_n are the coefficients and may be found by minimization of the RMS difference between the function $r_\alpha(\alpha)$ and its series expansion (H in Eq. 2-13), with respect to the set of variables $\{a_0, a_1, \dots, a_N, b_1, \dots, b_N\}$:

$$H = \sum_{j=1}^{M} \left\{S(\alpha_j) - r_\alpha(\alpha_j)\right\}^2 \tag{2-13}$$

where α_j is the camera's angle at j^{th} azimuthal location, $r_\alpha(\alpha_j)$ is the observed radius in the 2-D image at α_j, and M is the number of images taken (at different azimuthal angles). Minimization is done in MatLab *fminsearch* script (the Math-Works, Inc.). Using Eqs. 2-11 to 2-13 one has φ as a function of α (camera's angle):

$$\varphi(\alpha) = \tan^{-1}\left(\frac{\sum_{n=1}^{N} -na_n \sin n\alpha + nb_n \cos n\alpha}{\frac{a_0}{2} + \sum_{n=1}^{N} a_n \cos n\alpha + b_n \sin n\alpha}\right) + \alpha \tag{2-14}$$

Using the value of $\varphi(\alpha)$ found from Eq. 2-14, along with Eq. 2-9 one may find value of the actual radius of the contact line at different azimuthal angles ($i.e.\ r_{\varphi}$).

2.6 Validation with Experiments

To validate the proposed model for reconstructing the contact line from side view images a "putty gel" surrogate for an asymmetric drop is used (to minimize the effect of evaporation); it was placed on a smooth aluminum substrate. The experimental setup, shown in Fig. 2-8, allowed taking drop images both from the side and from the top. The contact line had no symmetrical axes or concavities. The contact angle was smaller than 90^{o} to allow verification of results with the top view image.

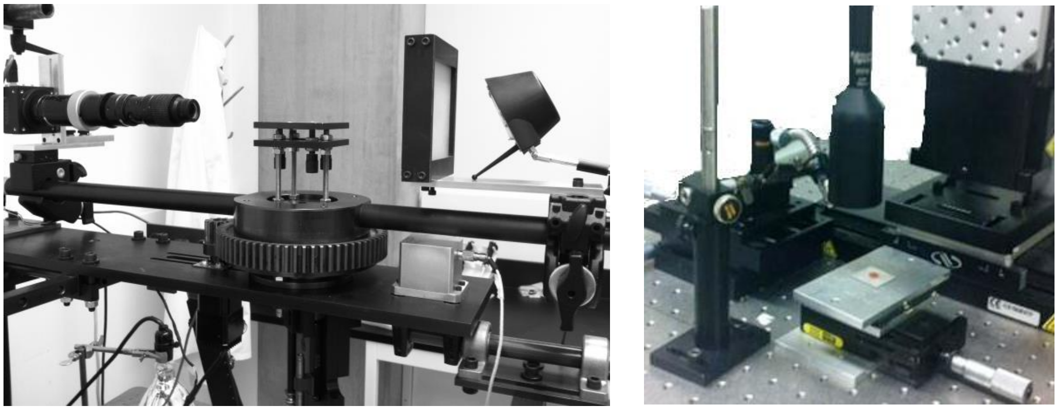

(a) (b)

Fig. 2-8 Experimental setup to record the (a) side view, (b) top view images from the surrogate (putty gel) drop is shown.

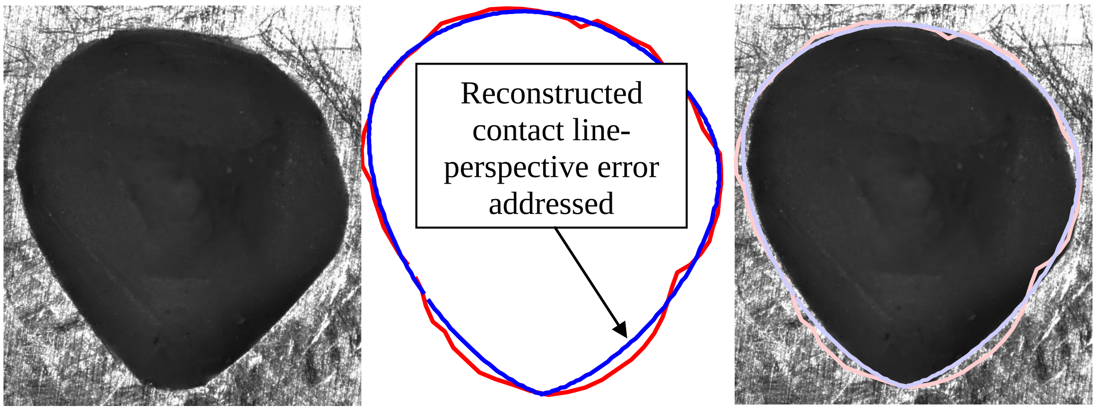

Fig. 2-9 (a) Top view of the putty drop on smooth aluminum substrate is shown. (b) The contact lines reconstructed from 2-D side view images with and without the perspective error are shown. (c) Reconstructed contact lines and top view image are shown and compared.

As shown in Fig. 2-9, due to the perspective error discussed in Section 2.5, the reconstructed contact line using 2-D side view images is not a faithful reconstruction of the true contact line. The model developed in [16] is unable to address the perspective error as the contact line of the surrogate for the drop (putty gel) has no axis of symmetry. As shown in the middle and left panels in Fig. 2-9, the model developed in this study is able to reconstruct the contact line with addressing the perspective error.

2.7 Contact Angle and Perspective Error

In this section, first it will be shown that rotating the camera azimuthally does not create any perspective error in measuring the contact angle. Then, the source of the perspective error in measuring the contact angle is discussed, and its magnitude is evaluated.

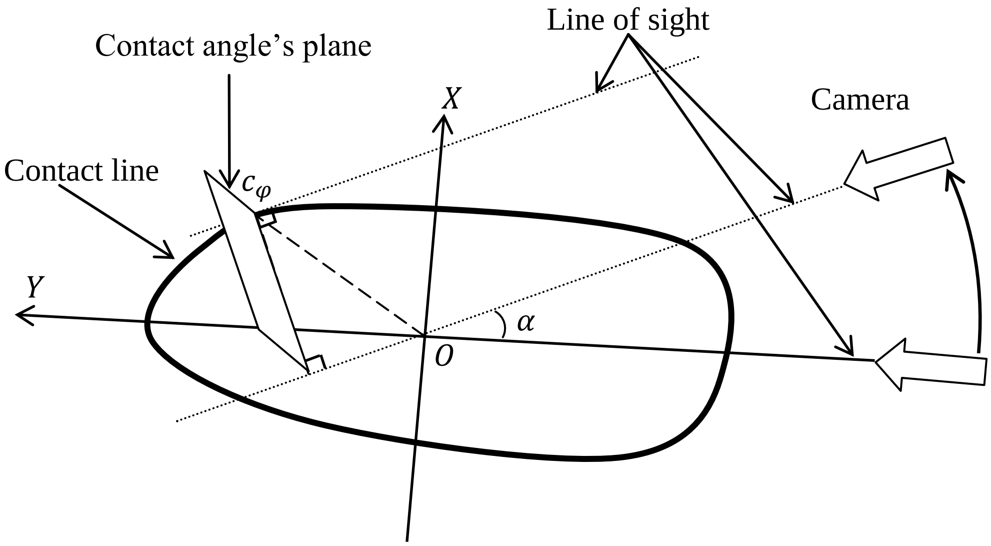

Fig. 2-10 A non-symmetric contact line and contact angle plane are shown. The contact angle plane is perpendicular to the line of sight; as such observed and actual contact angles are the same *i.e.* no perspective error in measuring the contact angle where camera is rotating in the substrate's plane (azimuthally).

As discussed in the previous section and shown in Fig. 2-10, the line of sight is perpendicular to the contact angle plane. As such, by rotating the camera azimuthally, at any azimuthal angle of the camera, the observed and the actual contact angles are the same.

In contact angle measurement methods based on image processing, the camera is tilted 1-6 degrees (back to front) to capture a portion of the reflected image. The reflected image is needed for detecting the edge contact points, as discussed for example in [46]. Tilting the camera may cause an error in reading the contact angle. In this section, the error associated with the back to front inclination of the camera is discussed.

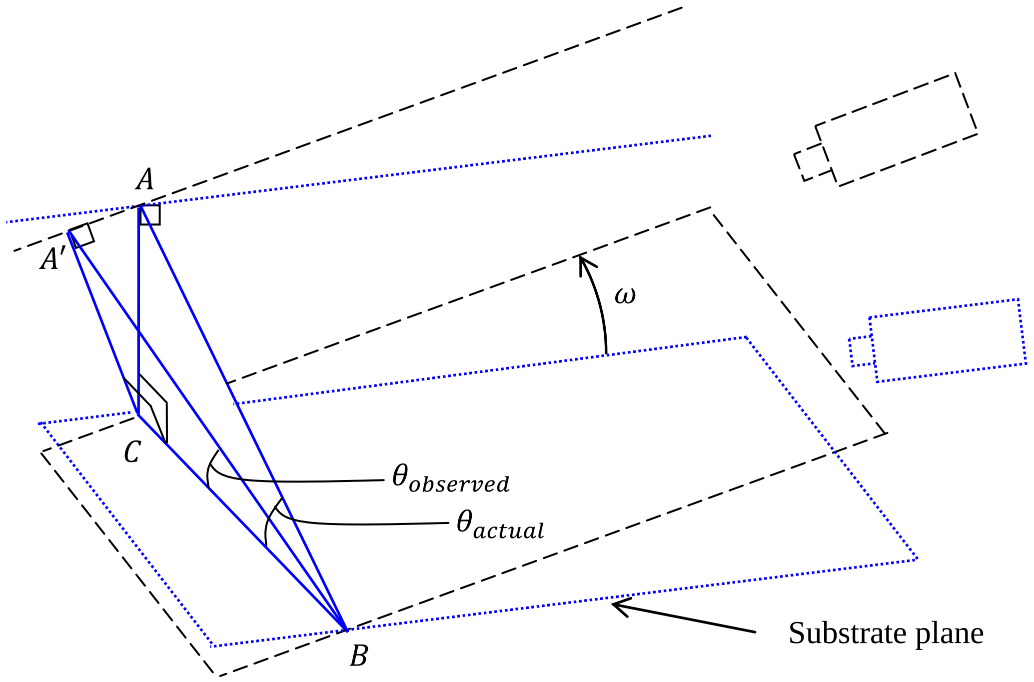

Fig. 2-11 The actual contact angle ($\angle CBA$) and the observed contact angle ($\angle CBA'$) due to back to front tilting the camera by ω are shown. Camera's rotation (ω) is out of the substrate's plane.

Figure 2-11 shows that by back to front tilting the camera by ω degrees, the line CA' is observed rather than CA. As such, instead of angle $\angle CBA$, angle $\angle CBA'$ is recorded. The difference between $\angle CBA$ (or θ_{actual}) and $\angle CBA'$ (or $\theta_{observed}$) is the perspective error due to the back-to-front tilt angle. From Fig. 2-11 one may find this perspective error as:

$$\tan\theta_{actual} = \frac{\tan\theta_{observed}}{\cos\omega} \tag{2-15}$$

where θ_{actual} is the actual contact angle and $\theta_{observed}$ is the observed contact angle after tilting the camera ω degrees back to front.

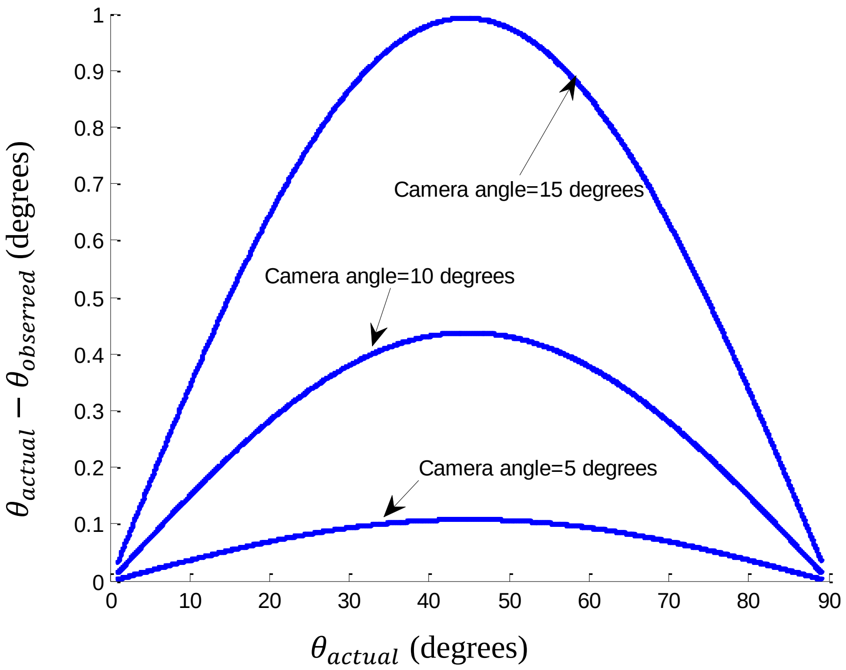

Fig. 2-12 The perspective error due to the back to front tilting the camera is shown. A tilt of as much as 10^{o} does not cause a significant error in measuring the contact angle.

As shown in Fig. 2-12, the $\theta_{observed}$ is always smaller than or equal to θ_{actual}. As understood from Eq. 2-15, the perspective error mentioned in this section depends on the value of the actual contact angle (*i.e.* θ_{actual}) and camera tilt angle (ω). Using Eq. 2-15, it was observed that even tilting the camera by 10^{o}

does not cause a significant error in measuring the contact angle (see Fig. 2-12). Also, the error is lower where the real contact angle is close to 0 and 90^o. It should be noted that the above discussion holds for contact angles smaller than 90^o, however it was found that the same occurs for contact angles larger than 90^o (small error for 90 and 180^o).

2.8 Conclusions

In this study, a model is developed to find the summation of surface tension forces along the contact line (drop adhesion force in the direction parallel to the substrate), for drops of arbitrary shape. In the case of drops with contact angles larger than 90^o, top view images cannot help one to find the contact line. As such, 2-D side view images are used in literature to reconstruct the contact line. Using the side view images at different azimuthal angles, the shape of contact line and the surface tension distribution along the contact line was found. For non-circular contact lines recording the drop radius introduces some perspective error. The model developed in literature for reconstructing the contact line with addressing this perspective error was only valid for drops with at least one axis of symmetry. The developed model in this study corrects this perspective error for any drop and contact line shape as long as there is no concave region on the contact line (curved towards the drop). On a separate segment, the potential perspective error in measuring the contact angle due to the back to front tilt of the camera was discussed. A tilt angle of $4^o - 6^o$ is a routine for capturing the contact point in 2-D side view images. It was found that for 10^o back to front tilt of camera, the maximum contact angle measurement error will be less than 1^o.

Acknowledgement

Authors would like to thank Natural Sciences and Engineering Research Council of Canada (NSERC) and CRC (Canada Research Chair) program for their financial support.

Appendix A-Effect of N (Number of Terms in the Fourier series) on Reconstruction of the Contact Line

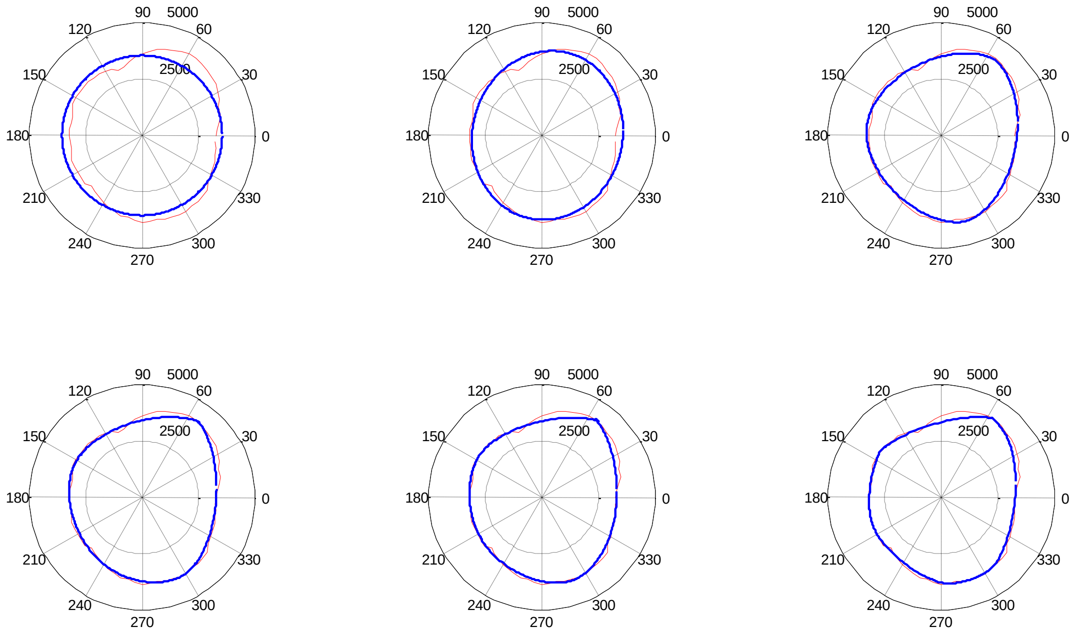

Fig. A1 The thick lines show the constructed contact lines with taking into account the perspective error using the methodology developed in section 3.3. From top left to bottom right N value changes from 2 to 7. For N values greater than 6, the constructed contact line only slightly changes. For very large N values (*e.g.* $N > 14$) the numerical model does not converge.

Appendix B- Perspective Error in Reconstruction of the Contact Line for the Specific Case of Elliptical Contact Line

To show the importance of correcting the perspective error in recording the contact line radius from the 2-D side view images, the specific case of elliptical contact line is studied analytically. The normal to the line of sight's projection of the actual contact line ($r_{\varphi \perp line\ of\ sight}$) is calculated as:

$$r_{\varphi \perp line\ of\ sight} = r_{\varphi}\ \cos(\varphi - \alpha) \qquad \text{(B2-1)}$$

Variation of φ from the value shown in Fig. B2-1b, results in the decrease of the value of $r_{\varphi \perp line\ of\ sight}$. As such, at φ, $r_{\varphi \perp line\ of\ sight}$ is at a local maximum. Therefore, one has:

$$\frac{\partial(r_{\varphi}\ \cos(\varphi - \alpha))}{\partial \varphi} = 0 \qquad \text{(B2-2)}$$

Using Eqs. 2-5 and B2-2 one has:

$$\frac{-ab\sin(\varphi - \alpha)}{\sqrt{a^2\cos^2\varphi + b^2\sin^2\varphi}} + \frac{ab\ \cos(\varphi - \alpha)\,(2a^2\sin\varphi\ \cos\varphi - 2b^2\sin\varphi\cos\varphi)}{-2\sqrt{(a^2\cos^2\varphi + b^2\sin^2\varphi)^3}} = 0 \qquad \text{(B2-3)}$$

Using some trigonometry identities, Eq. B2-3 simplifies to:

$$a^2\cos\varphi\sin\alpha - b^2\sin\varphi\cos\alpha{=}0 \qquad \text{(B2-4)}$$

Therefore, the following relation is found for φ at different α:

$$\varphi = \tan^{-1}\{(a/b)^2\tan\alpha\} \qquad \text{(B2-5)}$$

As expected for a drop with a circular contact line (*i.e.* $a/b = 1$), $\varphi - \alpha$ is zero (see Fig. B2-1a). By increasing the a/b, the difference between $\varphi - \alpha$ increases. Using Eqs. B2-5, one may find the ratio of the actual contact line radius to the observed contact line radius (*i.e.* $\frac{r_{\varphi}}{r_{\alpha}}$) at different camera's angles (*e.g.* Fig. B2-1b).

As shown in Fig. B2-1b, for a drop with an elliptical shape contact line, with $a/b = 3$, the actual contact line radius may be 1.7 times larger than the observed contact line radius.

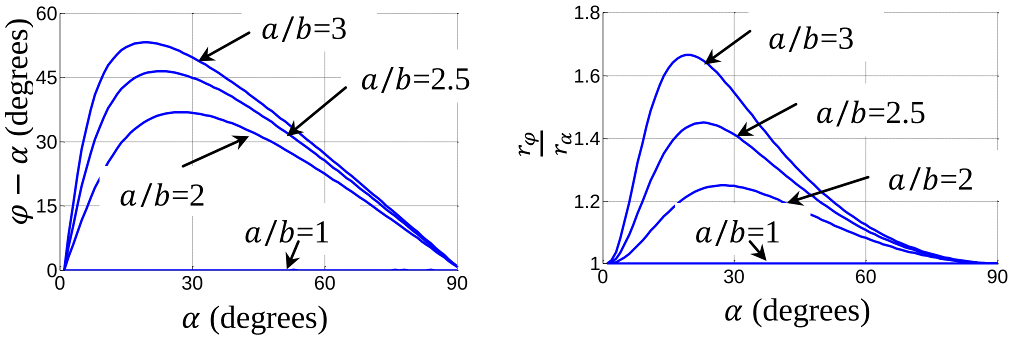

(a) (b)

Fig. B2-1 (a) The $\varphi - \alpha$ versus α (camera's angle) and (b) ratio of the drop's actual radius to the observed radius (*i.e.* $\frac{r_\varphi}{r_\alpha}$) for different a/b at different α are shown. The drop contact line has an elliptical shape and a and b are the major and minor radii, accordingly.

2.9 References

[1] Tan, S. C., 2005, "Effects of large droplet dynamics on airfoil impingement characteristics," 43rd AIAA Aerospace Sciences Meeting and Exhibit - Meeting Papers, Anonymous pp. 8389-8401.

[2] Lan, H., Friedrich, M., Armaly, B. F., 2008, "Simulation and Measurement of 3D Shear-Driven Thin Liquid Film Flow in a Duct," International Journal of Heat and Fluid Flow, **29**(2) pp. 449-459.

[3] Kumbur, E. C., Sharp, K. V., and Mench, M. M., 2006, "Liquid Droplet Behavior and Instability in a Polymer Electrolyte Fuel Cell Flow Channel," Journal of Power Sources, **161**(1) pp. 333-345.

[4] Witten, T., 2003, "Coffee Drops: Dispersions and Evaporative Flows," **2012**.

[5] White, E. B., and Schmucker, J. A., 2008, "A Runback Criterion for Water Drops in a Turbulent Accelerated Boundary Layer," Journal of Fluids Engineering, Transactions of the ASME, **130**(6) .

[6] Kolev, V. L., Kochijashky, I. I., Danov, K. D., 2003, "Spontaneous Detachment of Oil Drops from Solid Substrates: Governing Factors," Journal of Colloid and Interface Science, **257**(2) pp. 357-363.

[7] Kralchevsky, P. A., Danov, K. D., Kolev, V. L., 2005, "Detachment of Oil Drops from Solid Surfaces in Surfactant Solutions: Molecular Mechanisms at a

Moving Contact Line," Industrial and Engineering Chemistry Research, **44**(5) pp. 1309-1321.

[8] Gao, L., and McCarthy, T. J., 2009, "An Attempt to Correct the Faulty Intuition Perpetuated by the Wenzel and Cassie "Laws"," Langmuir, **25**(13) pp. 7249-7255.

[9] Gao, L., and McCarthy, T. J., 2007, "How Wenzel and Cassie were Wrong," Langmuir, **23**(7) pp. 3762-3765.

[10] Pease, D. C., 1945, "The Significance of the Contact Angle in Relation to the Solid Surface," Journal of Physical Chemistry, **49**(2) pp. 107-110.

[11] Bartell, F. E., and Shepard, J. W., 1953, "Surface Roughness as Related to Hysteresis of Contact Angles. II. the Systems Paraffin-3 Molar Calcium Chloride Solution-Air and Paraffin-Glycerol-Air," Journal of Physical Chemistry, **57**(4) pp. 455-458.

[12] Bartell, F. E., and Shepard, J. W., 1953, "Surface Roughness as Related to Hysteresis of Contact Angles. I. the System Paraffin-Water-Air," Journal of Physical Chemistry, **57**(2) pp. 211-215.

[13] Extrand, C. W., 2003, "Contact Angles and Hysteresis on Surfaces with Chemically Heterogeneous Islands," Langmuir, **19**(9) pp. 3793-3796.

[14] Cheng, D. F., and McCarthy, T. J., 2011, "Using the Fact that Wetting is Contact Line Dependent," Langmuir, **27**(7) pp. 3693-3697.

[15] Princen, H. M., 1999, "Spinning Drop Method Applied to Three-Phase Fluid Equilibria," Langmuir, **15**(21) pp. 7386-7391.

[16] Antonim, C., Carmona, F. J., Pierce, E., 2009, "General Methodology for Evaluating the Adhesion Force of Drops and Bubbles on Solid Surfaces," Langmuir, **25**(11) pp. 6143-6154.

[17] Chen, S. C., and Lin, J. F., 2008, "Detailed Modeling of the Adhesion Force between an AFM Tip and a Smooth Flat Surface Under Different Humidity Levels," Journal of Micromechanics and Microengineering, **18**(11) .

[18] Rabinovich, Y. I., Adler, J. J., Ata, A., 2000, "Adhesion between Nanoscale Rough Surfaces. I. Role of Asperity Geometry," Journal of Colloid and Interface Science, **232**(1) pp. 10-16.

[19] Rabinovich, Y. I., Adler, J. J., Ata, A., 2000, "Adhesion between Nanoscale Rough Surfaces: II. Measurement and Comparison with Theory," Journal of Colloid and Interface Science, **232**(1) pp. 17-24.

[20] Freitas, A. M., and Sharma, M. M., 2001, "Detachment of Particles from Surfaces: An AFM Study," Journal of Colloid and Interface Science, **233**(1) pp. 73-82.

[21] Yadav, P. S., Bahadur, P., Tadmor, R., 2008, "Drop Retention Force as a Function of Drop Size," Langmuir, **24**(7) pp. 3181-3184.

[22] Dimitrakopoulos, P., 2007, "Deformation of a Droplet Adhering to a Solid Surface in Shear Flow: Onset of Interfacial Sliding," Journal of Fluid Mechanics, **580**pp. 451-466.

[23] Baxter, S., 1950, "Wetting and Contact-Angle Hysteresis," Nature, **165**(4188) pp. 198.

[24] Marmur, A., 1997, "Line Tension and the Intrinsic Contact Angle in Solid-Liquid-Fluid Systems," Journal of Colloid and Interface Science, **186**(2) pp. 462-466.

[25] Amirfazli, A., Keshavarz, A., Zhang, L., 2003, "Determination of Line Tension for Systems Near Wetting," Journal of Colloid and Interface Science, **265**(1) pp. 152-160.

[26] Oguz, H. N., and Sadhal, S. S., 1988, "Effects of Soluble and Insoluble Surfactants on the Motion of Drops." Journal of Fluid Mechanics, **194**pp. 563-579.

[27] Chou, T., 2001, "Geometry-Dependent Electrostatics Near Contact Lines," Physical Review Letters, **87**(10) pp. 106101/1-106101/4.

[28] Bateni, A., Laughton, S., Tavana, H., 2005, "Effect of Electric Fields on Contact Angle and Surface Tension of Drops," Journal of Colloid and Interface Science, **283**(1) pp. 215-222.

[29] Wenzel, R. N., 1949, "Surface Roughness and Contact Angle," Journal of Physical & Colloid Chemistry, **53**(9) pp. 1466-1467.

[30] Cassie, A. B. D., 1948, "Contact Angles," Discussions of the Faraday Society, **3**pp. 11-16.

[31] Gao, L., and McCarthy, T. J., 2006, "Contact Angle Hysteresis Explained," Langmuir, **22**(14) pp. 6234-6237.

[32] MacDougall, G., and Okrent, C., 1942, Proc. R. Soc. London, **180A**.

[33] Brown, R. A., Orr Jr., F. M., and Scriven, L. E., 1980, "Static Drop on an Inclined Plate: Analysis by the Finite Element Method," Journal of Colloid and Interface Science, **73**(1) pp. 76-87.

[34] Extrand, C. W., and Gent, A. N., 1990, "Retention of Liquid Drops by Solid Surfaces," Journal of Colloid and Interface Science, **138**(2) pp. 431-442.

[35] Chen, K. S., Hickner, M. A., and Noble, D. R., 2005, "Simplified Models for Predicting the Onset of Liquid Water Droplet Instability at the Gas Diffusion layer/gas Flow Channel Interface," International Journal of Energy Research, **29**(12) pp. 1113-1132.

[36] ElSherbini, A. I., and Jacobi, A. M., 2004, "Critical Contact Angles for Liquid Drops on Inclined Surfaces," Progress in Colloid and Polymer Science, **128**pp. 57-62.

[37] ElSherbini, A. I., and Jacobi, A. M., 2004, "Liquid Drops on Vertical and Inclined Surfaces: II. A Method for Approximating Drop Shapes," Journal of Colloid and Interface Science, **273**(2) pp. 566-575.

[38] ElSherbini, A. I., and Jacobi, A. M., 2004, "Liquid Drops on Vertical and Inclined Surfaces: I. an Experimental Study of Drop Geometry," Journal of Colloid and Interface Science, **273**(2) pp. 556-565.

[39] Extrand, C. W., and Kumagai, Y., 1995, "Liquid Drops on an Inclined Plane: The Relation between Contact Angles, Drop Shape, and Retentive Force," Journal of Colloid and Interface Science, **170**(2) pp. 515-521.

[40] ElSherbini, A. I., and Jacobi, A. M., 2006, "Retention Forces and Contact Angles for Critical Liquid Drops on Non-Horizontal Surfaces," Journal of Colloid and Interface Science, **299**(2) pp. 841-849.

[41] Dussan V., E. B., 1983, "Moving contact line." Publications of the Mathematics Research Center, University of Wisconsin-Madison, Anonymous pp. 303-324.

[42] Dussan, V. E. B., and Chow, R. T., 1983, "On the Ability of Drops Or Bubbles to Stick to Non-Horizontal Surfaces of Solids." Journal of Fluid Mechanics, **137**pp. 1-29.

[43] Bateni, A., Susnar, S. S., Amirfazli, A., 2003, "A High-Accuracy Polynomial Fitting Approach to Determine Contact Angles," Colloids and Surfaces A: Physicochemical and Engineering Aspects, **219**(1-3) pp. 215-231.

[44] Alvarez, J. M., Amirfazli, A., and Neumann, A. W., 1999, "Automation of the Axisymmetric Drop Shape Analysis-Diameter for Contact Angle Measurements," Colloids and Surfaces A: Physicochemical and Engineering Aspects, **156**(1-3) pp. 163-176.

[45] Jan 2012, "Telecentricity and Telecentric Lenses in Machine Vision," .

[46] Chini, S. F., and Amirfazli, A., 2011, "A Method for Measuring Contact Angle of Asymmetric and Symmetric Drops," Colloids and Surfaces A: Physicochemical and Engineering Aspects, **388**(1-3) pp. 29-37.

Chapter 3 - A Method for Measuring Contact Angle of Asymmetric and Symmetric Drops[1]

3.1 Introduction

Contact angle (θ) is the angle between the solid surface and liquid-air interface, measured through the liquid phase. Contact angle is a measure of wettability of a solid surface; it is also used to predict drop evolution during evaporation [1] and determines the adhesion force between a drop and solid surface [2]. For other applications see [3-7]. As will be shown, state-of-the-art contact angle measurement techniques mostly use a drop to determine the contact angle value. The reason is that drop methods require a very simple setup and a small amount of liquid and surface (*e.g.* see Fig. 3-1). This study is focused on measuring the contact angle of drops; as such, it will not discuss other methods such as Wilhelmy plate method, ring method, etc. (interested readers can see *e.g.* Chap. 10 of [8]). However, the findings can be extended to the contact angle measurement of bubbles. Depending on the surface and external force on a drop, drop may be symmetrical (see Fig. 3-1a) or asymmetrical (see Fig. 3-1b). As will be shown the challenge in contact angle measurements is mostly for asymmetrical drops. Contact angle measurement methods found in literature can be grouped into tensiometry and goniometry methods.

---

[1] A version of this chapter has been published. Chini and Amirfazli 2011. Colloids Surfaces A., 338, 29-37.

3.2 Tensiometry Methods

Tensiometry methods find the contact angle value using Young Equation (Eq. 3-1).

$$\boldsymbol{\gamma_{SL}} + \boldsymbol{\gamma} \cos \theta_Y = \boldsymbol{\gamma_{SV}} \qquad (3\text{-}1)$$

where $\boldsymbol{\gamma_{SV}}$, $\boldsymbol{\gamma}$ and $\boldsymbol{\gamma_{SL}}$ are solid-vapor, liquid-vapor and solid-liquid surface tension forces, respectively; θ_Y is the intrinsic contact angle (see Fig. 3-1a). A complete list of tensiometry methods can be found in [8].

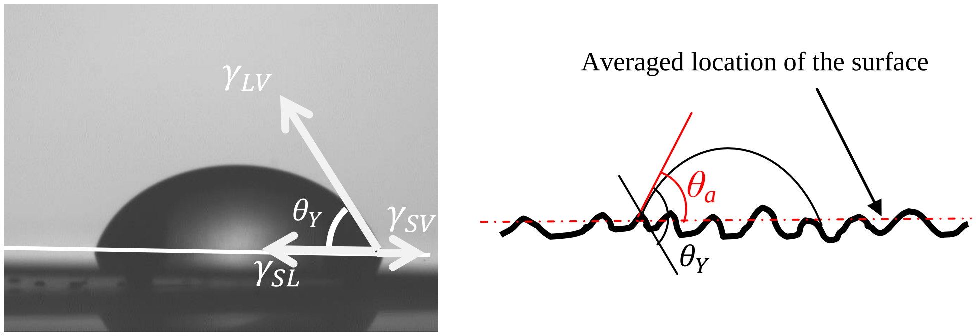

(a) (b)

Fig. 3-1 A water drop on a smooth Al surface with its reflection on the surface is shown where (a) no external force parallel to the surface is present, (b) Apparent (θ_a) and intrinsic ($\boldsymbol{\theta_Y}$) contact angles on a rough surface are shown.

As long as surface/interfacial tensions do not change, the intrinsic contact angle (θ_Y, see Fig. 3-1c) is constant and can be found from Eq. 3-1. But, there are two problems: First, the values of surface/interfacial tensions are not readily available (especially $\boldsymbol{\gamma_{SV}}$). Second, impurity [9], line tension[10-12] adsorption of the vapor onto the solid phase [13], electrostatic potential [14], surface roughness [15], heterogeneity [16] and external force will result in observed or apparent contact angle (θ_a in Fig. 3-1c). Surface roughness and heterogeneity result in observing different contact angles when contact line advances or recedes on a surface. The largest and smallest possible contact angles on a surface are called advancing and receding contact angles, accordingly (the difference between advancing and receding contact angles is known as the contact angle hysteresis). These different contact angle values are different from the value found using Eq. 3-1. Also, for a broad range of applications such as drops on heat-exchangers or pesticides on plant leaves, where surfaces are inclined, the presence of contact angle hysteresis causes the observed contact angle to be different at different locations along the contact line [2] and tensiometry methods are generally unable to find the contact angles for such cases.

3.3 Goniometry Methods

In goniometry methods contact angle is observed and measured from the 2-D side view image of drops on the solid surface (*e.g.* see Fig. 3-1a and b). Modern literature methods for measuring the contact angle of drops (and in general hanging, pendant and captive drops and bubbles) can be categorized into two groups: (i) analytical-image processing and, (ii) exclusively image processing methods. Analytical-image processing methods require a few of the liquid properties (*e.g.* the value of surface tension), and are usually unable to measure the contact angle of asymmetric drops (*e.g*. drops on inclined surfaces; see Fig. 3-1b). Image processing methods do not have such a limitation. As such, image processing methods are more general. However, for the completeness, in the following, one of the main analytical-image processing contact angle measurement methods is briefly discussed.

3.4 Analytical-image processing methods

Rotenberg *et al.* [17] developed *ADSA* (axisymmetric drop shape analysis) which finds the contact angle of axisymmetric drops. *ADSA* constructs an objective function which is the error between the observed and theoretical (Laplacian) drop boundary. Minimization of the objective function in *ADSA* was based on Newton-Raphson with initial value or shooting method [17]. As such, it required a good initial approximation to the drop profile which made the technique sensitive to noise. del Rio and Neumann [18] used Levenberg-Marquardt method with finite difference, and resolved the initial approximation problem (the method was called *ADSA-HD*). *ADSA* was limited to drops with distinguishable apex until the recent version *ADSA-NA* or *ADSA-no apex* [19]. *ADSA* (*ADSA-EF*) was also used to find the contact angle when an electric field is present [20]. However, due to nature of the method, *ADSA* is limited to axisymmetric shape drops. Also, for nearly spherical drop shapes Laplace equation does not easily converge and *ADSA* may be inaccurate in this range [21]. This may be the case for small drops placed on a superhydrophobic surface.

3.5 Image processing methods

Image processing methods are potentially able to measure the contact angle of any drop with any shape (symmetric or not). Therefore, image processing methods can be versatile when implemented properly. In the following, the state-of-the-art image processing methods for measuring contact angles are discussed.

Li *et al.* [22], and Goclawski and Urbaniak-Domagala [23] used a function describing a circle to fit the drop profile data (drop boundary is found using marker-controlled watershed transform). The main advantage of this method say compared to *ADSA* is the speed of implementation, but accuracy is somewhat compromised (especially for larger drops where due to the gravity, drop profile shape is not circular) [24]. The other limitation is that it is not really applicable to asymmetrical drops. Iliev and Pesheva [25] suggested a model for determination of local contact angle of drops with knowing the shape of contact line and volume of drop. However, due to the following reason, their model is not proper for asymmetric drops. The contact line in [25] is constructed from the drop side view images. However, for asymmetric drops, as shown in [2] construction of the contact line has some perspective error which is not considered in [25].

Bateni *et al.* [26] developed a method called *APF* (Automated Polynomial Fitting). In their method, *LOG* (Laplacian of Gaussian) was used to find the drop boundary in a region near the contact line which was 35X magnified. Polynomials (1st-6th order) were fitted to the drop boundary to find the contact angle. Bateni *et al.* [26] developed an algorithm to find the contact (three-phase) point automatically. The method developed by Bateni *et al.* [26] and methods based on their algorithm (*e.g.* Schuetter *et al.* [27]) were sensitive to the order of polynomial and the number of pixels used to fit the polynomial. However, the relation between polynomial order and number of pixels to use was not well defined for all ranges of contact angle. Also, only contact angle and contact point on one side of the drop may be found at a time. So, *APF* cannot find the baseline, and assumes that the baseline is horizontal. Baseline is important as contact angle is the angle between the tangent to the boundary at the contact point and the baseline. Stalder *et al.* [28] developed a “snakes” based approach to find the drop boundary (*i.e.* Drop Snake). “Gradient Vector Flows”, “Snakes” or “Active Contours” are computer-generated curves that move within the image to find the object boundaries [29]. Stalder *et al.* [28] fitted a B-spline curve to the drop boundary and found the contact angle. In “Drop Snake”, user should pick the contact and a few boundary points manually which makes the method susceptive to human error. One of the conventional methods for measuring the advancing and receding contact angles is adding and removing volume to/from a sessile drop with a needle embedded in the drop. “Drop Snake” is unable to measure the contact angle, if a needle is inside the drop from top. The software developed by the “First Ten Angstroms” (FTÅ-200 [30, 31]) fits a mathematical expression to the drop boundary and calculates the slope of the tangent to the drop at the contact point. It is user-friendly and produces accurate results for a wide range of contact angles. However, user should pick the baseline and a few boundary points which could make the method susceptible to human error. Also, user should select the drop boundary function *i.e.* one of the two built-in functions: Laplacian (similar to *ADSA*) or circular. In UTHSCSA ImageTool [32], user should pick the baseline, contact points and a line tangent to the drop profile manually. Even though, the method is very accurate and useable for any drop shape, it is time consuming and can be sensitive to human error. In general all the methods that user should pick points are usually not suitable for automated computer implementation or process of a set of image files in a folder.

In the next section, an image processing method is described. It automatically measures the contact angle of symmetric and asymmetric drops without the need to know any of drop property values, selecting any point on the boundary, and it works for all ranges of contact angles. The method is named “*SPPF*” (sub-pixel polynomial fitting). It measures the left side and right side contact angles (simultaneously), wetted width, drop height and the baseline inclination angle (needed as the contact angle should be measured with respect to the baseline) of symmetric and asymmetric drops.

3.5.1 SPPF (Sub-Pixel Polynomial Fitting) Method

First, an overall description of *SPPF* is given. This is followed by details involved in each step. In the first step drop boundary is found using “Canny” edge detection method with Otsu's threshold [33]; see Fig. 3-2. In [34] it was shown that finding the drop boundary in pixel resolution may results in an apparent difference of almost 5° in the determined contact angle. As such, in this study drop boundary is found in sub-pixel resolution. Location of the drop boundary with sub-pixel resolution was found using saddle point of the sigmoid of pixel intensity (the saddle point has the highest pixel intensity change, see supplementary materials [35]). The sigmoid model will be implemented in the procedure as its goodness is already verified (see Section 2.1). Regarding the verification of the sigmoid model, it should be noted that the sigmoid model was tested with pin gages with standard sizes. The reason of using pin gages was that the exact dimensions were known whereas for drops that is not the case. It was found that compared to the pixel resolution (Canny with threshold) method, the sub-pixel (sigmoid) method measured the pins' diameters with a higher accuracy and resolution. Since, images taken from pin gages were comparable with real drops in terms of size and pixel lighting intensity, we can extend the methodology to drop images. Smoothen edge was constructed from the resultant jagged edge using Savitzky-Golay filter [36]. Contact points were found by extrapolation and intersecting the drop boundary with its reflection. First to forth order polynomials were fitted to the smoothen edge of drop boundary to calculate the contact angle. It was found that the 2nd order polynomial was better for fitting the drop boundary and calculating the contact angle. Optimum number of pixels needed for fitting a polynomial was found by studying the change of contact angle versus pixel numbers used to fit the 2nd order polynomial. The "*SPPF*" was tested with (i) certified fixed drop calibration reference tool of ramé-hart instrument Co. (which includes 4 images of sessile drops with nominal contact angles of 30 °, 60 °, 90 ° and 120°), (ii) synthetic drops with known contact angles (between 10° and 170°) generated by intersecting two circles (see Appendix A), and (iii) natural symmetric drops with known contact angles found from other methods. Use of the median filter (which preserves the drop boundary and removes noise) makes the *SPPF* method robust to a reasonable level of noise (*i.e.* Gaussian noise with variance of 0.09).

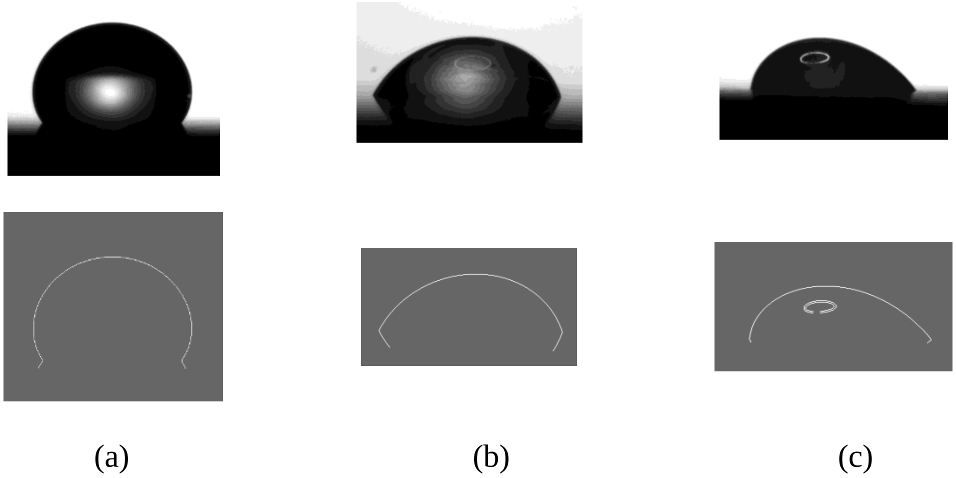

Fig. 3-2 Drop boundary for three cases of (a) hydrophobic, (b) hydrophilic and (c) drop on an inclined surface, is found using Canny with threshold method. Note in (c) the camera was rotated with the surface.

3.5.1.1 Detecting the Drop Boundary

For finding the drop boundary, in this study, the following edge detection methods were studied: Sobel, Prewitt, Roberts, Laplacian of Gaussian, and Canny with and without threshold (see supplementary materials [35]). For other edge detection methods see Atae-Allah *et al.* [37]. It was found through study of a collection of drops with contact angles between 10^o and 160^o that Canny with threshold is the best method for finding the drop boundary near the three-phase (contact) line. This was regardless of the lighting condition as for a reasonable lighting, image adjustment is performed to minimize the sensitivity of images to variation of light intensity (see online Supplementary Material). Threshold is found using Otsu's method [33] as implemented in MATLAB R2008b. In Otsu’s method the threshold is chosen such that the intraclass variance of the black and white pixels are minimized. Above algorithms (*e.g.* Canny) define the location of the drop boundary in pixel resolution. For having a higher accuracy in calculating the contact angle, in this study, drop boundary near the contact line is found in sub-pixel resolution. For contact angles close to 0^o and 180^o, the sub-pixel location of the drop boundary should be found in the vertical direction; and in horizontal direction for contact angles close to 90^o. It was observed that for contact angles far from 0^o, 90^o and 180^o, let's say 30^o, finding the sub-pixel location of drop boundary in vertical and horizontal directions result in similar contact angle values. In this study, initially the drop boundary in pixel resolution is used to find the approximate contact angle values. For the approximate contact angle values between 45^o and 135^o, the sub-pixel location of the drop boundary is found in the horizontal direction (*e.g.* see the inset in Fig. 3-3); and in the vertical direction where the approximate contact angle is smaller than 45^o or larger than 135^o. For finding the sub-pixel location of the drop boundary in horizontal and vertical directions, the following methodology is applied.

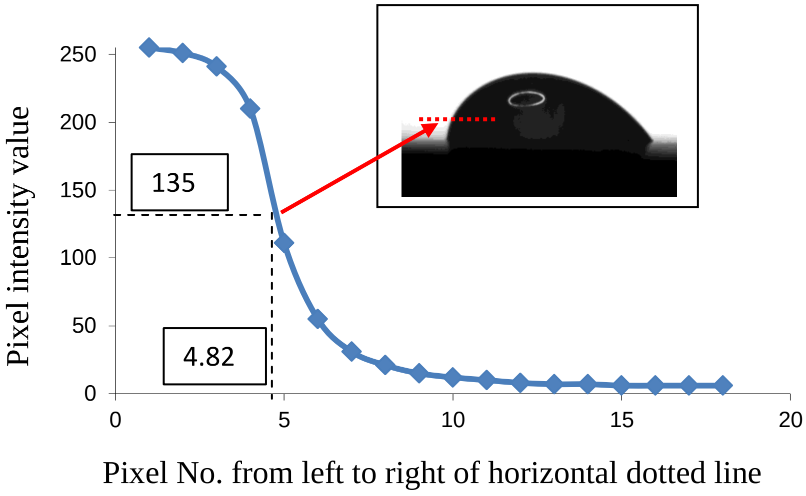

Fig. 3-3 Pixel intensity values along a horizontal line crossing the boundary of a drop (dotted line in the inset) are shown. The saddle point of the sigmoid shape pixel intensity curve is the sub-pixel location of the drop boundary. It should be noted that the left contact angle of the drop shown in the insert is between 45^o and 135^o (approximate value is found using the drop boundary in pixel resolution); as such sub-pixel location of drop boundary is found in horizontal location.

Each pixel in the gray scale image has a value between 0 (for pure black) to 255 (for pure white). A sigmoid function fitted to the gray level intensities of pixels on a horizontal or vertical line crossing the boundary depending on the contact angle (*e.g.* see Fig. 3-3). Saddle point of the sigmoid shape curve (shown in Fig. 3-3) locates the sub-pixel location of the boundary. The reason is that the saddle point has the highest color intensity change which by definition is the meaning of the drop boundary. It should be noted that a similar methodology was used by Kalantarian *et al.* [19] to find the sub-pixel location of the drop boundary.

However, they considered the midpoint of the sigmoid as the location of the drop boundary which in general is not equal to the saddle point (or highest color intensity change). It was found that the difference between the saddle point and midpoint is not very large. Since, the complexity of calculating the saddle point and midpoint is almost equal and saddle point by definition is the drop boundary, it is preferred to use the saddle point rather than the midpoint. Procedure of finding the sub-pixel location of the drop boundary is checked with pin gages with known diameters purchased from Meyer Gage Co. (see Table 3-1). The size of pin gages was comparable with the size of the studied drops. Using a calibration grid (grid size was 250µm×250µm) the physical dimension of each pixel was found to be 23µm. As such, in pixel resolution, measurement resolution was at best 23µm (at 4.5X time magnifications and for a Basler A302fs camera). However, in sub-pixel resolution (with two decimals), measurement resolution is in the order of 1µm or less. Comparing pixel and sub-pixel resolution algorithms, it was found that the maximum absolute error in calculating the diameter of pin gages were 80µm (1.3%) and 8µm (0.1%) for pixel and sub-pixel resolutions, respectively. The next step is detecting the three-phase (contact) points.

Table 3-1 Comparison of pixel and sub-pixel resolution methods in finding the pin diameters. Pin gage diameters are provided by the manufacturer (Meyer Gage Co.). The camera used was a Basler A302fs and magnification was 4.5X.

	Absolute error (μm)		Error (%)	
Pin diameter (μm)	Pixel resolution	Sub-pixel resolution	Pixel resolution	Sub-pixel resolution
3247±1	27	5	0.8	0.1
4206±1	51	1	1.2	0.0
5117±1	65	6	1.3	0.1
6235±1	80	8	1.3	0.1

3.5.1.2 Finding the Three-Phase (Contact) Points

Finding the exact location of the contact points is important in measuring an accurate contact angle [26]. For an automatic detection of the three-phase (contact) point, the following algorithm is developed: *SPPF* uses the reflection of the drop off the surface (see Fig. 3-2b for a clear example) to find the rough contact points (see “×” in Fig. 3-4a). Using the left and right contact points, baseline is found (see Fig. 3-4a). Then *SPPF* finds the exact location of the contact point by extrapolating the drop boundary and intersecting it with the baseline (see “×” in Fig. 3-4b). For the cases that reflection is not visible, user should pick the contact points manually. This is not really suggested as it makes the method susceptible to human error. As such, images should be taken such that the reflection is observable. This point is further discussed in section 3.5.1.4.

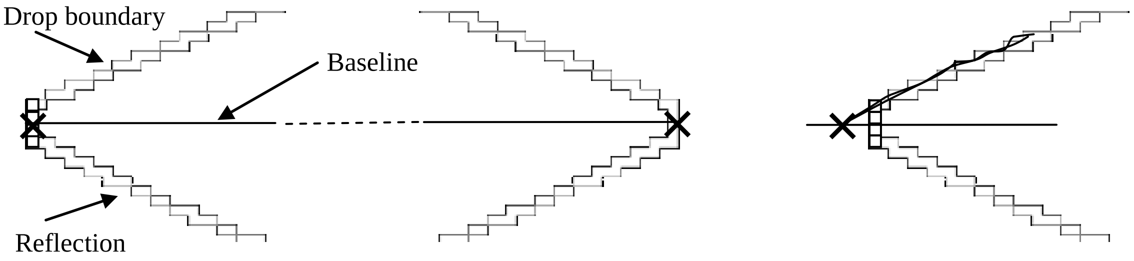

(a) (b)

Fig. 3-4 A portion of a drop boundary and its reflection near the contact point are shown (at pixel resolution). The contact point is found based on (a) median pixel calculation, and (b) extrapolating the drop boundary and its reflection. "×" is the identified contact point.

As shown in Fig. 3-4, the rough contact point may not be designated by a single pixel (in Fig. 3-4, 4 pixels are stacked near were contact point should be). Literature (*e.g.* Bateni *et al.* [26]), simply took the median of the 4 pixels in Fig. 3-4 as the location of the contact point (*e.g.* See Fig. 3-4a). The median however, can only give the vertical location of the contact point.

The *SPPF* finds the horizontal (lateral) location of the contact point as follows. A 1st order polynomial (line) is used for extrapolation. Drop boundary in pixel resolution (instead of sub-pixel resolution) is used to find the exact location of contact points. The reason is that it is preferred to work with original points which are in pixel resolution rather than calculated points which are in sub-pixel resolution. Although for fitting of the line, pixel resolution is used, but to find the vertical location of contact points, given the description of the methodology, one ends up with a sub-pixel resolution. Such improved precision, can avoid the problem noted in [34] when one deals with very high contact angles as a result moving the contact line up or down by one pixel. An important question for proper implementation of this extrapolation concept is that how many pixels need to be fitted to the drop boundary to generate the 1st order polynomial?

Finding the horizontal (lateral) location of the contact point (X) in this study is discussed with an example. For the specific example, the contact point found using the developed method is horizontally (laterally) 1.5 pixels away from the location indicated by the median pixel (see Fig. 3-5a). Depending on the number of pixels (n) used for fitting the extrapolation line, the calculated X changes (see Fig. 3-5b). The horizontal location of the contact point is considered to be the point where change of n results in the least change in X (see Fig. 3-5b). To find the least sensitive location of contact point to changing n, instead of comparing the X at n with that at $n-1$ and $n+1$, the X value is compared its value at its 10 adjacent neighboring points (5 on either side). For this example variations of X was minimum for n between 23 and 33 (this was implemented in MATLAB R2008b). So, in this example 28 pixels on the drop boundary ($n = 28$) were used to fit the extrapolation line and find the horizontal location of the contact point (X). It should be mentioned that for very large values of n, the extrapolation line cannot trace the drop boundary. This may result in predicting a non realistic X at a large n value. For this reason the range of n in *SPPF* is bounded to be smaller than 2% of the drop boundary length.

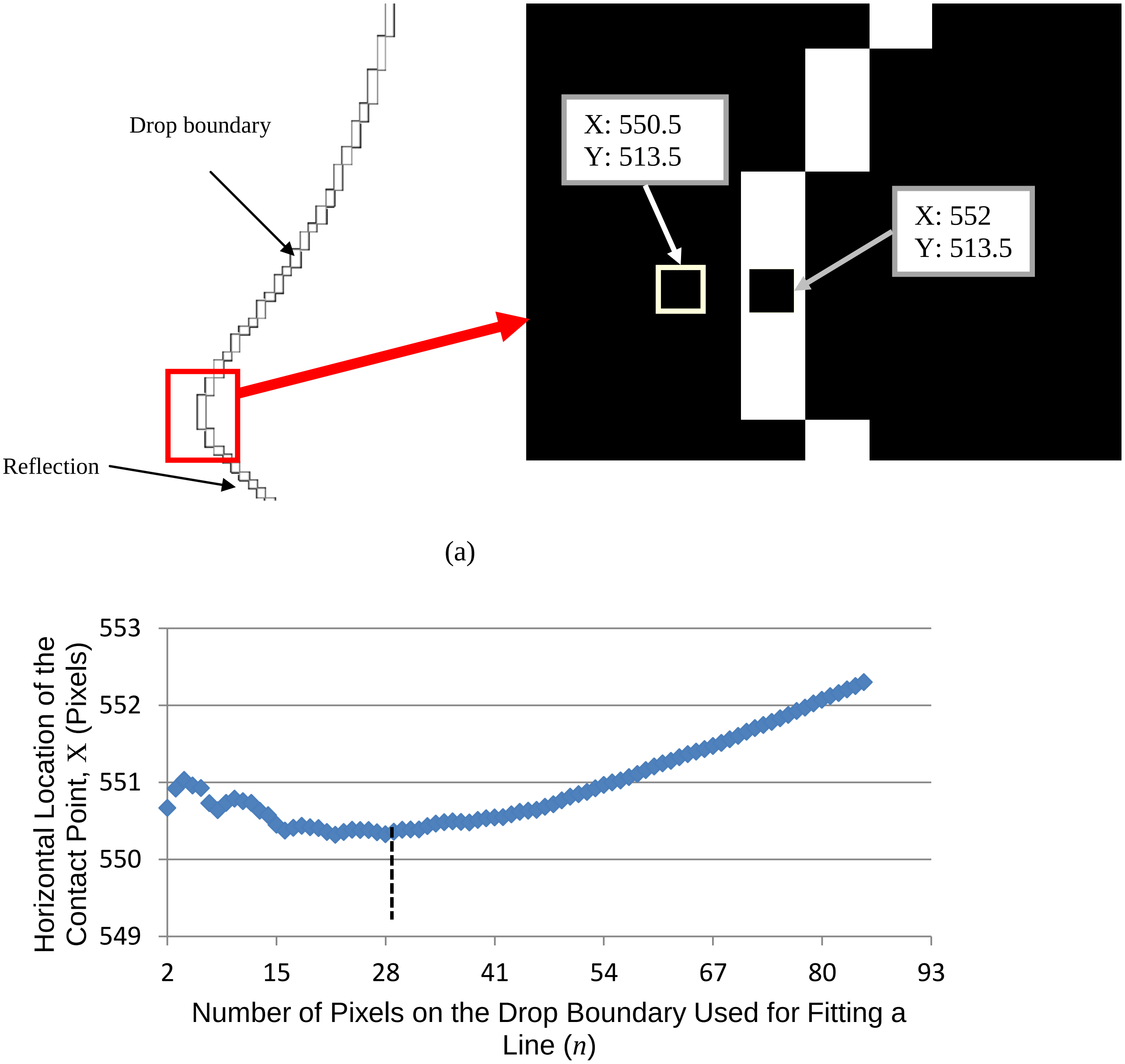

(a)

(b)

Fig. 3-5 (a) A portion of drop image near the contact point is shown. The horizontal location of the contact point with extrapolation (X=550.5) and without extrapolation (X=552) are shown. (b) Calculated horizontal location of contact point (X) versus number of pixels (***n***) used to fit the line needed for extrapolating to the contact point is shown.

3.5.1.3 Smoothing the Drop Boundary and Noise Removal

After finding the drop boundary in sub-pixel resolution, as seen in Fig. 3-6b, the drop boundary is not smooth. It was found that a first degree Savitzky-Golay FIR (finite impulse response) filter [36] is a suitable filter for smoothing the drop boundary (standard averaging filters are not proper as they do not preserve the drop boundary [38]). For removing the noise, median and Wiener filters were studied. It was observed that the median filter is better for removing the noise and preserving the drop boundary. A Gaussian noise was used to test the idea above and it was observed that a Gaussian noise with variances of up to 0.09 can be removed with median filters. It should be noted that the finding is not influenced by lighting condition.

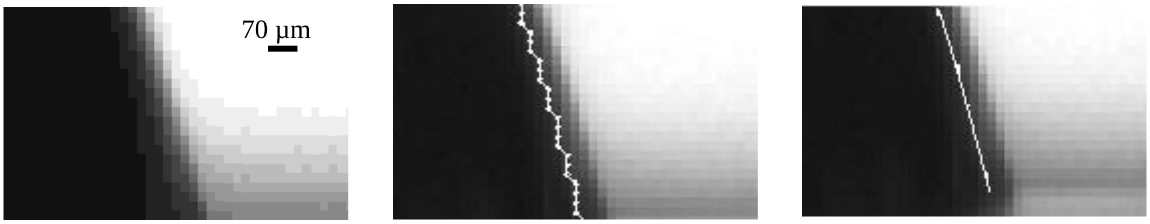

(a) (b) (c)

Fig. 3-6 (a) A section from the side view of a water drop, (b) its detected drop edge (white jagged line) in sub-pixel resolution with the method described in Fig. 3 and, (c) its smoothen edge are shown. The detected boundaries in (b) and (c) may seem to be inside the drop in these magnified images. However, as explained, the boundary was set to coincide with the location where the highest color intensity transition occurs.

3.5.1.4 Contact Angle Calculation

Contact angle is found from the slope of the fitted polynomial at the contact point. For finding the order of polynomial which best fits the drop boundary and the number of pixels required for fitting the polynomial (m), digitally generated synthetic drops with known contact angles between 10^o and 170^o were studied. Digital synthetic drops are generated by intersection of two circles (see Appendix A). For all cases, calculated contact angle versus number of pixels used for fitting 1st to 4th order polynomials were plotted. It was found that by increasing the number of pixels used for fitting the polynomial, the contact angle curve (see Fig. 3-7) forms a plateau with less than 0.1^o variation (the algorithm is similar to the one discussed in 3.5.1.2). The calculated contact angle in *SPPF* is the contact angle value at the plateau. For each individual case, *SPPF* generates a curve similar to the one in Fig. 3-7 and determines the m. Need to note that excessive increase in the number of pixel points beyond the plateau region would result in error in estimation of contact angle. The reason is that the polynomial cannot eventually trace the drop boundary shape. As plateau region will give way to deviations similar to when low number of pixels were used. The reason is that the polynomial cannot eventually trace the drop boundary shape. This was also the case for detecting the contact point in Section 2.2.

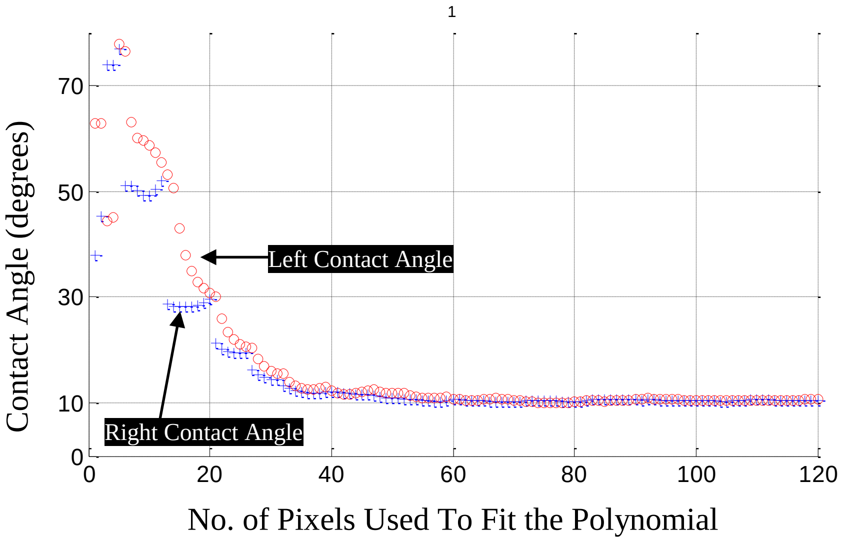

Fig. 3-7 A typical contact angle versus number of pixels (along drop profile used for fitting a 2nd order polynomial) for a synthetic drop with known contact angle of 10° is shown. The drop boundary length is 1047 pixels.

As m is case dependent, assuming a fixed number of pixels for fitting the polynomial and calculating the contact angle would not be correct. The m should be adjusted for each drop boundary length (in pixels) and volume. It should be noted that in [22, 26], they assumed a constant m for different drop volumes and observed different contact angles for same drops with different volumes. Also, Schuetter *et al.* [27], Stalder *at al.* [28] and Bateni *et al.* [26], all used fixed m values (2-10 pixels in [27], 10 and 30 pixels in [24] and 20 pixels in [26, 28]).

By studying the digitally generated synthetic drops with known contact angles (between 10° and 170°), it was observed that except for when $80^o<\theta<100^o$, absolute error of the calculated contact angle (using 2nd, 3rd and 4th order polynomials) is less than 1° degrees (see Fig. 3-8a). Since implementation of the

2^{nd} order polynomial is easier, 2^{nd} order polynomial is used for fitting the drop boundary and calculating the contact angle. It should be noted that polynomial fitting (and consequently *SPPF*) did not produce accurate results where contact angle was near 90^o (see Fig. 3-8a). The reason is that *SPPF* fits a 2^{nd} order polynomial to the drop boundary *i.e.* $y = ax^2 + bx + c$. It uses the minimization methods to find the optimum values for a, b and c. For contact angles close to 90^o, the drop boundary near the contact point has a vertical line shape *e.g.* $x = 3$. There is no combinations of a, b and c values for the above 2^{nd} order polynomial that may produce a vertical line. Since the polynomials were unable to trace the drop boundary where contact angle was close to 90^o, for the cases that the drop boundary is between 70^o and 110^o, *SPPF* rotates the drop boundary by 90^o, fits the polynomial, finds the tangent to the rotated boundary, and measures the contact angle with taking into account the rotation. With the above modification, the accuracy of the *SPPF* in the whole range of $10^o<\theta<170^o$ becomes less than 1^o (see Fig. 3-8b).

Figure 3-9a shows comparison of results from *SPPF* with *ADSA* [19], FTÅ [30] and ImageTool [32] for symmetric water drops (*e.g.* Fig. 3-1a). Since unlike a theoretical drop, for a natural drop no absolutely true contact angle value can be defined (the value measured to a degree depends on the method used), it was decided to estimate the error for the *SPPF* with respect to the average values for contact angle of one and the same drop image found using different software. Following this thinking the error is calculated and shown in Fig. 3-9a for four methods. From Fig. 3-9a it can be seen that results from FTÅ are consistently showing higher errors, which means it is skewing the average value. As such, in Fig. 3-9b results from *SPPF* with *ADSA* and ImageTool are compared. From Fig. 3-9b, it can be seen that the error, as defined, for *SPPF* was less than 3°, *i.e.* in the same order as that of ImageTool and slightly lower than error for *ADSA*. But the short processing time (less than 1 second for every single image), usability for all ranges of contact angles, applicability to both symmetric and asymmetric drops and being fully automatic are positive attributes of the *SPPF*. Furthermore, in addition to contact angle, *SPPF* finds the drop height and wetted width.

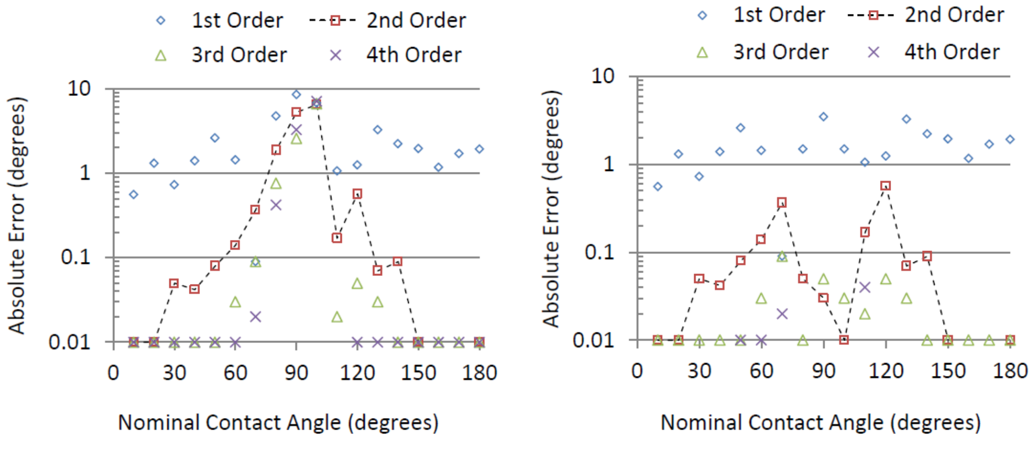

(a) (b)

Fig. 3-8 The absolute error of the calculated contact angle (using 1st, 2nd, 3rd and 4th order polynomial fittings) of synthetic drops with known contact angles is shown. (a) It is observed that polynomial fitting is inefficient in calculating the contact angle where contact angle is near 90^{o}. (b) For contact angles close to 90^{o} (70^{o}<θ<110^{o}) drop boundary is rotated by 90^{o}, and contact angle is calculated minding the rotation; as can be seen errors are much reduced compared to (a). Dashed lines are to guide eyes.

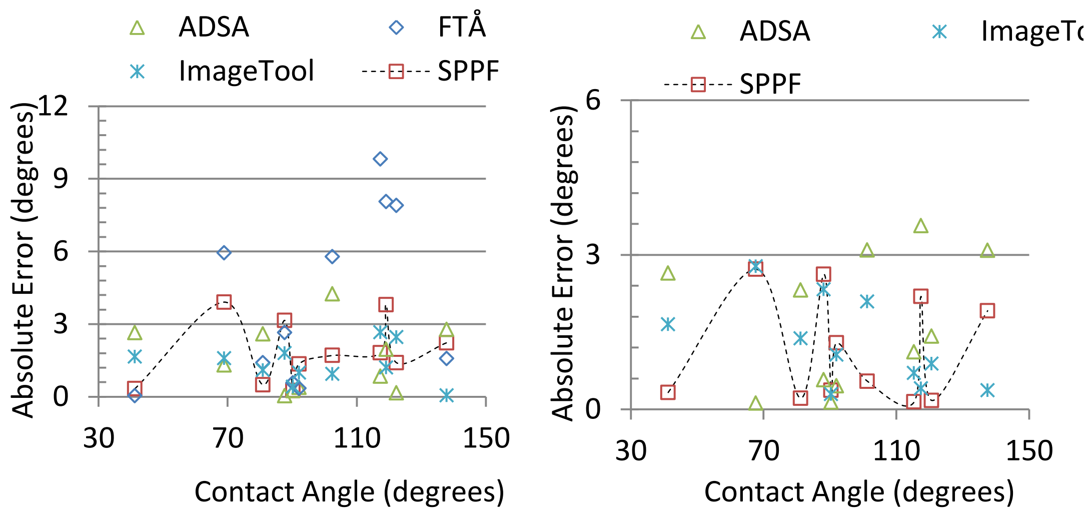

(a) (b)

Fig. 3-9 (a) *SPPF* results are compared with *ADSA*, FTÅ and ImageTool software for water drops on surfaces with different hydrophobicity. The absolute error is calculated with respect to the average results from four methods. Since FTÅ is skewing the results due to higher error, in (b) *SPPF*, *ADSA* and ImageTool are used for comparison only. Dashed lines are to guide eyes.

It should be noted that the contact angle of Ramé-Hart Instrument Co. drop calibration reference tool (images of drops with known contact angles of 30°, 60°, 90°, and 120°) was also calculated with *SPPF* and results were within 1^{o} of the expected values. To show another advantage of *SPPF* over other existing methods, following example is given: advancing and receding contact angles of a water drop placed on a superhydrophobic surface was studied. The superhydrophobic surface was fabricated by patterning a silicon substrate using photolithography method, and then coated by Teflon. Although, those drops had symmetrical shapes, FTÅ was unable to produce a proper fit to the drop boundary and measure an accurate contact angle; and *ADSA* had convergence problems which was previously reported in [39] (from [38] one understands that difficulty for ADSA may have root in numerical issues, *i.e.* “This difficulty is due to numerical truncation and accumulation of round-off errors, which are the ultimate limitation of all numerical schemes. This intrinsic limitation becomes more pronounced as drops get closer to a spherical shape, but there were no objective criteria available to define "close to spherical drops". Therefore, a quantitative criterion called shape parameter is introduced to identify the range of applicability of ADSA”). Also, ImageTool was sensitive to human error and time consuming (about 2min per single image). Advancing and receding contact angles were measured by injection and withdrawal of liquid, recording the images and analyzing the frames (~200 images). Therefore, using ImageTool would take more than 400min to analyze the whole stack of images. The *SPPF* finds the advancing and receding contact angles by analyzing all frames (see Fig. 3-10a) in less than 30 seconds with standard deviation less than 2^{o}. The *SPPF* not only finds the angles, but also detects the wetted width change; see Fig. 3-10b. Figure 3-11 shows an example of an asymmetric drop which its contact angles are found using the *SPPF*.

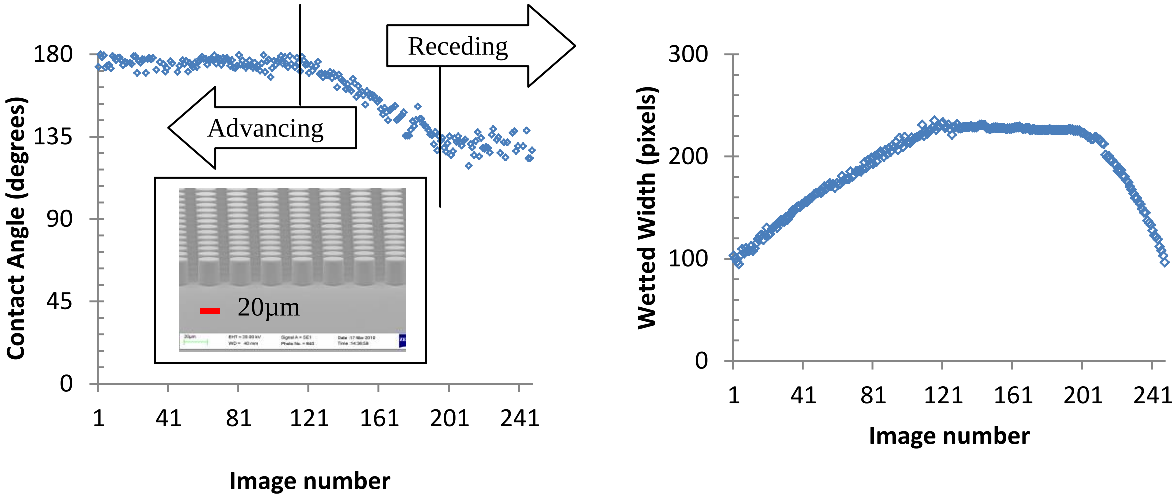

(a) (b)

Fig. 3-10 (a) Contact angles and (b) wetted width of a water drop (on patterned silicon and coated with Teflon; shown in the insert), by increasing and decreasing the volume, are shown.

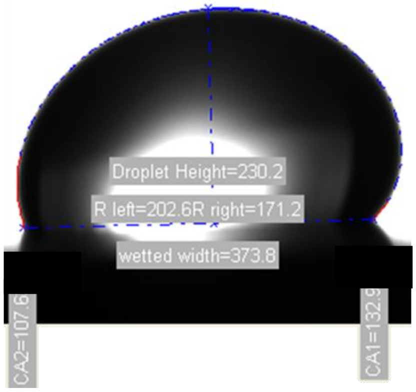

Fig. 3-11 The output of *SPPF* for an asymmetric drop is shown. Left and right contact points and contact angles are found using the *SPPF*. Drop dimensions are in pixels and can be found by calculating the physical dimension of pixels, through calibration. The *SPPF* program is available to all in [40] with proper referring to this paper.

It should be mentioned that *SPPF* detects the drop boundary using a single value for threshold. This will result in the following shortcoming: if a part of the drop boundary in an image is heavily shadowed (*e.g*. Fig. 3-12a), *SPPF* cannot detect the drop boundary. This is also mentioned in [34] as a drawback of drop methods for measuring the contact angle. In the next paragraph it will be shown that why SPPF cannot find the drop boundary of the drop in Fig. 3-12a, then a proper drop image will be shown. In the last part of this paper, it will be shown that the shadowing issue is not really a drawback and as will be shown in Fig. 3-13 this can be avoided by proper capturing of drop image.

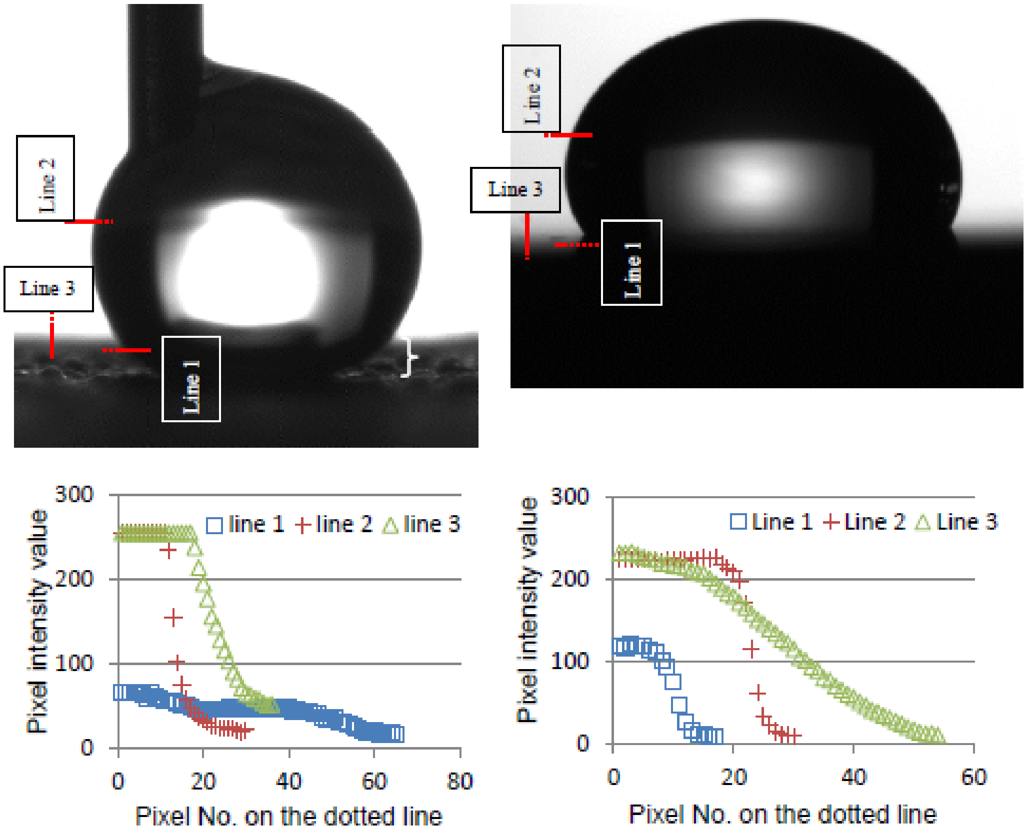

Fig. 3-12 (a) A case where *SPPF* is unable to measure the contact angle is shown. It should be mentioned that as the contact point is not even distinguishable with eyes, the contact angle values measured from images such as this are not reliable. The pixel intensity curve along the line 1 does not have a sigmoid shape. As such, *SPPF* does not detect the drop boundary in the region shown with the white curly bracket. (b) Proper angle of camera and light intensity makes the drop boundary and its reflection detectable *i.e.* the pixel intensity curves along lines 1 and 2 have sigmoid shape.

The pixel intensity plot across the line 1 in Fig. 3-12a does not have a sigmoid shape (drop boundary in *SPPF* is found as the saddle point of the sigmoid shaped curve). As such, *SPPF* is unable to find the drop boundary in the region shown with the curly bracket in Fig. 3-12a. Also, in Fig. 3-12a pixel intensity across the solid surface (line 3) changes as a sigmoid, and *SPPF* incorrectly takes the solid surface as the drop boundary. Figure 3-12b is an example of a properly captured image usable for *SPPF* is shown. As shown, pixel intensity curve along Lines 1 and 2 have a sigmoid; therefore *SPPF* detects the drop boundary and its reflection. Also, the pixel intensity curve along the line 3 does not have a sigmoid shape and solid surface edge will not be detected as the drop boundary. Regarding Figs. 3-12 and 3-13 it should be mentioned that above remarks may not be noticeable very well in the printed version and it is recommended to look at the online version of paper.

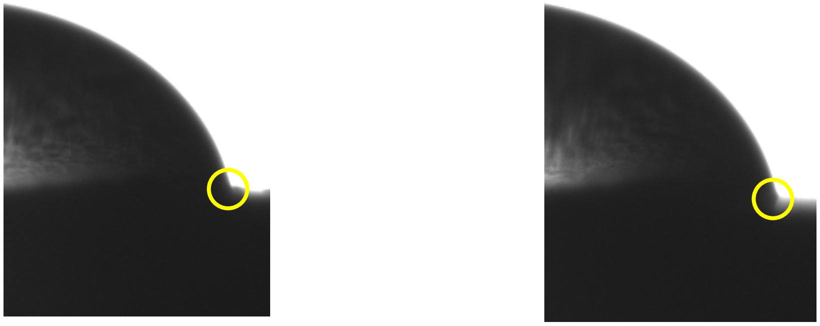

(a) (b)

Fig. 3-13 A region of a drop near the contact point is shown. a) camera is horizontal, b) camera is 5° tilted (back to front) which makes the reflection observable. Reflection is needed for detecting the contact point. Above remarks may not be noticeable very well in the printed version and it is recommended to look at the online version of paper.

Images such as the ones in Figs. 3-12a and 3-13a are not proper for measuring the contact angles. The reason is that the exact location of contact points, even with eyes, is not detectable. It was found that the above mentioned picture quality problem in terms of shadow can be avoided during the capturing of images by tilting the camera and/or changing the light intensity (*e.g.* in Fig. 3-13 camera is 5° tilted, back to front). As such, this is not really a limitation.

3.6 Conclusions

A method (*SPPF*) is developed to measure the contact angle of both symmetric and asymmetric drops for a wide range of contact angles. *SPPF* does not require any liquid property value and is suitable for automated computer implementations. *SPPF* fits a 2nd order polynomial to the drop boundary (near the contact points) and calculates the contact angle as the slope of the fitted curve where it intersects the baseline. Drop boundary and contact points are found in sub-pixel resolutions. Since polynomials were unable to produce accurate results where contact angle was close to 90^o, for contact angles between 70^o and 110^o, *SPPF* rotates the drop boundary and calculates the contact angle with consideration for the rotation. With the above modification, the *SPPF* had a small error of less than 1^o in calculating the contact angle of synthetic drops over a wide range of contact angles between 10^o and 170^o. For natural symmetric drops, the error for *SPPF* was determined as a relative value, *i.e.* the error was calculated with respect to the mean value of the contact angle values found using *ADSA* and FTÅ and ImageTool, to be less than 3^o. The error for *SPPF* when comparing to calibration slides or synthetic drops was less than 1^o. This error was in the order of /or slightly lower than the error of all other methods. It should also be mentioned that short processing time (less than 1 second for every single image), usability for all ranges of contact angles, applicability to both symmetric and asymmetric drops and being fully automatic are other advantages of the *SPPF*.

Acknowledgements

The authors would like to thank NSERC (Natural Sciences and Engineering Research Council of Canada), CRC (Canada Research Chair program) for funding this project. The authors would also like to extend their gratitude to Denise Thornton for her guidance and comments.

Appendix A-Synthetic Drops by Intersection of two Circles

Synthetic drops are generated as part of circles. Figure A1 shows the detail of generating the synthetic drop in this study. Approximation of drop shapes with circles is also mentioned in [41, 42].

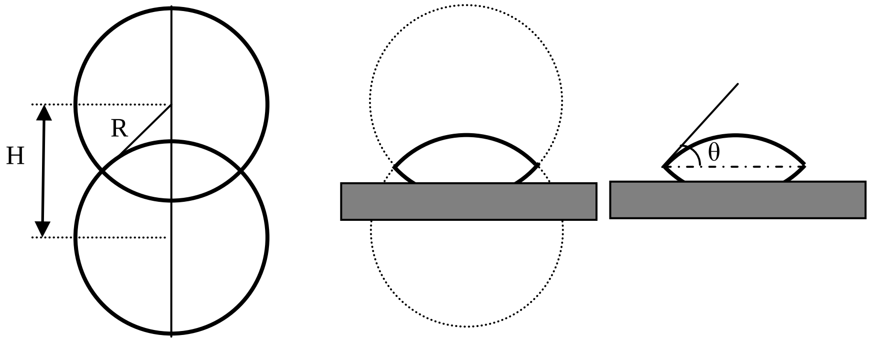

Fig. A1 The figure shows how a synthetic sessile drop can be generated by intersecting two circles.

From Fig. A1, a synthetic drop with known contact angle can be generated by setting *H* and *R* values (see Eq. A1).

$$\theta = A\cos(\frac{H}{2R}) \tag{A1}$$

3.7 References

[1] McHale, G., Rowan, S. M., Newton, M. I., 1998, "Evaporation and the Wetting of a Low-Energy Solid Surface," Journal of Physical Chemistry B, **102**(11) pp. 1964-1967.

[2] Antonim, C., Carmona, F. J., Pierce, E., 2009, "General Methodology for Evaluating the Adhesion Force of Drops and Bubbles on Solid Surfaces," Langmuir, **25**(11) pp. 6143-6154.

[3] Kugel, G., Klettke, T., Goldberg, J. A., 2007, "Investigation of a New Approach to Measuring Contact Angles for Hydrophilic Impression Materials," Journal of Prosthodontics, **16**(2) pp. 84-92.

[4] Dogan Buzoglu, H., Calt, S., and Gümüsderelioglu, M., 2007, "Evaluation of the Surface Free Energy on Root Canal Dentine Walls Treated with Chelating Agents and NaOCl," International Endodontic Journal, **40**(1) pp. 18-24.

[5] Kontakiotis, E. G., Tzanetakis, G. N., and Loizides, A. L., 2007, "A Comparative Study of Contact Angles of Four Different Root Canal Sealers," Journal of Endodontics, **33**(3) pp. 299-302.

[6] Daffonchio, D., Thaveesri, J., and Verstraete, W., 1995, "Contact Angle Measurement and Cell Hydrophobicity of Granular Sludge from Upflow Anaerobic Sludge Bed Reactors," Applied and Environmental Microbiology, **61**(10) pp. 3676-3680.

[7] Salaün, F., Devaux, E., Bourbigot, S., 2009, "Application of Contact Angle Measurement to the Manufacture of Textiles Containing Microcapsules," Textile Research Journal, **79**(13) pp. 1202-1212.

[8] Neumann, A.W., 1996, "Applied Surface Thermodynamics," CRC Press, New York, USA, .

[9] Oguz, H. N., and Sadhal, S. S., 1988, "EFFECTS OF SOLUBLE AND INSOLUBLE SURFACTANTS ON THE MOTION OF DROPS." Journal of Fluid Mechanics, **194**pp. 563-579.

[10] Marmur, A., 1997, "Line Tension and the Intrinsic Contact Angle in Solid-Liquid-Fluid Systems," Journal of Colloid and Interface Science, **186**(2) pp. 462-466.

[11] Amirfazli, A., Keshavarz, A., Zhang, L., 2003, "Determination of Line Tension for Systems Near Wetting," Journal of Colloid and Interface Science, **265**(1) pp. 152-160.

[12] Rusanov, A. I., 1999, "Classification of Line Tension," Colloids and Surfaces A: Physicochemical and Engineering Aspects, **156**(1-3) pp. 315-322.

[13] Baxter, S., 1950, "Wetting and Contact-Angle Hysteresis," Nature, **165**(4188) pp. 198.

[14] Bateni, A., Laughton, S., Tavana, H., 2005, "Effect of Electric Fields on Contact Angle and Surface Tension of Drops," Journal of Colloid and Interface Science, **283**(1) pp. 215-222.

[15] Wenzel, R. N., 1949, "Surface Roughness and Contact Angle," Journal of Physical & Colloid Chemistry, **53**(9) pp. 1466-1467.

[16] Cassie, A. B. D., 1948, "Contact Angles," Discussions of the Faraday Society, **3**pp. 11-16.

[17] Rotenberg, Y., Boruvka, L., and Neumann, A. W., 1983, "Determination of Surface Tension and Contact Angle from the Shapes of Axisymmetric Fluid Interfaces," Journal of Colloid and Interface Science, **93**(1) pp. 169-183.

[18] Del Río, O. I., and Neumann, A. W., 1997, "Axisymmetric Drop Shape Analysis: Computational Methods for the Measurement of Interfacial Properties from the Shape and Dimensions of Pendant and Sessile Drops," Journal of Colloid and Interface Science, **196**(2) pp. 136-147.

[19] Kalantarian, A., David, R., and Neumann, A. W., 2009, "Methodology for High Accuracy Contact Angle Measurement," Langmuir, **25**(24) pp. 14146-14154.

[20] Bateni, A., Susnar, S. S., Amirfazli, A., 2004, "Development of a New Methodology to Study Drop Shape and Surface Tension in Electric Fields," Langmuir, **20**(18) pp. 7589-7597.

[21] Hoorfar, M., and W. Neumann, A., 2006, "Recent Progress in Axisymmetric Drop Shape Analysis (ADSA)," Advances in Colloid and Interface Science, **121**(1-3) pp. 25-49.

[22] Li, L., Kang, W., and Ye, D., 2007, "A contact angle measurement method for the droplets in EWOD-based chips," Proceedings of the 2nd IEEE International Conference on Nano/Micro Engineered and Molecular Systems, IEEE NEMS 2007, Anonymous pp. 1071-1075.

[23] Goclawski, J., and Urbaniak-Domagala, W., 2007, "The method of solid-liquid contact angle measurement using the images of sessile drops with shadows on substratum," Proceeding of the 3rd International Conference of Young Scientists "Perspective Technologies and Methods in MEMS Design", MEMSTECH 2007, Anonymous pp. 135-140.

[24] Bortolotti, M., Brugnara, M., Volpe, C. D., 2009, "Numerical Models for the Evaluation of the Contact Angle from Axisymmetric Drop Profiles: A Statistical Comparison," Journal of Colloid and Interface Science, **336**(1) pp. 285-297.

[25] Iliev, S., and Pesheva, N., 2006, "Nonaxisymmetric Drop Shape Analysis and its Application for Determination of the Local Contact Angles," Journal of Colloid and Interface Science, **301**(2) pp. 677-684.

[26] Bateni, A., Susnar, S. S., Amirfazli, A., 2003, "A High-Accuracy Polynomial Fitting Approach to Determine Contact Angles," Colloids and Surfaces A: Physicochemical and Engineering Aspects, **219**(1-3) pp. 215-231.

[27] Schuetter, S., Shedd, T., Doxtator, K., 2006, "Measurements of the Dynamic Contact Angle for Conditions Relevant to Immersion Lithography," Journal of Microlithography, Microfabrication and Microsystems, **5**(2) .

[28] Stalder, A. F., Kulik, G., Sage, D., 2006, "A Snake-Based Approach to Accurate Determination of both Contact Points and Contact Angles," Colloids and Surfaces A: Physicochemical and Engineering Aspects, **286**(1-3) pp. 92-103.

[29] Xu, C., and Prince, J. L., 1998, "Snakes, Shapes, and Gradient Vector Flow," IEEE Transactions on Image Processing, **7**(3) pp. 359-369.

[30] Anonymous "Contact Angle Measurements using the Drop Shape Method," .

[31] Woodward R. P., "Dispensing Method and Apparatus for Dispensing very SmallQuantities of Fluid." (US 6579497) .

[32] Anonymous "Image Tool Version 3.0," .

[33] Otsu, N., 1979, "THRESHOLD SELECTION METHOD FROM GRAY-LEVEL HISTOGRAMS." IEEE Trans Syst Man Cybern, **SMC-9**(1) pp. 62-66.

[34] Zimmermann, J., Seeger, S., and Reifler, F. A., 2009, "Water Shedding Angle: A New Technique to Evaluate the Water-Repellent Properties of Superhydrophobic Surfaces," Textile Research Journal, **79**(17) pp. 1565-1570.

[35] Chini, S. F., "Various Methods of Interpolation," .

[36] Savitzky, A., and Golay, M. J. E., 1964, "Smoothing and Differentiation of Data by Simplified Least Squares Procedures," Analytical Chemistry, **36**(8) pp. 1627-1639.

[37] Atae-Allah, C., Cabrerizo-Vílchez, M., Gómez-Lopera, J. F., 2001, "Measurement of Surface Tension and Contact Angle using Entropic Edge Detection," Measurement Science and Technology, **12**(3) pp. 288-298.

[38] MathWorks, "Savitzky-Golay FIR Smoothing Filter," .

[39] Hoorfar, M., 2006, "Development of a Third Generation of Axisymmetric Drop Shape Analysis (ADSA)," .

[40] Chini, S. F., "Drop Contact Angle Measurement Software SPPF Ver. 4.3," (Oct/2012) .

[41] ElSherbini, A. I., and Jacobi, A. M., 2004, "Liquid Drops on Vertical and Inclined Surfaces: I. an Experimental Study of Drop Geometry," Journal of Colloid and Interface Science, **273**(2) pp. 556-565.

[42] ElSherbini, A. I., and Jacobi, A. M., 2004, "Liquid Drops on Vertical and Inclined Surfaces: II. A Method for Approximating Drop Shapes," Journal of Colloid and Interface Science, **273**(2) pp. 566-575.

Chapter 4 - Understanding the Evaporation of Spherical Drops in Quiescent Environment

4.1 Introduction

Studying the evaporation of fully isolated and suspended drops is important in understanding the evaporation of drops from surfaces fundamentally. Evaporation of drops from solid surfaces has a broad application in cleaning industries, ink jet printing [1], PEM (Proton Exchange Membrane) fuel cells [2-4], surface patterning [5], etc. For most of the mentioned applications, drops are evaporated from solid surfaces. In this study, a model is developed to explain the evaporation of suspended micro-drops (drops not touching a surface) at room temperature, normal atmospheric condition and quiescent environment (*i.e.* no external airflow). The suspended drops rather than sessile or pendant drops are studied to minimize the factors affecting the evaporation *e.g.* thermal conductivity of the substrate [6, 7], or contact angle hysteresis due to the substrate [8], and find the fundamentals of evaporation. For micro-liter drops, as drop radius is larger than $0.01\mu m$, Kelvin's effect (higher vapor pressure on the drop surface than on a planar liquid surface) is not important [9, 10]. Ivchenko [11-14] has studied the evaporation of drops with radius in the order of $0.01\mu m$ (or Kn, Knudsen number, is almost equal to 1). In [15] it was shown that for some liquids (*e.g.* water drops) surface cooling is as low as $3-4^{o}C$; and for some liquids (*e.g.* heptane) surface cooling is as high as $20^{o}C$. In this study, surface cooling effect is assumed to be small (<4^{o}C), to consider the system as iso-thermal. As such, for the cases that surface cooling is not small, the developed model is not accurate.

This is further discussed in Section 3.2. As shown in [16-18], the evaporation rate of drops at normal atmospheric condition is considered not to be limited by the transfer of molecules across the liquid-vapor interface (phase change) but by the transfer from the drop surface to the surrounding (vapor transport). The mass flux of vapor leaving the drop is:

$$\mathbf{J}_{\boldsymbol{v}}^{\diamond} = \rho_{v}^{\diamond}\boldsymbol{u}_{\boldsymbol{v}}^{\diamond} \tag{4-1}$$

where $\mathbf{J}_{\boldsymbol{v}}^{\diamond}$ is the molar flux of vapor $\left({}^{mol}/{}_{m^2.s}\right)$, $\rho_{v}^{\diamond}$ is the molar density of vapor $\left({}^{mol}/{}_{m^3}\right)$ and $u_{v}^{\diamond}$ is the velocity of vapor (m/s). As will be shown, expressing mass flow rate and density in molar units rather than kilograms, facilitate the formulation of the problem. Integration of $\mathbf{J}_{\boldsymbol{v}}^{\diamond}$ along the drop surface gives the total molar flux of vapor leaving the drop surface, or evaporation rate. From the molar balance of drop liquid and vapor, one has the following:

$$\mathbf{J}_{\boldsymbol{v}}^{\diamond} = \frac{\rho_{L}^{\diamond}}{S}\frac{\partial \mathrm{V}}{\partial t} \tag{4-2}$$

where V and S are drop volume (m^3) and surface area (m^2), respectively; $\rho_{L}^{\diamond}$ is the liquid molar density $\left({}^{mol}/{}_{m^3}\right)$ and t is the time (s).

Assuming the vapor-air mixture is an ideal gas [19], the air-vapor mixture molar density ($\rho^{\diamond} = \frac{P}{RT}$, $R = 8.314\,J/K.mol$, P is pressure in Pa and T is temperature in Kelvin) is constant throughout the gas phase. It should be noted that constant density throughout the gas phase is not true if density is expressed in kg/m^3. The air-vapor mixture molar density is also equal to:

$$\rho^\diamond = \rho_a^\diamond + \rho_v^\diamond \tag{4-3}$$

where $\rho_a^\diamond$ is the molar density of air. The molar averaged velocity of vapor-air mixture ($\boldsymbol{u}^\diamond$) is:

$$\boldsymbol{u}^\diamond = \frac{\rho_a^\diamond}{\rho^\diamond}\boldsymbol{u}_{\boldsymbol{a}}^\diamond + \frac{\rho_v^\diamond}{\rho^\diamond}\boldsymbol{u}_{\boldsymbol{v}}^\diamond \tag{4-4}$$

where $u_a^\diamond$ is the air velocity. The vapor flux (*i.e.* $\mathbf{J}_{\boldsymbol{v}}^\diamond$) can be decomposed into convection (advection, 1st term in the right hand side, RHS, of Eq. 4-5) and diffusion (2nd term in the RHS of Eq. 4-5). Using Fick's first law of binary diffusion [20, 21], which was originally developed for movement of salt in liquids, and Eq. 5-1, one has [22]:

$$\mathbf{J}_{\boldsymbol{v}}^\diamond = \rho_v^\diamond \boldsymbol{u}^\diamond - \rho^\diamond D \nabla w_v^\diamond \tag{4-5}$$

where D is the binary diffusion constant of vapor into air (${}^{m^2}/{}_{s}$), w_v is $\rho_v^\diamond/\rho^\diamond$,

and $\nabla w_v^\diamond$ is the vapor concentration gradient (VCG). The question is how to find the $\mathbf{J}_{\boldsymbol{v}}^\diamond$. According to Eq. 4-5, for finding the vapor flux ($\mathbf{J}_{\boldsymbol{v}}^\diamond$), $\boldsymbol{u}^\diamond$ and $\nabla w_v^\diamond$ are needed. It should be noted that some of the studies in literature have used lubrication assumption along with Navier-Stokes (without calculating the $\nabla w_v^\diamond$ and $\boldsymbol{u}^\diamond$) to find $\mathbf{J}_{\boldsymbol{v}}^\diamond$, *e.g.* in [5]. However, those studies are limited to very thin sessile drops, and evaporation rate is found only near the contact line. These models cannot be used for suspended spherical drops. The next section of this paper discusses the results in the literature for finding $\boldsymbol{u}^{\diamond}$, $\nabla w_v^{\diamond}$ and consequently $\mathbf{J}_v^{\diamond}$.

4.2 Maxwell's Approach

As will be shown, assuming the evaporation process is (i) quasi-steady, and (ii) non-convective, a model is developed in literature for finding the diffusion [18] and vapor flux leaving the drop surface. These assumptions are adopted from Maxwell's study on evaporation from a wet-bulb, but their validity for micro-liter drops is not fully appreciated (see below).

Regarding the steady-state assumption, the original experiment of Maxwell, took 2-3 days and the VCG became relatively steady after approximately 45min. However, for a micro-liter drop where the lifetime is in the order of minutes, assuming a quasi-steady process may not be a good assumption. This is further investigated by considering a heat analogy problem i.e. a semi-infinite slab which initially is at a uniform temperature. The slab surface from one side is suddenly taken to a higher temperature (similar to start of evaporation right after forming the drop). The analogous problem is solved in [23]; using the analogy method and substituting the relevant values for evaporation (temperature and heat flux are analogous to $\mathrm{w_v}$ and VCG, respectively). It can be shown that the VCG is time dependent, especially in the first 10 minutes, which is in the order of the lifetime of micro-liter drops.

Regarding the non-convective assumption, Guena et al. [24, 25], from observing an identical evaporation behavior for sessile and hanging drops of the same type concluded convection is small during the evaporation of micro-liter drops. However, the “buoyancy” is a better term for the observation mentioned in [24, 25], and not the “convection”. Buoyancy is ascending or descending the vapor due to the weight of vapor relative to air, and has opposite effects on sessile and pendant drops [26]. As understood from evaporation in Stefan tube with gravity [27], the buoyancy-driven convective flux has a small contribution in total convection. Other contributors to convection are mentioned in [27].

Also, there are not enough experiments in literature to enable one to either approve or reject the validity of Maxwell’s assumptions for micro-liter drops. Most of the experiments are for sessile drops and as mentioned in [6][6], existence of the surface adds more parameters to the problem and one cannot easily check the validity of Maxwell assumptions. Regarding the suspended drops, in literature, most use electromagnetic energy to levitate the drops e.g. [28], or falling drops at terminal velocity [29]. As shown in [30] the electromagnetic energy adds extra parameters to the problem and charged drops evaporate slower than uncharged drops. Also, drops falling at terminal velocity in air are exposed to a large forced convection (*e.g.* [31]). As such, electromagnetically levitated or free falling drops cannot be used to verify the Maxwell’s assumptions. To the knowledge of authors, the experiment in [15] is the only experimental result in the literature for evaporation of fully spherical drops in quiescence environment and room temperature in absence of external effects.

Maxwell originally derived a relationship for evaporation from a wet-bulb thermometer using a heat analogy problem [18], and its mass analogy is explained in this section. For finding the $\nabla \mathrm{w}_{\mathrm{v}}^{\diamond}$, he applied the continuity of mass for vapor in a shell of small thickness (see Fig. 4-1) located at some arbitrary distance from a wet-bulb (or drop) surface [32]:

$$\frac{\partial \rho_v^{\diamond}}{\partial t} + \nabla.\left(\rho_v^{\diamond}\boldsymbol{u}^{\diamond} - \rho^{\diamond}\, D\nabla w_v^{\diamond}\right) = 0 \tag{4-6}$$

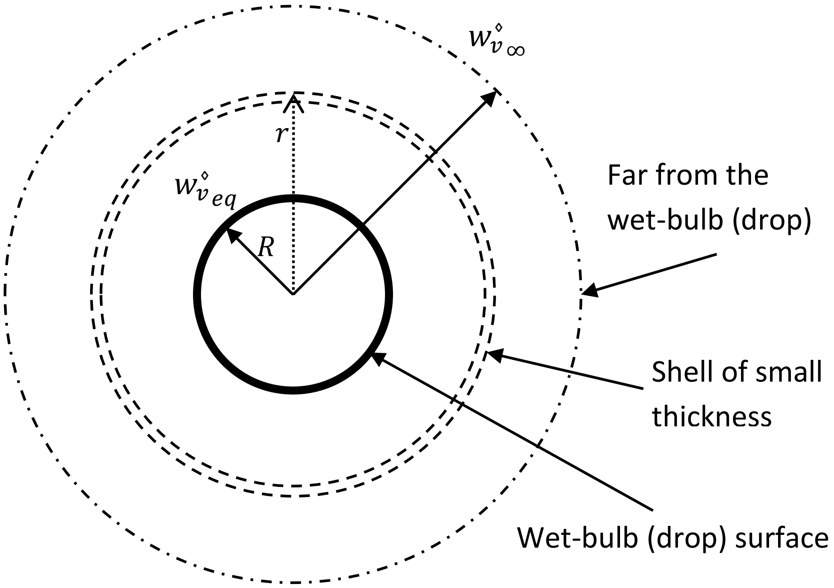

Fig. 4-1 Schematic of a wet-bulb (drop) surrounded by air is shown. The solid thick line denotes the wet-bulb (drop) free surface. $w_{v\,eq}^{\diamond}$ and $w_{v\,\infty}^{\diamond}$ are vapor concentrations at the wet-bulb (drop) surface and far from it.

From above equation and knowing that $\rho_v^\diamond = \rho^\diamond w_v^\diamond$, one has:

$$\frac{\partial(\rho^\diamond w_v^\diamond)}{\partial t} + \nabla.(\rho_v^\diamond \boldsymbol{u}^\diamond) - \nabla.(\rho^\diamond D \nabla w_v^\diamond) = 0 \tag{4-7}$$

Using the continuity equation for vapor-air mixture, *i.e.* $\frac{\partial \rho^\diamond}{\partial t} + \nabla.(\rho^\diamond \boldsymbol{u}^\diamond) = 0$, Eq. 4-7 simplifies to:

$$\rho^\diamond \frac{\partial w_v^\diamond}{\partial t} + \rho^\diamond \boldsymbol{u}^\diamond.\nabla(w_v^\diamond) - \nabla.(\rho^\diamond D \nabla w_v^\diamond) = 0 \tag{4-8}$$

Equation 7 holds regardless of constancy of $\rho^\diamond$. As discussed, in the previous section $\rho^\diamond$ is constant in space. Maxwell [18] assumed convection is negligible (*i.e.* $\boldsymbol{u}^\diamond = 0$) and process is steady state (*i.e.* $\frac{\partial w_v^\diamond}{\partial t} = 0$). The assumptions seemed valid for Maxwell's original experiment which was evaporation from a wet-bulb. With above mentioned assumptions, Eq. 4-8 reduces to:

$$\nabla.(\nabla w_v^\diamond) = 0 \tag{4-9}$$

For evaporation from a wet-bulb, due to the symmetry in angular directions, $\nabla w_v^\diamond$ reduces to a 1-D case (*i.e.* in r direction), see Fig. 4-1. For such a case, using Eq. 4-9, $\nabla w_v^\diamond$ becomes radially outward, and on the drop surface its magnitude, $\left\|\nabla w_{v\ at\ R-Maxwell}^\diamond\right\|$, will be [18]:

$$\left\|\nabla w_{v\ at\ R-Maxwell}^\diamond\right\| = -\frac{\left(w_{v_{eq}}^\diamond - w_{v_\infty}^\diamond\right)}{R} \tag{4-10}$$

where R is the radius of the wet-bulb (or suspended drop), $w_{v_{eq}}^\diamond$ and $w_{v_\infty}^\diamond$ are $\rho_v^\diamond/\rho^\diamond$ in a thin shell surrounding the liquid and the far field, respectively. It can be assumed that $w_{v_{eq}}^\diamond$ is equal to the density ratio of vapor to air-vapor mixture in a vapor saturated air [33]. This is valid when $R > 10\mu m$ [12]. For $R < 10\mu m$, the influence of the curvature of the wet-bulb (or suspended drop) and surface tension of the liquid on the saturated vapor density is not negligible and $w^{\diamond}_{v_{eq}}$ would not be equal to the ratio of vapor to air-vapor mixture in a vapor saturated air [10]. Using Eq. 4-10 along with Eq. 4-5, one may find the molar vapor flux. Sreznevsky [34] adapted Maxwell's assumptions to the evaporation of drops and used Eq. 4-10 to find the VCG of drops by replacing the wet-bulb radius with the drop radius. Ever since, Maxwell's model is widely used for finding the VCG and evaporation flux of drops. Also, most of the evaporation models developed for sessile drops use the Maxwell's model [35-49] or are based on Maxwell's model with some modifications *e.g.* taking into account the variation of the VCG across the drop surface [50-58]; or modifications due to the thermal conductivity of the substrate [6].

In [59], using Eqs. 4-2, 4-5, 4-10 and knowing that for a suspended spherical drop, V and S can be given in terms of R, the radius of a suspended spherical drop during evaporation was calculated as:

$$R_{\text{Maxwell}} = \sqrt{-2D\frac{\rho^{\diamond}}{\rho_L^{\diamond}}\left(w^{\diamond}_{v_{eq}} - w^{\diamond}_{v_{\infty}}\right)t + R_0^2} \tag{4-11}$$

where R_{Maxwell} is the drop radius (using Maxwell's model) at time t, and R_0 is the initial drop radius.

In [15] the linear trend of $m^{2/3}$ versus time during the evaporation of water, n-butyl alcohol and octane drops suspended from polypropylene fibers (drops were hung from the crossover of polypropylene fibers) was explained by Eq. 4-11 (note that $m = \frac{4}{3}\pi\rho_L^{\diamond}MR^3$, where M is the molar mass, kg/mol). Regarding Eq. 4-11, it should be noted that the evaporation time (drop lifetime) can be found by setting $R_{\text{Maxwell}} = 0$ and solving for t. An examination of the experiments in [15] shows that for some of the cases, the values of the slopes of $m^{2/3}$ in time is not completely in agreement with Eq. 4-11 (*e.g.* see Fig. 2). In [15] the discrepancy between experiments and Eq. 4-11 was explained by the surface cooling phenomena. Surface cooling is simply a temperature reduction at the surface of liquid due to the heat loss as a result of evaporation. However, due to the following reason surface cooling cannot explain the discrepancy seen in Fig. 4-2. Surface cooling generally slows the evaporation process. Therefore, the slope of $m^{2/3}$ versus time should be lower in presence of surface cooling. However, it is observed that except for water, the experimental slope of $m^{2/3}$ versus time is higher than the one found using Maxwell's model (see Fig. 4-2). Furthermore, other studies showed that the surface cooling for such drops is small, *e.g.* [60].

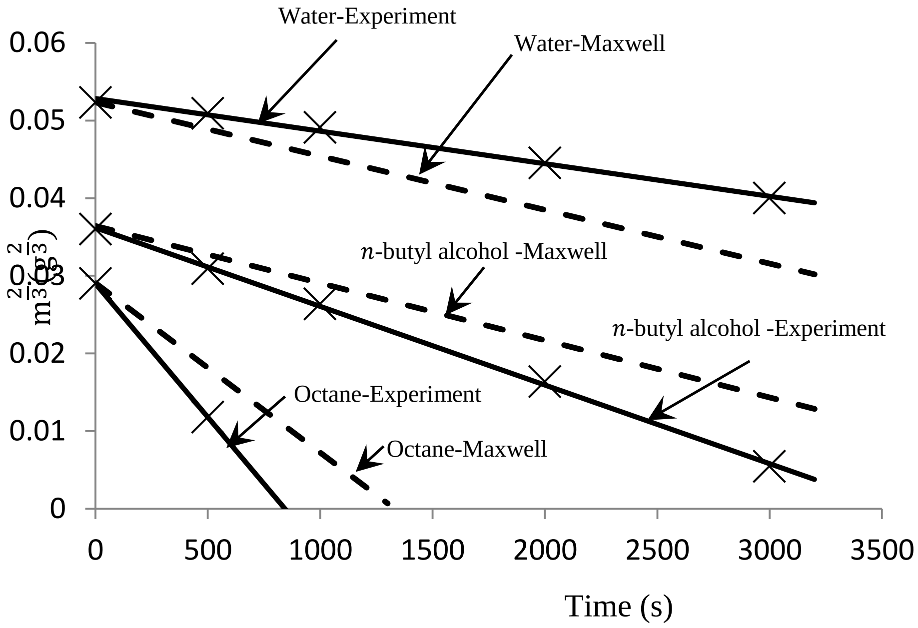

Fig. 4-2 Change of $m^{2/3}$ in time for suspended spherical n-butyl alcohol, octane and water drops is shown. Experimental values (symbols) are taken from [15], and dashed lines are drawn using Eq. 4-11 (note that $m = \frac{4}{3}\pi\rho_L^{\circ}MR^3$). Solid lines are to guide eyes.

In the next part of this paper, first the steady-state assumption is relaxed and a transient non-convective (TNC) model is developed. The TNC is not suggested to be used for evaporation of micro-liter drops as it still ignores the convection term. The goal of developing the TNC was to show if evaporation of micro-liter drops is a steady-state process or not. Then, a transient and convective (TC) model is developed which relaxes both of the Maxwell assumptions. The TC model developed is suggested to be used for studying the evaporation of drops, especially for volatile liquids.

4.3 Transient, Non-Convective (TNC) Model

The transient and non-convective (TNC) model developed in this section, relaxes only one of the Maxwell assumptions, *i.e.* steady-state assumption. The only purpose of developing this model is to show the transient effect is not small.

By ignoring the convection (*i.e.* $\boldsymbol{u}^{\diamond} = 0$), the vapor flux is solely impelled by the diffusion, and $\nabla w_v^{\diamond}$ is the only unknown to find for calculating the vapor flux (see Eq. 4-5). For finding the $\nabla w_v^{\diamond}$, Eq. 4-8 is used. Due to the symmetry in angular directions for a fully spherical (suspended) drop and inserting zero for convection term, Eq. 8 simplifies to:

$$\rho^{\diamond} \frac{\partial w_v^{\diamond}}{\partial t} + \frac{1}{r^2} \frac{\partial}{\partial r} (-r^2 \rho^{\diamond} D \frac{\partial w_v^{\diamond}}{\partial r}) = 0 \qquad (4\text{-}12)$$

Boundary and initial conditions for Eq. 4-12 are:

$$w_v^{\diamond}(R, t) = w_{v_{eq}}^{\diamond}, \qquad t > 0, \qquad \frac{r}{R} \gg 1 \qquad (4\text{-}13,1)$$

$$w_v^{\diamond}(\infty, t) = w_{v_\infty}^{\diamond}, \qquad t > 0, \qquad r = R \qquad (4\text{-}13,2)$$

$$w_v^{\diamond}(r, 0) = w_{v_\infty}^{\diamond}, \qquad t = 0, \qquad r > R \qquad (4\text{-}13,3)$$

For solving the partial differential equation in Eq. 4-12, the similarity transformation method is used where the similarity variable (η) is:

$$\eta = \frac{r^2}{4D(t_{lifetime} - t)} \qquad (4\text{-}14)$$

where $t_{lifetime}$ is the evaporation time. This similarity variable is an indication of the rate of change of r^2 (or drop area) in time. Using the similarity variable, Eq. 4-12 simplifies to an ordinary differential equation:

$$\frac{d^2 w_v^{\diamond}}{d\eta^2} + \left(1 + \frac{1}{\eta}\right)\frac{dw_v^{\diamond}}{d\eta} = 0 \tag{4-15}$$

and the solution is:

$$w_v^{\diamond} = A \int_{\eta}^{\infty} \frac{e^{-\eta}}{\eta} d\eta + B \tag{4-16}$$

where A and B are constants and shall be found using the initial and boundary conditions in Eq. 4-13. Using the second boundary condition and the initial condition (*i.e.* at $\eta \rightarrow \infty$, $w_v^{\diamond} = w_{v\infty}^{\diamond}$), one has:

$$B = w_{v\infty}^{\diamond} \tag{4-17}$$

At the drop interface, $w_{v\ at\ R}^{\diamond} = w_{v_{eq}}^{\diamond}$. As such, one has:

$$A = \frac{w_{v_{eq}}^{\diamond} - w_{v\infty}^{\diamond}}{\int_{\eta_i}^{\infty} \frac{e^{-\eta}}{\eta} d\eta} \tag{4-18}$$

where η_i is found by replacing r by R in Eq. 4-14 as:

$$\eta_i = \frac{R^2}{4D(t_{lifetime} - t)} \tag{4-19}$$

As such, similar to η, η_i is an indication of the evaporation rate and the larger the η_i, the faster the evaporation rate is. It should be noted that for micro-liter drops with lifetime in the order of 10 minutes, η_i is in the order of 10^{-5} (using Eq. 4-19, the $\eta_i$values for the cases studied in [15] are found and presented in Table 4-

1). Regarding Eq. 4-18, note that the left hand side (LHS) is a constant and the right hand side (RHS) is a function of η_i. As such, η_i should stay constant over time, and using Eq. 4-19 one has: $R^2 \propto (t_{lifetime} - t)$. Therefore, the transient, non-convective (TNC) evaporation model predicts that the change of R^2 (or $m^{\frac{2}{3}}$) in time is linear. The linear trend is similarly observed in models based on Maxwell's assumptions (see Eq. 4-11).

Table 4-1 The relevant parameters [61] and experimental η_i values for four different liquids studied in [15] are shown at pressure of 740 to 746 mmHg and the temperature of 20^{o}C. η_i is found using Eq. 4-19 and using lifetimes from the experiments.

	$D\ (\frac{m^2}{s})$	$w_{v_{eq}}$	$\rho_L\ (\frac{kg}{m^3})$	$R_0(mm)$	$t_{lifetime}\ (s)$	η_i
Octane	5.90×10^{-5}	0.0537	702	1.19	780	7.70×10^{-5}
Nitro methane	1.01×10^{-5}	0.0743	1137	1.24	960	3.98×10^{-5}
n-butyl alcohol	8.00×10^{-5}	0.0140	810	1.27	3300	1.53×10^{-5}
Water (62% RH)	2.04×10^{-5}	0.0146	998	1.42	9300	2.66×10^{-5}

Using Eqs. 4-16 to 4-18 and finding the gradient in the spherical coordinates (only in r-direction, as due to the symmetry other components are zero) one has:

$$\|\nabla w^{\diamond}_{v\,at\,R-TNC}\| = -\frac{\left(w^{\diamond}_{v\,eq} - w^{\diamond}_{v\,\infty}\right)}{R} f(\eta_i) \tag{4-20}$$

where $f(\eta_i)$ is:

$$f(\eta_i) = \frac{2e^{-\eta_i} + 2\eta_i \int_{\eta_i}^{\infty} (\frac{1+\eta}{\eta^2}) e^{-\eta}\, d\eta}{\int_{\eta_i}^{\infty} \frac{e^{-\eta}}{\eta}\, d\eta} \tag{4-21}$$

The value of $f(\eta_i)$ versus η_i is numerically found using Matlab ® 2011 and shown in Fig. 4-3. It was also found that $\frac{4\,e^{-\eta_i}}{-Ei(-\eta_i)}$ is a good approximation for Eq. 4-21 where Ei is an exponential integral [62]. Using Eqs. 4-2, 4-5 and 4-20 and knowing that for a suspended spherical drop, V and S can be given in terms of R, one has:

$$RdR = -2D \frac{v}{\rho^{\diamond}_L} \left(w^{\diamond}_{v\,eq} - w^{\diamond}_{v\,\infty}\right) f(\eta_i) dt \tag{4-22}$$

Solving the above differential equation results in:

$$R_{TNC} = \sqrt{\left\{-2D \frac{\rho^{\diamond}}{\rho^{\diamond}_L} \left(w^{\diamond}_{v\,eq} - w^{\diamond}_{v\,\infty}\right) t\right\} f(\eta_i) + R_0^2} \tag{4-23}$$

By comparing Eqs. 4-11 and 4-23 one can see that the only difference between TNC and Maxwell model is $f(\eta_i)$. As shown in Table 4-1, for the experiments in [15], η_i is between 10^{-4} and 10^{-5} (η_i is found using Eq. 4-19 and using lifetimes from the experiments). Considering Fig. 4-3, for η_i between 10^{-4} and 10^{-5}, $f(\eta_i)$ is on average 0.4. As such, by including the transient term, evaporation rate decreases by approximately 60% (slope of R^2 versus t is an indication of evaporation rate, see Eq. 4-2 and knowing that for spherical drops $V = \frac{4}{3}\pi R^3$).

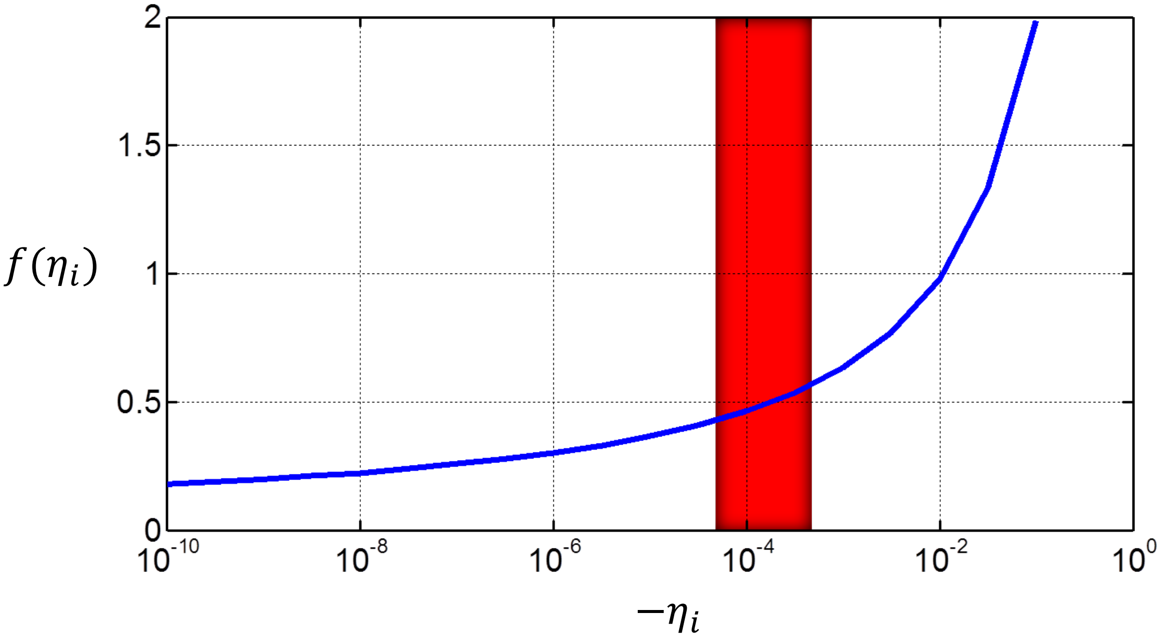

Fig. 4-3 The value of $f(\eta_i)$ versus η_i is shown (see Eqs. 4-19 to 4-23). For η_i between 10^{-4} and 10^{-5} (shaded area), $f(\eta_i)$ is on average 0.4.

Here, a methodology for finding η_i without performing experiments is explained. The η_i found from this method was in the same order of magnitude of values found from experiments. At $t = t_{lifetime}$, the drop radius vanishes (*i.e.* $R_{TNC} = 0$). As such, using Eq. 4-23, knowing that $f(\eta_i) \approx \frac{4\,e^{-\eta_i}}{-Ei(-\eta_i)}$, and using Eq. 4-19 at time zero, (*i.e.* ${R_0}^2 = 4Dt_{lifetime}\eta_i$), one has:

$$-Ei(-\eta_i)\eta_i e^{\eta_i} = 2\frac{\rho^\diamond}{\rho_L^\diamond}\left(w_{v\,eq}^\diamond - w_{v\,\infty}^\diamond\right) \qquad (4\text{-}24)$$

The η_i value is found by solving the above equation (numerically or graphically). In Fig. 4-4, Eq. 4-24 is solved graphically for the octane drop in [15]. Table 4-1 shows the η_i values found experimentally using the experimental results of [15]. The difference between the calculated η_i value and the one found from experiment is that the TNC model does not include the convective term. This can be another indication of the importance of convection in evaporation of drops.

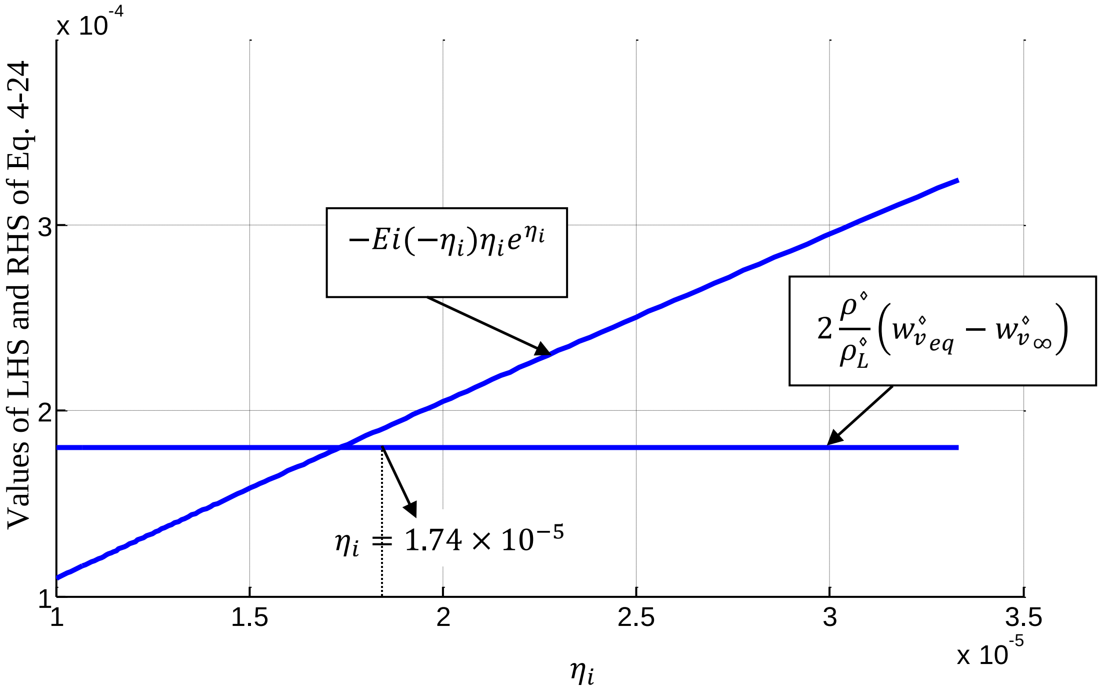

Fig. 4-4 Equation 4-24 is solved graphically for the octane drop in [15]. The intersection of the RHS and the LHS of Eq. 4-24 is the solution. Using the η_i value one may find the evaporation time (drop lifetime).

The results of this part showed the process of evaporation of micro-liter drops is not steady-state. However, the TNC is not recommended for micro-liter drops, as it ignores the effect of convection. As will be shown, for evaporation of micro-liter drops, convection is not small.

4.4 Transient, Convective (TC) Model

In the previous section it was shown that the transient effect is not negligible. In this section, the non-convective assumption is also relaxed and a transient, convective (TC) model is developed. As seen in Eq. 4-5, for the convection term, the value of $u^{\diamond}$ is needed. Stefan using the impermeability of drop surface to air derived a relation for $\boldsymbol{u}^{\diamond}$ [63-66]. However, as will be explained, Stefan's approach is limited to steady-state problems; also he assumed that the liquid interface does not move (Stefan's approach is discussed in the Appendix); none of these assumptions would be valid for evaporation of micro-liter drops. The other approach is jump mass balance. As will be shown the second approach does not have the limitations of Stefan's approach.

4.4.1 Jump Mass Balance Approach

Using the continuity equation for air-vapor mixture in molar form *i.e.* $\frac{\partial \rho^{\diamond}}{\partial t} + \nabla . (\rho^{\diamond} \boldsymbol{u}^{\diamond}(s,t)) = 0$, at constant $\rho^{\diamond}$, one has $\nabla . \boldsymbol{u}^{\diamond}(s,t) = 0$, where $u^{\diamond}(s,t)$ is the molar averaged velocity of the air-vapor mixture as a function of space (s) and time. The mass continuity equation for the air-vapor mixture in the Spherical coordinates is:

$$\frac{1}{r^2}\frac{\partial (r^2 \boldsymbol{u}^{\diamond})}{\partial r} + \frac{1}{r\sin\theta}\frac{\partial (\boldsymbol{u}^{\diamond}{}_{\boldsymbol{\theta}} \sin\theta)}{\partial \theta} + \frac{1}{r\sin\theta}\frac{\partial (\boldsymbol{u}^{\diamond}{}_{\emptyset})}{\partial \emptyset} = 0 \qquad (4\text{-}25)$$

where $\boldsymbol{u}^{\diamond}{}_{\boldsymbol{\theta}}$ and $\boldsymbol{u}^{\diamond}{}_{\emptyset}$ are molar averaged velocity of the air-vapor mixture in polar (θ) and azimuthal ($\emptyset$) directions in the Spherical coordinates. Due to the symmetry in polar and azimuthal directions, for a suspended spherical drop, Eq. 4-25 simplifies to:

$$\frac{1}{r^2}\frac{\partial(r^2\boldsymbol{u}^\diamond)}{\partial r}=0 \tag{4-26}$$

Therefore, $\boldsymbol{u}^\diamond$ is given as:

$$\|\boldsymbol{u}^\diamond\|=\frac{\xi(t)}{r^2} \tag{4-27}$$

where $\xi(t)$ is an arbitrary function of t and should be determined. The air-vapor mixture jump mass balance at the drop interface is [67]:

$$-\rho_L^\diamond\boldsymbol{u_S}=\rho^\diamond(\boldsymbol{u}^\diamond-\boldsymbol{u_S}) \tag{4-28}$$

where $\boldsymbol{u_S}$ is the drop interface velocity (which is equal to $\frac{dR}{dt}$). Solving the Eq. 4-28 for u_S gives:

$$\|\boldsymbol{u_S}\|=-\frac{\rho^\diamond}{\rho_L^\diamond-\rho^\diamond}u^\diamond \tag{4-29}$$

The vapor jump mass balance at the drop interface is [68]:

$$-\rho_L^\diamond\boldsymbol{u_S}=\rho_v^\diamond(\boldsymbol{u_v^\diamond}-\boldsymbol{u_S}) \tag{4-30}$$

By inserting the value for $\boldsymbol{u_S}$ from Eq. 4-29 into Eq. 4-30, and solving for $\rho_v^\diamond\boldsymbol{u_v^\diamond}$, one has the following relationship for molar flux of vapor:

$$\rho_v^\diamond\boldsymbol{u_v^\diamond}=\rho^\diamond\frac{\rho_L^\diamond-\rho_v^\diamond}{\rho_L^\diamond-\rho^\diamond}\boldsymbol{u}^\diamond \tag{4-31}$$

Using Eqs. 4-1, 4-5 and 4-31, and knowing that $w_v^\diamond$ is $\rho_v^\diamond/\rho^\diamond$, one has:

$$D\nabla w_v^{\diamond} - w_v^{\diamond}\boldsymbol{u}^{\diamond} + \frac{\rho_L^{\diamond} - \rho_v^{\diamond}}{\rho_L^{\diamond} - \rho^{\diamond}}\boldsymbol{u}^{\diamond} = 0 \tag{4-32}$$

Using Eqs. 4-27, and 4-32, after simplification and taking into account of symmetry in polar and azimuthal directions, it can be shown that:

$$\frac{D(\rho_L^{\diamond} - \rho^{\diamond})}{\rho_L^{\diamond}\xi(t)} r^2 \frac{\partial w_v^{\diamond}}{\partial r} - w_v^{\diamond} + 1 = 0 \tag{4-33}$$

Above equation is a first order linear ordinary differential equation and its solution is:

$$w_v^{\diamond}(r,t) = c_1(t) e^{-\frac{\rho_L^{\diamond}\xi(t)}{D(\rho_L^{\diamond} - \rho^{\diamond})r}} + 1 \tag{4-34}$$

where $c_1(t)$ is the integration constant. Using the boundary and initial conditions mentioned in Eq. 4-13, one has:

$$c_1(t) = w_{v\,\infty}^{\diamond} - 1, \qquad t > 0 \tag{4-35,1}$$

$$\xi(t) = ln\left(\frac{w_{v\,\infty}^{\diamond} - 1}{w_{v\,eq}^{\diamond} - 1}\right) \frac{D(\rho_L^{\diamond} - \rho^{\diamond})}{\rho_L^{\diamond}} R, \qquad t > 0 \tag{4-35,2}$$

$$\xi(0) = ln\left(\frac{c_1(0)}{w_{v\,\infty}^{\diamond} - 1}\right) \frac{D(\rho_L^{\diamond} - \rho^{\diamond})}{\rho_L^{\diamond}} r, \qquad t = 0, r \geq R_0 \tag{4-35,3}$$

Using Eqs. 4-34, 4-35,1 and 4-35,2, $w_v^{\diamond}(r,t)$ is calculated as:

$$w_v^{\diamond}(r,t) = (w_{v\,\infty}^{\diamond} - 1)\left(\frac{w_{v\,\infty}^{\diamond} - 1}{w_{v\,eq}^{\diamond} - 1}\right)^{-\frac{R}{r}} + 1 \tag{4-36}$$

Inserting Eq. 4-35,2 into Eq. 4-27 results in:

$$\|\boldsymbol{u}^{\diamond}\| = ln\left(\frac{w_{v\,\infty}^{\diamond} - 1}{w_{v\,eq}^{\diamond} - 1}\right) \frac{D(\rho_L^{\diamond} - \rho^{\diamond})}{\rho_L^{\diamond}} \frac{R}{r^2} \tag{4-37}$$

Using Eq. 4-37 and definition of Péclet number ($Pe = \frac{u^{\diamond 2} t}{D}$), one may find that convection is not negligible. The Pe value is approximately equal to $\frac{D\left(w^{\diamond}_{v_{eq}} - w^{\diamond}_{v\infty}\right)^{2} t}{R^2}$. Knowing that for micro-liter water drops, $D \sim 10^{-5}$, $w^{\diamond}_{v_{eq}} \sim 0.01$, $R \sim 10^{-3}$ and $t \sim 10^{3}$, one may find that $Pe \approx 1$ which means that convection and diffusion have the same order of magnitude for micro-liter water drops.

Using Eqs. 4-5, 4-36 and 4-37 at $r = R$ and knowing that $\rho^{\diamond}_{v}$ is equal to $w^{\diamond}_{v_{eq}} \rho^{\diamond}$ one has:

$$\mathbf{J}^{\diamond}_{v} = \rho^{\diamond}_{v} \boldsymbol{u}^{\diamond} - \rho^{\diamond} D \nabla w^{\diamond}_{v} = \frac{\rho^{\diamond} D}{R} ln\left(\frac{w^{\diamond}_{v\infty} - 1}{w^{\diamond}_{v_{eq}} - 1}\right)\left\{-w^{\diamond}_{v_{eq}} \frac{\rho^{\diamond}}{\rho^{\diamond}_{L}} + 1\right\} \tag{4-38}$$

Using Eq. 4-38, for a spherical drop ($V = \frac{4}{3}\pi R^3$ and $S = 4\pi R^2$), one has:

$$\frac{\partial R}{\partial t} \rho^{\diamond}_{L} = \frac{\rho^{\diamond} D}{R} ln\left(\frac{w^{\diamond}_{v\infty} - 1}{w^{\diamond}_{v_{eq}} - 1}\right)\left\{1 - \frac{\rho^{\diamond}}{\rho^{\diamond}_{L}} w^{\diamond}_{v_{eq}}\right\} \tag{4-39}$$

Solving the above linear first order differential equation gives:

$$R^2 = -2 \frac{\rho^{\diamond}}{\rho^{\diamond}_{L}} D \left\{\left(1 - \frac{\rho^{\diamond}}{\rho^{\diamond}_{L}} w^{\diamond}_{v_{eq}}\right) ln\left(\frac{w^{\diamond}_{v\infty} - 1}{w^{\diamond}_{v_{eq}} - 1}\right)\right\} t + {R_0}^{2} \tag{4-40}$$

The difference between Eqs. 4-11 and 4-40 is in a curly bracket. As $\frac{\rho^{\diamond}}{\rho^{\diamond}_{L}} w^{\diamond}_{v_{eq}} \ll 1$, and for small $w^{\diamond}_{v_{eq}}$ values $\left(1 - \frac{\rho^{\diamond}}{\rho^{\diamond}_{L}} w^{\diamond}_{v_{eq}}\right) ln\left(\frac{w^{\diamond}_{v\infty} - 1}{w^{\diamond}_{v_{eq}} - 1}\right) \approx \left(w^{\diamond}_{v_{eq}} - w^{\diamond}_{v\infty}\right)$, the results from Maxwell's model are close to the results from the TC model (see Fig. 4-5).

The small difference between Maxwell and TC models does not mean that evaporation of micro-liter drops is steady and non-convective. As shown in the previous section, considering the transient term decreased the evaporation rate (slope of R^2 versus time) by approximately 60%. Including the convection, brings the evaporation rate (slope of R^2 versus time) close to the value predicted by Maxwell's model. In other words, for small $w_{v\,eq}^{\diamond}$ values, the effect of convection and transient cancel each other. This is crucial to know as some studies in literature for developing a better model may relax the steady-state or non-convective assumption one at a time, *e.g.* [69]. For the cases that $w_{v\,eq}^{\diamond}$ is not small (*e.g.* diethyl ether, $w_{v\,eq}^{\diamond} = 0.5$), the difference between Maxwell and TC models is not negligible and one cannot use the Maxwell's model.

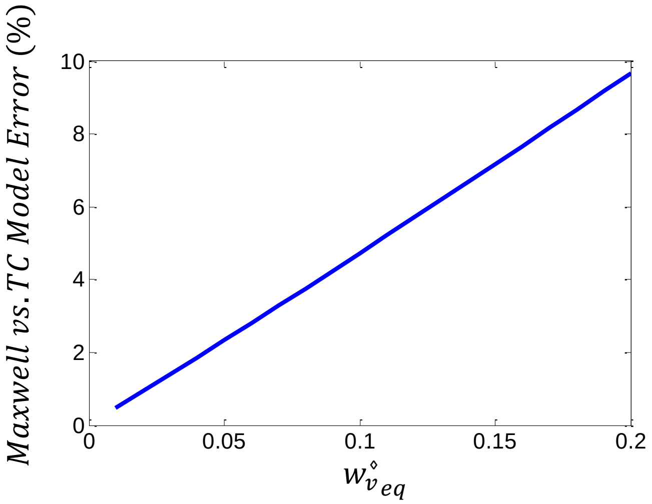

Fig. 4-5 The error in using the Maxwell model relative to the transient-convective (TC) model developed in this study versus $w_{v\,eq}^{\diamond}$ is shown.

4.5 Experiments

To verify the developed TC model (Eq. 4-40), the slope of R^2 versus time for micro-liter suspended water, methanol and ethanol drops have been tested. Drops were suspended from a knot created on a copper wire. The knot size was at least 10 times smaller than the initial diameter of the drop and the top of drop was attached to the bottom of the knot. The wire was tied to a stand and put on a micro-balance (Sartorius TE214S). The micro-balance was connected to a PC and programmed to record the weight of the drop every 5 seconds. Drops were put by means of a micro pipette with the volume of approximately $4\mu l$. The whole system was enclosed in a chamber to minimize the outside air flow. The minimum distance of drop from each wall was at least $15cm$ to make sure that diffusion is not limited by walls. Each experiment was repeated 12 times and between each set, wire was completely cleaned using acetone followed by methanol and rinsed by DI-water then dried completely. The chamber was kept open and purged between each experiment to make sure that initial concentration of vapor in the chamber is consistent. The wet and dry bulb temperatures were $T_{db} = 21.7^o$ and $T_{wb} = 13.8^o$, therefore, $RH = 0.4$. The atmospheric pressure was $99.058\ kPa$, so $\rho^\diamond = 38.4\frac{mol}{m^3}$. Drop surface temperature was found using an IR camera (FLIR A320). Other relevant parameters are listed in Table 4-2.

Table 4-2 Liquid and vapor properties needed (from [70] and [71]).

Liquid	$D(\frac{m^2}{s})$	$P_{sat}(kPa)$	$M(\frac{g}{mol})$	$\rho_L(\frac{kg}{m^3})$	$\rho_L^{\circ}(\frac{mol}{m^3})$	$\rho_v^{\circ}(\frac{mol}{m^3})$	$w_{v_{eq}}^{\circ}$	$w_{v_{\infty}}^{\circ}$
DI-Water	2.45×10^{-5}	2.671	18.015	997.78	55.37×10^{3}	1.078	0.0281	0.0112
Methanol	1.4×10^{-5}	14.748	32.042	786.5	24.55×10^{3}	5.890	0.1534	0
Ethanol	1.1×10^{-5}	6.629	46.071	785.1	17.04×10^{3}	2.678	0.0697	0

4.6 Results and Discussion

The slope of R^2 versus t was found for DI-water, methanol and ethanol micro-liter drops (*e.g.* see Fig. 4-6) and compared with Eqs. 4-11 and 4-40; the results are shown in Table 4-3. The results at which drop radius is small ($R < 10\mu m$) are not used (the reason is discussed in Section 4.1).

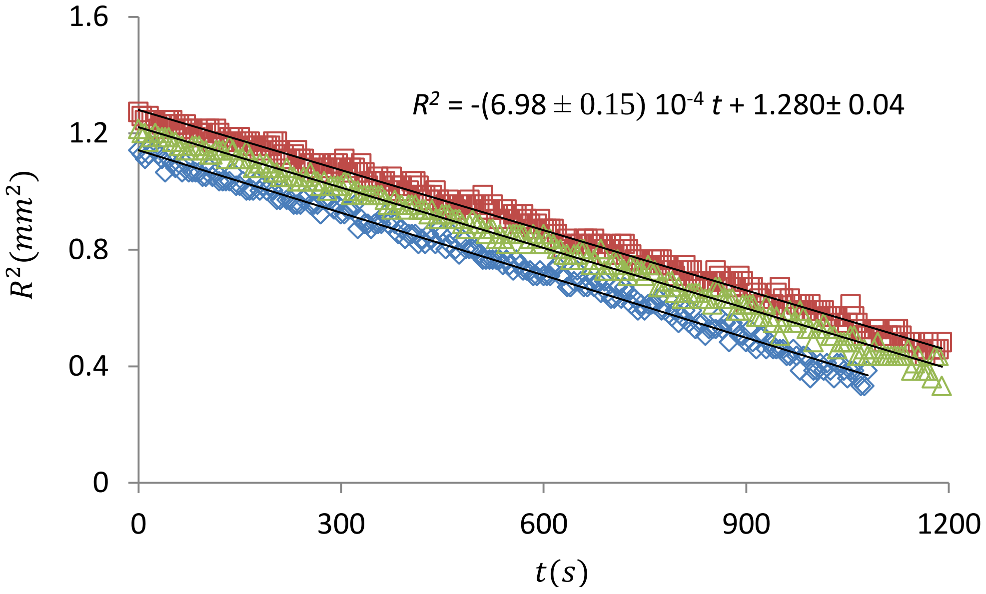

Fig. 4-6 The R^2 versus t during the evaporation for three suspended spherical water drops is shown. It is shown that the slope of R^2 versus t is unchanged. The slope of R^2 versus t is important as it is an indication of evaporation rate, also enables one to predict the evaporation time.

As shown in Table 4-3 the TC and Maxwell models both follow the experiments very well. For the range of micro-liter drop variables, transient and convective effects balance each other, and Maxwell and TC models provide relatively equal values. However, the transient and convective effects do not necessarily cancel each other and in general the TC model should be used. The inconsistency between experiments and models observed for methanol (see Table 3) is related to the surface cooling as evaporation rate is decreased (as mentioned in Section 4.0 surface cooling slows down the evaporation rate). It was found that the temperature change for methanol is more than 10^o. It should be noted that for water and ethanol drops surface cooling was less than 3^o.

Table 4-3 Slope of R^2 (mm^2) versus t (s) found using the TC (Eq. 40) and Maxwell (Eq. 11) model is compared with the experimental results.

Liquid	TC	Maxwell	Experiments
Water	-5.85×10^{-4}	-5.73×10^{-4}	$-(6.98 \pm 0.15) \times 10^{-4}$
Methanol	-7.29×10^{-3}	-6.72×10^{-3}	$-(3.90 \pm 0.17) \times 10^{-3}$
Ethanol	-3.58×10^{-3}	-3.46×10^{-3}	$-(4.05 \pm 0.25) \times 10^{-3}$

4.7 Conclusions

This study can provide a better insight into evaporation of micro-liter drops in room condition through newly developed model. Maxwell's assumptions (*i.e.* non-convective and quasi-steady) are the foundation of most of the drop evaporation studies. In this paper, these two assumptions were relaxed. First the steady-state assumption was relaxed and a transient non-convective (TNC) model was developed. It was found that the transient effect is not negligible. Then the convection velocity was found using the jump mass balance concept. As Péclet number suggests, convection is not negligible in evaporation of drops. By relaxation of the non-convective assumption, a transient and convective (TC) model was developed. By comparing the TC model with Maxwell's, it was found that in the range of parameters for micro-liter methanol, ethanol and water drops, the effect of transient term cancels the effect of convection. This is important as (i) some studies, for increasing the accuracy, relax either one of the steady-state or non-convective assumptions which may result in inaccurate results; (ii) for the range of variables where transient and convective effect do not cancel each other, the TC model rather than the Maxwell's model should be used.

Acknowledgement

Authors would like to thank Natural Sciences and Engineering Research Council of Canada (NSERC) and CRC (Canada Research Chair) program for their financial support.

Appendix

Diffusion of vapor into air, from a different perspective, can be considered as diffusion of air into vapor. Similar to Eq. 4-5, for mass flux of air one has the following:

$$\mathbf{J}_{\boldsymbol{a}}^{\diamond} = \rho_a^{\diamond}\boldsymbol{u}^{\diamond} - \rho^{\diamond} D \nabla w_a^{\diamond} \tag{A-1}$$

where $\mathrm{J}_a^{\diamond}$ is the mass flux of air (since it is a binary diffusion, diffusion constant of vapor to air equals to that of air to vapor). Stefan diffusion is usually used when in a mixture one component has a zero flux (*e.g.* evaporation of a puddle of water lying on the ground into air). Since liquid interface is impermeable to air [66], on the drop surface, the net mass flow rate of air is zero (*i.e.* $\mathbf{J}_{\boldsymbol{a}}^{\diamond} = 0$) or the air convection is balanced by diffusion. At steady-state this flux is zero everywhere in a column on top of the interface (Stefan's assumption [63-65]). Assuming a 1-D mass transport, there should be no mass flow rate of air everywhere on top of the liquid surface or throughout a gas column on top of the drop surface (*i.e.* $\mathbf{J}_{\boldsymbol{a}}^{\diamond} = 0$). From that and solving for $u^{\diamond}$ in Eq. A-1, one has:

$$\boldsymbol{u}^{\diamond} = \frac{\rho^{\diamond}}{\rho_a^{\diamond}} D \nabla w_a^{\diamond} \tag{A-2}$$

Using Eq. 4-3, one may find $\nabla w_a^{\diamond} = -\nabla w_v^{\diamond}$. Using Eqs. 4-5, and A-2 the vapor flux is found as [66]:

$$\mathbf{J}_{\boldsymbol{v}}^{\diamond} = -\frac{\rho^{\diamond}}{1 - w_v^{\diamond}} D \nabla w_v^{\diamond} \tag{A-3}$$

The values for $w_v^{\diamond}$, $\nabla w_v^{\diamond}$ and consequently $\mathbf{J}_{\boldsymbol{v}}^{\diamond}$ may be found using Eq. 4-8 (not completely solved here); where $u^{\diamond}$ is found using Eq. A-2 and knowing that in steady-state condition one has: $\frac{\partial w_v^\diamond}{\partial t} = 0$ as follows. The solution for Eq. 4-8 in this case is:

$$w_v^\diamond = \frac{\rho_a^\diamond}{\rho^\diamond} log(\frac{\rho^\diamond}{r\rho_a^\diamond} + c_2) + c_3 \qquad \text{(A-4)}$$

where c_2 and c_3 are integration constants and should be found using initial and boundary conditions stated in Eq. 4-13. Equation A-4 is not solved as this approach assumes the evaporation is steady (which is shown otherwise in Section 4.4).

4.8 References

[1] Thomas, J. E., and McKnight, J. K., 1984, "Ink Evaporation Prevention Means for Ink Jet Print Head," (4412233) .

[2] Lan, H., Friedrich, M., Armaly, B. F., 2008, "Simulation and Measurement of 3D Shear-Driven Thin Liquid Film Flow in a Duct," International Journal of Heat and Fluid Flow, **29**(2) pp. 449-459.

[3] Kumbur, E. C., Sharp, K. V., and Mench, M. M., 2006, "Liquid Droplet Behavior and Instability in a Polymer Electrolyte Fuel Cell Flow Channel," Journal of Power Sources, **161**(1) pp. 333-345.

[4] Ous, T., and Arcoumanis, C., 2007, "Visualisation of Water Droplets during the Operation of PEM Fuel Cells," Journal of Power Sources, **173**(1) pp. 137-148.

[5] Fischer, B. J., 2002, "Particle Convection in an Evaporating Colloidal Droplet," Langmuir, **18**(1) pp. 60-67.

[6] Dunn, G. J., Wilson, S. K., Duffy, B. R., 2009, "The Strong Influence of Substrate Conductivity on Droplet Evaporation," Journal of Fluid Mechanics, **623**pp. 329-351.

[7] David, S., Sefiane, K., and Tadrist, L., 2007, "Experimental Investigation of the Effect of Thermal Properties of the Substrate in the Wetting and Evaporation of Sessile Drops," Colloids and Surfaces A: Physicochemical and Engineering Aspects, **298**(1-2) pp. 108-114.

[8] Kulinich, S. A., and Farzaneh, M., 2009, "Effect of Contact Angle Hysteresis on Water Droplet Evaporation from Super-Hydrophobic Surfaces," Applied Surface Science, **255**(7) pp. 4056-4060.

[9] Butt, H., Golovko, D. S., and Bonaccurso, E., 2007, "On the Derivation of Young's Equation for Sessile Drops: Nonequilibrium Effects due to Evaporation," Journal of Physical Chemistry B, **111**(19) pp. 5277-5283.

[10] Thomson, W., 1871, "On the Equilibrium of Vapour at a Curved Surface of Liquid," Philos. Mag., **42**(2) pp. 448-452.

[11] Ivchenko, I. N., 1979, "Evaporation of Spherical Drops Under Conditions of Thermostatic Control of their Surface," Fluid Dynamics, **14**(5) pp. 790-792.

[12] Ivchenko, I. N., and Muradyan, S. M., 1982, "Evaporation of Spherical Drops in a Binary Gas Mixture at Arbitrary Knudsen Numbers," Fluid Dynamics, **17**(1) pp. 92-97.

[13] Ivchenko, I. N., 1984, "The Evaporation and Growth of Spherical Droplets at Intermediate Knudsen Numbers," Fluid Dynamics, **19**(2) pp. 335-337.

[14] Ivchenko, I. N., 1985, "Heat and Mass Transfer during Evaporation Or Condensation Growth of Spherical Drops." High Temperature, **23**(4) pp. 634-638.

[15] Erbil, H. Y., and Dogan, M., 2000, "Determination of Diffusion Coefficient-Vapor Pressure Product of some Liquids from Hanging Drop Evaporation," Langmuir, **16**(24) pp. 9267-9273.

[16] Poulard, C., Guéna, G., and Cazabat, A., 2005, "Diffusion-Driven Evaporation of Sessile Drops," Journal of Physics Condensed Matter, **17**(49) pp. S4213-S4227.

[17] Poulard, C., Guéna, G., Cazabat, A., 2005, "Rescaling the Dynamics of Evaporating Drops," Langmuir, **21**(18) pp. 8226-8233.

[18] Maxwell, J.C., 1890, "Collected Scientific Papers,"Cambridge, pp. 628.

[19] Slattery, J.C., 1999, "Advanced Transport Phenomena,"Cambridge, pp. 21-426,459.

[20] Fick, A., 1855, "On Liquid Diffusion," Philos. Mag. J. Sci., **10**pp. 31-39.

[21] Fick, A., 1856, "Sulla Diffusione Dei Liquini," Il Nuovo Cimento, **3**(1) pp. 244-245.

[22] Taylor, R., and Krishna, R., 1993, "Multicomponent Mass Transfer," John Wiley &Sons Inc., New York, .

[23] Jiji, L.M., 2003, "Heat Conduction," Begel House Inc., New York, .

[24] Guena, G., Poulard, C., and Cazabat, A., 2007, "The Dynamics of Evaporating Sessile Droplets," Colloid Journal, **69**(1) pp. 1-8.

[25] Guéna, G., Poulard, C., and Cazabat, A., 2007, "The Leading Edge of Evaporating Droplets," Journal of Colloid and Interface Science, **312**(1) pp. 164-171.

[26] Shahidzadeh-Bonn, N., Rafaï, S., Azouni, A., 2006, "Evaporating Droplets," Journal of Fluid Mechanics, **549**pp. 307-313.

[27] Markham, B. L., and Rosenberger, F., 1980, "Velocity and Concentration Distribution in a Stefan Diffusion Tube." Chemical Engineering Communications, **5**(5-6) pp. 287-298.

[28] Mitchem, L., Buajarern, J., Hopkins, R. J., 2006, "Spectroscopy of Growing and Evaporating Water Droplets: Exploring the Variation in Equilibrium Droplet Size with Relative Humidity," J. Phys. Chem. A, **110**(26) pp. 8116-8125.

[29] Pruppacher, H. R., and Rasmussen, R., 1979, "A Wind Tunnel Investigation of the Rate of Evaporation of Large Water Drops Falling at Terminal Velocity in Air." Journal of the Atmospheric Sciences, **36**(7) pp. 1255-1260.

[30] Bhalwankar, R. V., Sathe, A. B., and Kamra, A. K., 2004, "The Evaporation of the Charged and Uncharged Water Drops Suspended in a Wind Tunnel," Proceedings of the Indian Academy of Sciences, Earth and Planetary Sciences, **113**(2) pp. 129-138.

[31] Watts, R. G., 1971, "Relaxation Time and Steady Evaporation Rate of Freely Falling Raindrops," J. Atmos. Sci., **28**pp. 219-225.

[32] Cussler, E.L., 2003, "Diffusion, mass transfer in fluid systems," Cambridge, .

[33] Tonini, S., 2009, "Heat and Mass Transfer Modeling of Submicrometer Droplets Under Atmospheric Pressure Conditions," Atomization Sprays, **19**(9) pp. 833-846.

[34] Sreznevsky, V., 1882, Zhurnal Fizicheskoi Khimii, **14**(420) pp. 483.

[35] Shi, L., Shen, P., Zhang, D., 2009, "Wetting and Evaporation Behaviors of Water-Ethanol Sessile Drops on PTFE Surfaces," Surface and Interface Analysis, **41**(12-13) pp. 951-955.

[36] Soolaman, D. M., and Yu, H. Z., 2005, "Water Microdroplets on Molecularly Tailored Surfaces: Correlation between Wetting Hysteresis and Evaporation Mode Switching," Journal of Physical Chemistry B, **109**(38) pp. 17967-17973.

[37] Song, H., Lee, Y., Jin, S., 2008, "Sessile drop evaporation on surfaces of various wettability," 2008 Proc. ASME Micro/Nanoscale Heat Transfer Int. Conf., MNHT 2008, Anonymous **PART A,** pp. 445-451.

[38] Liu, C., Bonaccurso, E., and Butt, H., 2008, "Evaporation of Sessile Water/Ethanol Drops in a Controlled Environment," Phys. Chem. Chem. Phys., **10**(47) pp. 7150-7157.

[39] Shanahan, M. E. R., and Bourgès, C., 1994, "Effects of Evaporation on Contact Angles on Polymer Surfaces," International Journal of Adhesion and Adhesives, **14**(3) pp. 201-205.

[40] Shin, D. H., Lee, S. H., Jung, J. -., 2009, "Evaporating Characteristics of Sessile Droplet on Hydrophobic and Hydrophilic Surfaces," Microelectronic Eng., **86**(4-6) pp. 1350-1353.

[41] Cioulachtjian, S., Launay, S., Boddaert, S., 2010, "Experimental Investigation of Water Drop Evaporation Under Moist Air Or Saturated Vapour Conditions," Int. J. Thermal Sci., **49**(6) pp. 859-866.

[42] Picknett, R. G., and Bexon, R., 1977, "The Evaporation of Sessile Or Pendant Drops in Still Air," Journal of Colloid and Interface Science, **61**(2) pp. 336-350.

[43] Birdi, K. S., Vu, D. T., and Winter, A., 1989, "A Study of the Evaporation Rates of Small Water Drops Placed on a Solid Surface," Journal of Physical Chemistry, **93**(9) pp. 3702-3703.

[44] Fang, X., Li, B., Petersen, E., 2005, "Factors Controlling the Drop Evaporation Constant," Journal of Physical Chemistry B, **109**(43) pp. 20554-20557.

[45] Bourgès-Monnier, C., and Shanahan, M. E. R., 1995, "Influence of Evaporation on Contact Angle," Langmuir, **11**(7) pp. 2820-2829.

[46] Erbil, H. Y., McHale, G., and Newton, M. I., 2002, "Drop Evaporation on Solid Surfaces: Constant Contact Angle Mode," Langmuir, **18**(7) pp. 2636-2641.

[47] Rowan, S. M., Newton, M. I., and McHale, G., 1995, "Evaporation of Microdroplets and the Wetting of Solid Surfaces," Journal of Physical Chemistry, **99**(35) pp. 13268-13271.

[48] Furuta, T., Sakai, M., Isobe, T., 2009, "Evaporation Behavior of Microliter- and Sub-Nanoliter-Scale Water Droplets on Two Different Fluoroalkylsilane Coatings," Langmuir, **25**(20) pp. 11998-12001.

[49] McHale, G., Rowan, S. M., Newton, M. I., 1998, "Evaporation and the Wetting of a Low-Energy Solid Surface," Journal of Physical Chemistry B, **102**(11) pp. 1964-1967.

[50] Dhavaleswarapu, H. K., Migliaccio, C. P., Garimella, S. V., 2010, "Experimental Investigation of Evaporation from Low-Contact-Angle Sessile Droplets," Langmuir, **26**(2) pp. 880-888.

[51] Widjaja, E., and Harris, M. T., 2008, "Numerical Study of Vapor Phase-Diffusion Driven Sessile Drop Evaporation," Comput. Chem. Eng., **32**(10) pp. 2169-2178.

[52] Barash, L. Y., Bigioni, T. P., Vinokur, V. M., 2009, "Evaporation and Fluid Dynamics of a Sessile Drop of Capillary Size," Phys. Rev. E, **79**(4) .

[53] Deegan, R. D., 2000, "Pattern Formation in Drying Drops," Phy. Rev. E, **61**(1) pp. 475-485.

[54] Deegan, R. D., Bakajin, O., Dupont, T. F., 2000, "Contact Line Deposits in an Evaporating Drop," Phys. Rev. E, **62**(1 B) pp. 756-765.

[55] Jackson, J.D., 1998, "Classical Electrodynamics,"John Wiley& Sons Inc., pp. 75.

[56] Deegan, R. D., Bakajin, O., Dupont, T. F., 1997, "Capillary Flow as the Cause of Ring Stains from Dried Liquid Drops," Nature, **389**(6653) pp. 827-829.

[57] Lebedev, N.N., 1965, "Special Functions and their Applications,"Prentice-Hall Inc., pp. 227.

[58] Berteloot, G., Pham, C. -., Daerr, A., 2008, "Evaporation-Induced Flow Near a Contact Line: Consequences on Coating and Contact Angle," EPL, **83**(1) .

[59] Erbil, H. Y., 2012, "Evaporation of Pure Liquid Sessile and Spherical Suspended Drops: A Review," Advances in Colloid and Interface Science, **170**(1-2) pp. 67-86.

[60] Golovko, D. S., Bonanno, P., Lorenzoni, S., 2008, "Evaporative Cooling of Sessile Water Microdrops Measured with Atomic Force Microscope Cantilevers," Journal of Micromechanics and Microengineering, **18**(9) .

[61] Rienstra, S. W., 1990, "The Shape of a Sessile Drop for Small and Large Surface Tension," Journal of Engineering Mathematics, **24**(3) pp. 193-202.

[62] Anonymous "Exponential Integral," .

[63] Stefan, J., 1890, "The Evaporation and Melting Phenomena such as Diffusion (Über Die Verdampfung Und Die Auflösung Als Der Vorgänge Diffusion)," SAW Philosophisch Historische-Klasse, **98**pp. 1418-1422.

[64] Stefan, J., 1890, "Über Die Theorie Der Eisbildung." Monatshefte Für Mathematik Und Physik, **1**(1) pp. 1-6.

[65] Stefan, J., 1872, "The Dynamic Theory of Diffusion of Gases (Über Die Theorie Der Dynamische Didffusion Der Gase)," SAW, **65**pp. 159-187.

[66] Som, S.K., 2008, "Introduction to heat transfer," Eastern Economy Edition, New Delhi, India, .

[67] Slattery, J. C., and Mhetar, V. R., 1997, "Unsteady-State Evaporation and the Measurement of a Binary Diffusion Coefficient," Chem. Eng. Sci., **52**(9) pp. 1511-1515.

[68] Slattery, J.C., Sagis, L., and Oh, E., 2007, "Interfacial Transport Phenomena,"Springer, pp. 70-736.

[69] Kelly-Zion, P. L., Pursell, C. J., Vaidya, S., 2011, "Evaporation of Sessile Drops Under Combined Diffusion and Natural Convection," Colloids and Surfaces A: Physicochemical and Engineering Aspects, **381**(1–3) pp. 31-36.

[70] Perry, R.H., and Green, D.W., 1997, "Chemical Engineering Handbook," McGraw-Hill Book Co., New York, .

[71] Cengel, Y.A., 2003, "Heat transfer a practical approach," McGraw-Hill Book Co., New York, pp. 857-868.

Chapter 5 - Effect of Buoyancy on Evaporation of Sessile and Pendant Drops

5.0 Introduction

The main goal of this study is to gain further insight into the process of drop evaporation, specifically, the effects of buoyancy. The study was done at room temperature, atmospheric pressure, and quiescent environment. As explained in Chapter 4, evaporation of micro-liter drops in room temperature is limited by vapor transport from the drop surface and not the phase change. The vapor transport can be decomposed into diffusion and convection (bulk motion). Literature models (based on Maxwell's assumptions) assume that the convection part of vapor transport is negligible and the process is a steady-state process. In Chapter 4, it was shown that none of these two assumptions are correct for this problem; however for the range of parameters for micro-liter drops the effects of convection and transient term cancel each other. Therefore, a pure diffusive and transient model (which is easy to derive and use) provides accurate results. The convection that was discussed above does not take into account the effect of gravity and buoyancy (discussed in Chapter 4). Potentially, buoyancy may increase or decrease the evaporation rate through changing the bulk motion of vapor (or convection) that occurs [1-5]

Buoyancy can be caused by temperature [2, 3, 6], or density [5] variations. As the temperature is assumed to be uniform, the latter is the interest of this study. There are opposing theories on the effect of density-driven buoyancy on drop evaporation [7-10]. To observe the importance of buoyancy on drop evaporation, literature studies have compared the evaporation rate of sessile and pendant drops at similar experimental situation (similar drop volume and substrate). For example, consider water as the liquid. Water vapor is lighter than air. Therefore, during the evaporation of sessile water drops buoyancy may potentially increase the evaporation rate. Whereas for pendant water drops buoyancy moves the vapor up and back to the drop. As such, potentially sessile water drops should evaporate faster than pendant water drops. In general depending on the weight of the liquid vapor, sessile and pendant water drops should evaporate at different rates. Now, the question to be answered is how large is the effect of buoyancy on evaporation?

Through the comparison, some literature has observed a notable difference between evaporation rate of sessile and pendant drops and suggested that buoyancy's effect is important. For example, in [3] using the Schlieren imaging technique, it was suggested that in evaporation of liquid hydrocarbons the effect of buoyancy is not negligible (other examples are in [2, 3, 5, 11]). However, some studies observed a negligible or no difference between the evaporation rate of sessile and pendant drops [7-9].

There is no systematic study in literature which can answer the following questions: Is there a notable difference between evaporation of pendant and sessile drops (similar volume and substrate)? Is buoyancy a dominant factor in creating the difference? In this study we found that there is a notable difference between the evaporation rate of sessile and pendant drops. However, through a systematic experiment it was shown that the difference cannot be attributed to buoyancy. Instead, other parameters are introduced which are believed to be far more important than buoyancy. To tackle this problem the experimental setup outlined below was used.

5.1 Experimental Methods

To test buoyancy's role in drop evaporation, evaporation of different liquids with vapor weights heavier and lighter than air were studied. To account for possible effect of substrate, drop evaporation was studied on different substrates. Experiments were performed in normal laboratory condition (pressure: 94kPa, temperature: 21^{o}, and relative humidity: 40%); and temperatures of the surrounding gas phase, substrate and drop were uniform. Drop images were taken with Basler A302fs CCD and Navitar 67X NIRA cameras (see Fig. 5-1). Real Drip Drop© was used to import the camera's images, and images were processed using the in-house developed software *SPPF* ver. 4.2 [12]. A Sartorius TE214S scale was integrated into a computer via a printer port, which was able to give a reading every five seconds to an Excel file. The scale was put in an opaque box to mitigate radiation and airflow effects while still being large enough so that diffusion can still proceed without interference. A stand measuring 15cm high was constructed to support the substrate in the pendant conformation (see Fig. 5-1a). This height was chosen to avoid any wall effects. A Fisher micropipette was held vertically when placing the drops onto the substrate. To place a pendant drop, the substrate was placed on the stand and the pipette was inverted to place the drop, which was found to be the most consistent method. An air stream was used on the substrate and enclosure before every experiment to ensure all liquid was purged from the substrate and no vapor was trapped within the box. As shown in Chapter 4, variation of $m^{2/3}$ versus t is linear. The slope of that line was used as an indication of evaporation rate (similar to [13]); and evaporation rate of sessile and pendant drops were compared using t-tests. To record the drop images (see Fig. 5-1b), another opaque box was used to limit radiation from the room, but in order to capture images a light had to be placed within the box, producing radiation on the sample. This meant that the experiment environment involving mass measurements was not the same as that for the experiments where images were recorded. The purpose of recording the drop images was to trace the drop evolution shape during the evaporation. Each experiment was repeated nine times and averages are presented.

5.1.1 Surface Preparation

The four substrates were used in the experiments included an aluminum plate (25x49x1.5 mm), glass slide (26x76x1 mm), silicon wafer (Ultrasil, 20x44x0.5 mm) and poly(methyl methacrylate) (PMMA) coated silicon wafer (19x45x0.5 mm). Silicon was chosen as it is smooth, homogeneous and rigid. The PMMA coated silicon wafer was produced using spin coating technique at 2400 RPM and PMMA powders (Aldrich®) were diluted with Toluene (Fisher Chemical) with solute concentration of 3% w/w. After spin coating, coated silicon wafers were put in an oven for 24 hours at 100^oC. Roughness of the PMMA coated silicon was found to be similar to the roughness of silicon before coating, *i.e.* $50 \pm 10nm$. Roughness was measured with Axio CSM-700 Confocal Microscope with scanning resolution of $20nm$. The aluminum, glass, and silicon substrates were placed in a diluted chromo-sulfuric acid for a minimum of 24 hours and rinsed with acetone, ethanol, distilled water and dried under heat lamp in a chamber. After each experiment, the substrates were washed with methanol followed by acetone and rinsed with distilled water and dried with blowing nitrogen. The surfaces were kept isolated from the environment when not in use to avoid contamination.

5.1.2 Liquids

The liquids used in these experiments were DI water (DirectQ Millipore) and iso-butanol (Anachemia, 99%). The molar mass of water is $18.02g/mol$, which is lighter than air $29g/mol$. Other tested liquids have molar masses heavier than air (see Table 5-1). From Avogadro's law, at constant temperature, the molar volume of a gas is a constant so the molar mass corresponds directly to density [14].

Table 5-1 Molar Mass of studied liquids (from [15]).

	DI-Water (H_2O)	Iso-butanol ($C_4H_{10}O$)
Molar Mass (g/mol)	18.02	74.12

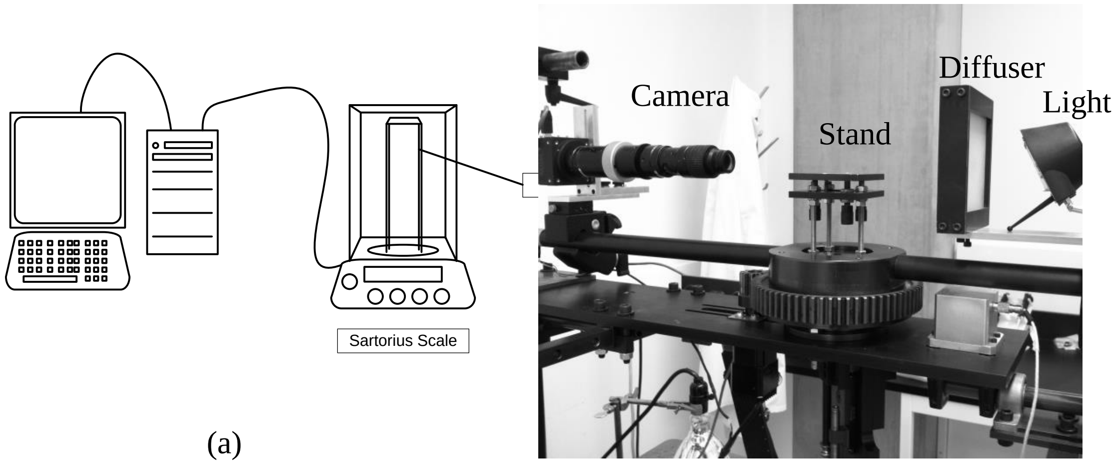

(a)

(b)

Fig. 5-1 Experimental setup for (a) measuring the drop weight and (b) recording the drop image during evaporation are shown. The stand in (a) is for holding the substrate for pendant drop cases.

5.2 Results and Discussion

Drops ($4\mu L$) were placed on aluminum, glass, poly methyl methacrylate (PMMA) coated silicon, and silicon substrates in both sessile and pendant conformations. If buoyancy is a deterministic factor in evaporation rate, sessile water drop should potentially evaporate faster than pendant. And Iso-butanol should potentially evaporate faster in pendant conformation. For comparing the evaporation rates, the slope of drop mass raised to the power of 2/3 ($m^{2/3}$) in time (t) is used and larger slope means higher evaporation rate. In Chapters 4 and 6 it was shown that for evaporation of drops the change of $m^{2/3}$ in time is linear. A t-test with 95% confidence level was performed to compare the slope of $m^{2/3}$ in time for sessile and pendant drops. It should be noted that for very small drops, some extra factors (*e.g.* Kelvin effect) can take over [16]; therefore, the slope of $m^{2/3}$ in time is only calculated for the first half-life of evaporating drop.

Table 5-2 Evaporation rate of $4\mu l$ sessile and pendant iso-butanol drops on glass, aluminum, and silicon substrates.

Substrate	Slope of $m^{2/3} vs. t\ (\mu g/s)$		Significantly Different at 95% confidence interval
	Sessile	Pendant	
Glass	40 ± 3	34 ± 3	Yes
Aluminum	58 ± 6	48 ± 4	Yes
Silicon	60 ± 3	51 ± 5	Yes

Table 5-3 Evaporation rate of $4\mu l$ water drop on glass, aluminum, silicon, and PMMA-coated silicon substrates.

Substrate	Slope of $m^{2/3} vs. t\ (\mu g/s)$		Significantly Different at 95% confidence interval
	Sessile	Pendant	
Glass	31 ± 1	22.4 ± 0.3	Yes
Aluminum	12.1 ± 0.1	10.1 ± 0.5	No
Silicon	22 ± 1	18.2 ± 0.3	Yes
PMMA coated Silicon	16.4 ± 0.4	13.3 ± 0.4	Yes

It was found that for both water (which its vapor is lighter than air) and iso-butanol (which its vapor is heavier than air), sessile drops evaporate faster than pendant drops; see Tables 5-2 and 5-3. The “Significantly Different” column in Tables 5-1 and 5-2 indicates that the difference between the evaporation rate of sessile and pendant drops is significant (with 95% confidence level).

Having water evaporate faster in the sessile case agrees with the belief that buoyancy would help the lighter-than-air water vapor evaporate quicker than the pendant case. However, iso-butanol should have had faster evaporation rate in the pendant conformation under the influence of buoyancy as their vapor is heavier than air. This may mean that the effect of buoyancy is not a major factor in drop evaporation.

On a separate note, as shown in Tables 5-2 and 5-3, iso-butanol drops evaporate faster than water drops. This is expected since water has higher surface tension than iso-butanol. As discussed in Chapter 6 the evaporation rate is higher near the contact line [17, 18]; since iso-butanol has a larger contact line, it may potentially have a faster evaporation than water drop.

Next, other possible factors which may contribute in creating the difference between evaporation rate of sessile and pendant drops will be studied. One of these factors is the drop shape change due to the gravity. For micro-liter drops Bond number value is low ($Bo = \frac{\Delta\rho g L^2}{\gamma}$, $\Delta\rho$ is the density difference between the liquid-vapor interface, g is the gravitational acceleration, L is a characteristic length and is equal to $3V/S$, and γ is the surface tension) [19]. As such, gravitational forces should not affect the drop's shape, meaning that sessile and pendant drops should have the same shape (see Fig. 5-2). This is also tested using image processing methods and comparing the shape of similar drop volumes and surfaces in sessile and pendant configurations.

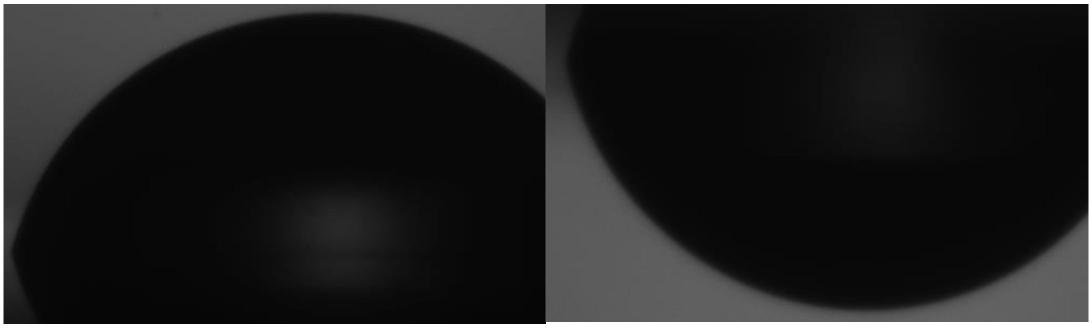

(a) (b)

Fig. 5-2 Images of (a) sessile and (b) pendant water drops on PMMA-coated silicon are shown.

To better verify that sessile and pendant micor-liter drops have similar shapes, the sphericity (ψ) definition was used, see Eq. 5-1.

$$\psi = \frac{\pi^{1/3}(6V)^{2/3}}{S} \tag{5-1}$$

where V is the volume and S is the surface area of the drop. A sphere has a sphericity of unity. If drop is affected by gravity, its shape deviates from spherical cap to ellipsoidal cap shape [20-23], and the value of sphericity deviates from unity. Assuming that drop is axisymmetric, one of the symmetrical axes of the ellipsoid (which the ellipsoidal cap is a portion of that) becomes perpendicular to the substrate and the other axis of symmetry is parallel to the substrate (*e.g.* Fig. 5-3). The volume and surface area of an ellipsoidal cap shape drop can be found from Eqs. 5-2 and 5-3:

$$V = \frac{4}{3}\pi {r_1}^2 r_2 \tag{5-2}$$

$$S = 2\pi {r_1}^2 + \frac{2\pi r_1 {r_2}^2}{\sqrt{{r_2}^2 + {r_1}^2}} \sin^{1-} \frac{\sqrt{{r_2}^2 - {r_1}^2}}{r_2} \tag{5-3}$$

where r_1 and r_2 are minor and major radii of the ellipse (see Fig 5-3).

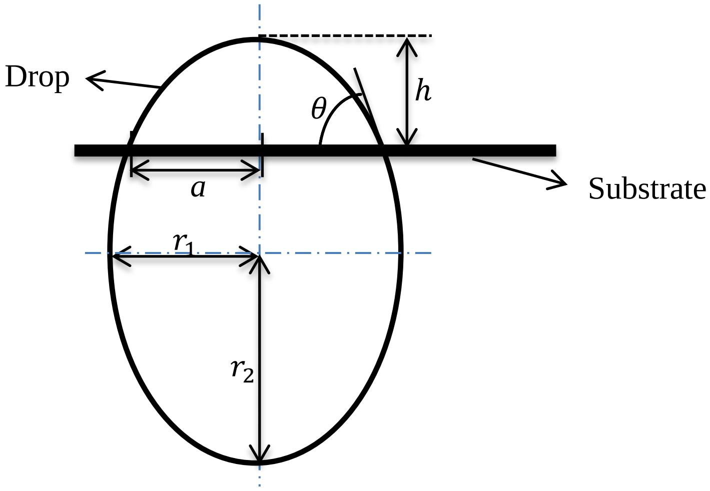

Fig. 5-3 An ellipsoidal cap shape drop with drop height (h), wetted radius (a), and contact angle (θ) is shown in 2-D. The ellipsoidal cap (which represents a drop affected by gravity) is a portion of an ellipsoidal shape with major and minor radii of r_1 and r_2.

In the case of drops, the values of r_1 and r_2 cannot be measured from the drop image. Instead, the values of drop height (h), wetted radius (a), and contact angle (θ) can be found using the drop images and image processing [12]. In the following, r_1 and r_2 are found as functions of h, a, and θ. The general equation of an ellipse with minor and major radii of r_1 and r_2 is:

$$\frac{x^2}{{r_1}^2}+\frac{y^2}{{r_2}^2}=1 \tag{5-4}$$

At $x = a$, the tangent to the ellipse is θ degrees with respect to the x-axes (see Fig. 5-3), as such one has:

$$\left.\frac{dy}{dx}\right|_{x=a} = -tan\theta \tag{5-5}$$

Using Eqs. 5-4 and 5-5 one can find the value of r_1 and r_2 based on the drop height (h), wetted radius (a), and contact angle (θ) as:

$$r_2 = \frac{ah\tan\theta - h^2}{a\tan\theta - 2h} \tag{5-6}$$

and:

$$r_1 = \sqrt{\frac{a(a\tan\theta - h)^2}{\tan\theta\,(a\tan\theta - 2h)}} \tag{5-7}$$

It was found that the sphericity of sessile and pendant water drops is 0.95 ± 0.01 and 0.96 ± 0.01, respectively. These two values are reasonably similar which indicates that sessile and pendant drops have relatively similar shapes. Also, as the sphericity values are close to unity, it can be concluded that both sessile and pendant drops have spherical cap shapes. It should be noted that the sphericity check is done for drops at the beginning of evaporation. This will provide a conservative estimate of ψ, as during the evaporation drop size shrinks and sphericity approaches unity. Above, discussion shows that the initial drop shape cannot explain the difference between the evaporation of pendant and sessile drops.

The other hypothesis for explaining the difference between evaporation rate of sessile and pendant drops is based on evaporation modes. According to Picknett and Bexon [11], for evaporation of pure sessile drops, the following two drop shape changes or a combination of them is expected: (i) decrease of the wetted area with constant θ; and (ii) constant wetted area with decreasing θ. Each of these drop evolution cases is called an evaporation mode [24-27]. According to Picknett and Bexon [11] evaporation in constant wetted area (CWA) mode is faster than that in constant contact angle (CCA) mode. Literature states that evaporation of drops usually begins in the CWA mode, and then switches to the CCA mode [13, 28, 29]. As such, if compared to the evaporation of pendant drops, the sessile drops stay longer in the CWA mode, evaporation rate of the sessile drops become faster. This is the case here. As shown in Table 5-4, a $4\mu l$ sessile water drop stays for $318\,s$ in the CWA mode, whereas a $4\mu l$ pendant water drop stays for $274\,s$ in the CWA mode. In summary, it was found that during the evaporation, sessile drops stay longer in the CWA mode (with 95% confidence). As such, sessile drops evaporate faster than pendant drops. This is consistent with the observations in Tables 5-2 and 5-3.

Table 5-4 Time spent in CWA (constant wetted area) or CCA (constant contact angle) modes during the evaporation of a $4\mu l$ water drop from PMMA-coated silicon.

Conformation	CWA (s)	CCA (s)	Lifetime (s)	% in CWA	% in CCA
Sessile	318 ± 77	820 ± 51	1138 ± 98	28 ± 5	72 ± 5
Pendant	274 ± 40	931 ± 90	1205 ± 114	23 ± 2	77 ± 2

The results of this chapter show that buoyancy is not a dominant factor in evaporation of sessile and pendant drops. The difference between the evaporation rate of sessile and pendant drops is due to the time spent in evaporation modes.

5.3 Summary and Conclusions

Evaporation of micro-liter drops in room temperature is restricted by movement of vapor from the drop surface, and not the phase change. The vapor movement can be decomposed into diffusion and convection (bulk movement). The convection term discussed above excludes the buoyancy. As different liquids have different vapor weights, buoyance may potentially increase or decrease the convection and evaporation rate, consequently. For example, water vapor is lighter than air and sessile water drops should evaporate faster than pendant water drops. Based on the agreement of the above statement and experimental observations, some literature studies have concluded that buoyancy has a dominant effect on evaporation of drops. However, literature judgments on the effect of buoyancy are divided. In this study, it was found that buoyancy is not a dominant factor on evaporation of drops, and the difference between the evaporation rate of sessile and pendant drops has a different source. For instance, evaporation of iso-butanol which its vapor is heavier than air is studied. Due to the buoyancy effect the pendant iso-butanol drop should potentially evaporate faster than a sessile. However, the opposite was observed. This disproves the hypothesis that buoyancy effect is significant. The cause of evaporation rate difference between sessile and pendant drops was found to be related to the evaporation modes. Evaporation typically occurs in CWA and CCA modes. Theoretically it was shown in literature that evaporation rate is faster in the CWA mode. It was found that sessile drops spend more time in the CWA mode compared with pendant drops (with %95 confidence and using t-test). This causes the sessile drops to evaporate faster than pendant drops, and buoyancy is not the cause of the difference between the evaporation rate of sessile and pendant drops.

5.4 References

[1] Guena, G., Poulard, C., and Cazabat, A., 2007, "The Dynamics of Evaporating Sessile Droplets," Colloid Journal, **69**(1) pp. 1-8.

[2] Kelly-Zion, P. L., Pursell, C. J., Vaidya, S., 2011, "Evaporation of Sessile Drops Under Combined Diffusion and Natural Convection," Colloids and Surfaces A: Physicochemical and Engineering Aspects, **381**(1-3) pp. 31-36.

[3] Kelly-Zion, P. L., Pursell, C. J., Booth, R. S., 2009, "Evaporation Rates of Pure Hydrocarbon Liquids Under the Influences of Natural Convection and Diffusion," International Journal of Heat and Mass Transfer, **52**(13-14) pp. 3305-3313.

[4] Poulard, C., Guéna, G., and Cazabat, A. M., 2005, "Diffusion-Driven Evaporation of Sessile Drops," Journal of Physics Condensed Matter, **17**(49) pp. S4213-S4227.

[5] Shahidzadeh-Bonn, N., Rafaï, S., Azouni, A., 2006, "Evaporating Droplets," Journal of Fluid Mechanics, **549**pp. 307-313.

[6] Dunn, G. J., Wilson, S. K., Duffy, B. R., 2009, "The Strong Influence of Substrate Conductivity on Droplet Evaporation," Journal of Fluid Mechanics, **623**pp. 329-351.

[7] Guena, G., Poulard, C., and Cazabat, A. -., 2007, "The Dynamics of Evaporating Sessile Droplets," Colloid Journal, **69**(1) pp. 1-8.

[8] Guéna, G., Poulard, C., and Cazabat, A. M., 2007, "The Leading Edge of Evaporating Droplets," Journal of Colloid and Interface Science, **312**(1) pp. 164-171.

[9] Guéna, G., Poulard, C., and Cazabat, A. M., 2007, "Evaporating Drops of Alkane Mixtures," Colloids and Surfaces A: Physicochemical and Engineering Aspects, **298**(1-2) pp. 2-11.

[10] Guéna, G., Poulard, C., and Cazabat, A. M., 2006, "The Contact Angle of Droplets Evaporating at Ambient Temperature," Applied Mathematics Research eXpress, **2006** pp. 1-16.

[11] Picknett, R. G., and Bexon, R., 1977, "The Evaporation of Sessile Or Pendant Drops in Still Air," Journal of Colloid and Interface Science, **61**(2) pp. 336-350.

[12] Chini, S. F., and Amirfazli, A., 2011, "A Method for Measuring Contact Angle of Asymmetric and Symmetric Drops," Colloids and Surfaces A: Physicochemical and Engineering Aspects, **388**(1-3) pp. 29-37.

[13] Erbil, H. Y., McHale, G., and Newton, M. I., 2002, "Drop Evaporation on Solid Surfaces: Constant Contact Angle Mode," Langmuir, **18**(7) pp. 2636-2641.

[14] Cengel, Y.A., 2003, "Heat transfer a practical approach," McGraw-Hill Book Co., New York, pp. 857-868.

[15] Perry, R.H., and Green, D.W., 1997, "Chemical Engineering Handbook," McGraw-Hill Book Co., New York, .

[16] Erbil, H. Y., 2012, "Evaporation of Pure Liquid Sessile and Spherical Suspended Drops: A Review," Advances in Colloid and Interface Science, **170**(1-2) pp. 67-86.

[17] Hu, H., and Larson, R. G., 2002, "Evaporation of a Sessile Droplet on a Substrate," Journal of Physical Chemistry B, **106**(6) pp. 1334-1344.

[18] Deegan, R. D., Bakajin, O., Dupont, T. F., 1997, "Capillary Flow as the Cause of Ring Stains from Dried Liquid Drops," Nature, **389**(6653) pp. 827-829.

[19] Rienstra, S. W., 1990, "The Shape of a Sessile Drop for Small and Large Surface Tension," Journal of Engineering Mathematics, **24**(3) pp. 193-202.

[20] ElSherbini, A. I., and Jacobi, A. M., 2006, "Retention Forces and Contact Angles for Critical Liquid Drops on Non-Horizontal Surfaces," Journal of Colloid and Interface Science, **299**(2) pp. 841-849.

[21] ElSherbini, A. I., and Jacobi, A. M., 2004, "Critical Contact Angles for Liquid Drops on Inclined Surfaces," Progress in Colloid and Polymer Science, **128**pp. 57-62.

[22] ElSherbini, A. I., and Jacobi, A. M., 2004, "Liquid Drops on Vertical and Inclined Surfaces: II. A Method for Approximating Drop Shapes," Journal of Colloid and Interface Science, **273**(2) pp. 566-575.

[23] ElSherbini, A. I., and Jacobi, A. M., 2004, "Liquid Drops on Vertical and Inclined Surfaces: I. an Experimental Study of Drop Geometry," Journal of Colloid and Interface Science, **273**(2) pp. 556-565.

[24] Shanahan, M. E. R., and Bourgès, C., 1994, "Effects of Evaporation on Contact Angles on Polymer Surfaces," International Journal of Adhesion and Adhesives, **14**(3) pp. 201-205.

[25] Shin, D. H., Lee, S. H., Jung, J. -., 2009, "Evaporating Characteristics of Sessile Droplet on Hydrophobic and Hydrophilic Surfaces," Microelectronic Eng., **86**(4-6) pp. 1350-1353.

[26] Bourgès-Monnier, C., and Shanahan, M. E. R., 1995, "Influence of Evaporation on Contact Angle," Langmuir, **11**(7) pp. 2820-2829.

[27] Shi, L., Shen, P., Zhang, D., 2009, "Wetting and Evaporation Behaviors of Water-Ethanol Sessile Drops on PTFE Surfaces," Surface and Interface Analysis, **41**(12-13) pp. 951-955.

[28] Erbil, H. Y., and Dogan, M., 2000, "Determination of Diffusion Coefficient-Vapor Pressure Product of some Liquids from Hanging Drop Evaporation," Langmuir, **16**(24) pp. 9267-9273.

[29] Semenov, S., Starov, V. M., Rubio, R. G., 2011, "Evaporation of Sessile Water Droplets: Universal Behaviour in Presence of Contact Angle Hysteresis,"

Colloids and Surfaces A: Physicochemical and Engineering Aspects, **391**(1-3) pp. 135-144.

Chapter 6 - Evaporation of Sessile Drops

6.0 Introduction

In this chapter, evaporation of drops on horizontal solid surfaces (sessile drops) is studied. Using the results in Chapter 5, the models for sessile drops can be extended to pendant drops (drops hanging form a solid surface). The discussion is limited to evaporation of micro-liter drops at room temperature, normal atmospheric condition and in quiescent environment. For such drops, as explained in Chapter 4, Kelvin's effect can be assumed to be small. Also, as shown in [1, 2], the evaporation rate is considered not to be limited by the transfer rate of molecules across the liquid-vapor interface (phase change) but by the transfer from the drop surface to the surrounding (vapor transport). Transport of vapor from drop surface to the surrounding may potentially be attributed to diffusion, convection, or both [3, 4]. Solving the mass balance equations, Langmuir [5] showed that in pure convective driven problems, evaporation rate has to be proportional to the wetted radius squared (*i.e.* $\mathbf{J} \propto a^2$) and in pure diffusive driven problems evaporation rate has to be proportional to the wetted radius (*i.e.* $\mathbf{J} \propto a$). As Langmuir [5] and proceeding researchers observed that $\mathbf{J} \propto a$, they came to the conclusion that evaporation of micro-liter drops in room temperature is governed by diffusion and not convection *e.g.* [3, 4, 6-12]. It was also assumed that such evaporation is a steady-state process. The steady-state and non-convective assumptions (Maxwell assumptions) are widely used in literature for finding the evaporation rate of sessile drops. As shown in Chapter 4, evaporation is neither steady-state, nor non-convective. However, in the range of the relevant values for micro-liter drops in room temperature, the transient and convective terms cancel each other and the results from the transient-convective model are similar to the pure diffusive and steady-state model.

6.1 Evaporation Flux Variation Across the Drop Surface

In the case of sessile drops, the presence of a solid substrate affects the evaporation rate. As shown in [12-14], and discussed in the next paragraph, for sessile drops, vapor flux on the drop surface changes from a maximum at the contact line to a minimum at the drop apex. There are two categories of studies supporting the variation of evaporation flux from apex to contact line: (i) flow visualization techniques and (ii) solutions based on electrostatic analogies.

Regarding the flow visualization techniques, the flow inside the evaporating drop was attributed to the Marangoni flow [15]. From that, according to the following explanation it was concluded that the evaporation rate near the contact line is higher [10]. Surface tension is temperature dependent and decreases by increasing the temperature. Therefore, the high evaporation rate near the contact line may cause a temperature decrease and Marangoni flow, accordingly. Due to the following two reasons flow visualization techniques cannot provide a complete explanation for the high evaporation rate near the contact line. First, the flow inside the drop may have a different source *e.g.* capillary flow due to seed particles used for visualization [16]. Second, the temperature decrease may be attributed to the thermal conductivity of the substrate [9]. As such, in this thesis the flow visualization techniques are not used to find the evaporation flux variation along the drop surface.

Regarding the electrostatic analogies, two of the commonly used electrostatic analogies in literature are explained: (i) the problem of finding the fields and charge densities in two-dimensional corners and along edges [17], (ii) Exterior Dirichlet problem for a domain, bounded by two intersecting spheres or capacitance of the equiconvex lens [18]. The first analogy is mentioned in [19]. As the original electrostatic problem was for flat conducting surfaces, this analogy was only good for small contact angles where the drop surface was nearly flat. The second analogy was mentioned in [3, 4, 13, 20]. The only limitation of applying the second analogy is that the drop should have a spherical cap shape which is not a restriction especially for small drops, having small Bond numbers, *i.e.* Bo <<1 ($Bo = \frac{\rho_L g L^2}{\gamma}$, where ρ_L is the liquid density, g is the acceleration gravity, γ is the surface tension force and L is a characteristic length and is equal to $\frac{3V}{A}$ for drops; V and A are drop volume and surface area accordingly). In more details, the second analogy (exterior Dirichlet problem) relates the electrostatic potential of two intersecting spherical bowls [18] to the vapor concentration. As such, the derivative of the electrostatic potential or the electric field becomes analogous to the VCG (vapor concentration gradient). The original electrostatic problem was mentioned in [18] in Toroidal coordinates. Figure 6-1 shows the

Toroidal coordinates (α, β and symmetry in the third dimension) and compares it with the cylindrical coordianets (r, z and symmetry in azimuthal direction). The third dimension of Toroidal coordinates which is not shown in Fig. 6-1 makes a "donut" around the z axis.

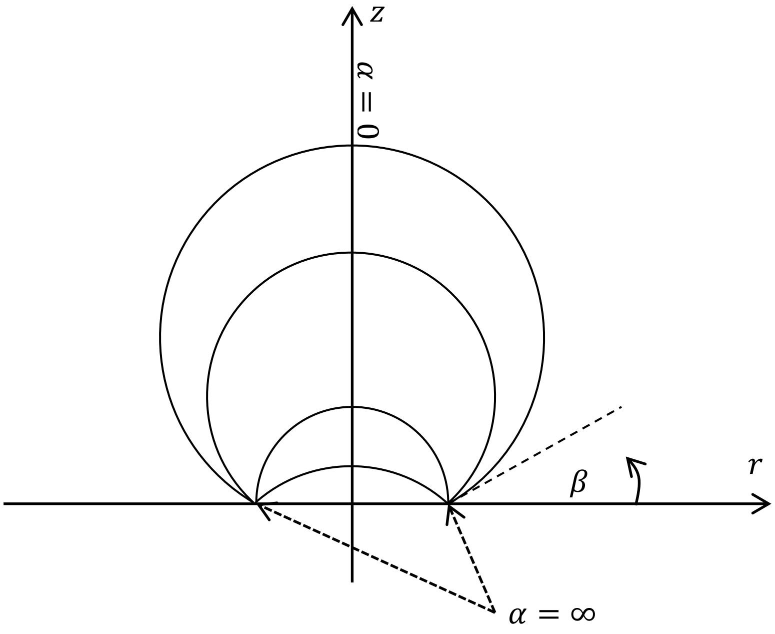

Fig. 6-1 Schematic of symmetrical Cylindrical coordinates (r, z) and symmetrical Toroidal coordinates (α, β) are shown.

It should be noted that the above electrostatic analogies are equivalent to the steady-state and non-convective evaporation problems. However, the steady-state and non-convective analogies are not restrictions. The reason is that the only purpose of using these analogies is finding the distribution of the evaporation flux across the drop surface. By having the distribution of evaporation flux along the drop surface at any moment, and using the transient-convective model developed in Chapter 4, evaporation rate of a sessile drop can be found.

6.2 Calculating the Evaporation Flux Distribution along the Drop Surface

For sessile drops due to the statement discussed in Section 6.1, the evaporation flux is not uniform on the drop surface. As explained in Section 6.1, the exterior Dirichlet problem is an electrostatic analogy problem for finding the evaporation flux distribution along the drop surface [16, 21, 22]. In the exterior Dirichlet problem the domain of β is: $\beta_2 < \beta < \beta_1 + 2\pi$. For two equal intersecting lenses the values for β_1 and β_2 are: $\beta_1 = \pi - \theta$ and $\beta_2 = \pi + \theta$. In Toroidal coordinates, by relating the analogous parameters, one has the following relation for the vapor concentration at different locations in the surface [18]:

$$w_v^\circ(\alpha,\beta) = \sqrt{2\cosh\alpha - 2\cos\beta} \times \left(w_{v\,eq}^\circ - w_{v\,\infty}^\circ\right) \tag{6-1}$$
$$\int_0^\infty \frac{\cosh((\pi-\beta_1)\tau) \times \sinh\big((\beta-\beta_2)\tau\big) + \cosh((\pi-\beta_2)\tau) \times \sinh\big((2\pi+\beta_1-\beta)\tau\big)}{\cosh(\pi\tau) \times \sinh\big((2\pi+\beta_1-\beta_2)\tau\big)}$$
$$\times P_{-1/2+i\tau}(\cosh\alpha)\,d\tau$$

where τ is a dummy variable, α is the Toroidal coordinate and is zero on the z-axis and infinity on the points on the edge of spheres (see Fig. 6-1) [18], and $P_{-1/2+i\tau}(\cosh\alpha)$ is the Legendre function of the complex degree with the argument of the hyperbolic function and may be found using Eq. 6-2 [18]:

$$P_{-{}^{1}\!/_{2}+i\tau}(\cosh\alpha) = \frac{2}{\pi}\coth(\pi\tau)\int_{\alpha}^{\infty}\frac{\sin(p\tau)}{\sqrt{2\cosh p - 2\cosh\alpha}}dp \tag{6-2}$$

$$= \frac{2}{\pi}\cosh(\pi\tau)\int_{0}^{\infty}\frac{\cos(p\tau)}{\sqrt{2\cosh p + 2\cosh\alpha}}dp$$

and, the value of $\cosh\alpha$ can be found as [18]:

$$\cosh\alpha = \left\{\left(\frac{x}{a}\right)^{2}\cos\theta + \left(1-\left(\frac{x}{a}\right)^{2}\sin^{2}\theta\right)^{\frac{1}{2}}\right\} \Big/ \left(1-\left(\frac{x}{a}\right)^{2}\right) \tag{6-3}$$

where x is the distance measured from apex (see Fig. 6-2). By taking derivative from Eq. 6-1 in Toroidal coordinates, one has [22]:

$$\nabla w_{v}^{\diamond}(\alpha,\beta = 2\pi+\beta_{1}) = \frac{\cosh\alpha-\cos\beta}{a}\left(\frac{\partial w_{v}^{\diamond}(\alpha,\beta)}{\partial\beta}\right)_{\beta=2\pi+\beta_{1}} \tag{6-4}$$

The term $\frac{\cosh\alpha-\cos\beta}{a}$ is called metric coefficient and appears when taking derivation in Toroidal coordinates. The relation for $\left(\frac{\partial w_{v}^{\diamond}(\alpha,\beta)}{\partial\beta}\right)_{\beta=2\pi+\beta_{1}}$ can be found by simple derivation with respect to β at $\beta = 2\pi+\beta_{1}$. Taking the derivative of Eqs. 6-1 with respect to β gives:

$$\left(\frac{\partial w_{v}(\alpha,\beta)}{\partial\beta}\right)_{\beta=3\pi-\theta} = \left(w_{v\,eq}^{\diamond} - w_{v\,\infty}^{\diamond}\right) \tag{6-5}$$

$$\left(\frac{\sin\theta}{\sqrt{2\cosh\alpha+2\cos\theta}}\times\int_{0}^{\infty}\frac{\cosh(\theta\tau)}{\cosh(\pi\tau)}\times P_{-{}^{1}\!/_{2}+i\tau}(\cosh\alpha)d\tau + \sqrt{2\cosh\alpha+2\cos\theta}\right.$$

$$\left.\times\int_{0}^{\infty}\tau\frac{\cosh(\theta\tau)}{\cosh(\pi\tau)}\tanh((\pi-\theta)\tau)\times P_{-{}^{1}\!/_{2}+i\tau}(\cosh\alpha)d\tau\right)$$

Using Eq. 4-5 and neglecting the convection (*i.e.* $u^{\diamond} = 0$) and Eqs. 6-4 and 6-5, one has:

$$J(\alpha,\theta) = -\rho^{\circ} D \frac{\cosh\alpha + \cos\theta}{a}\left(w^{\circ}_{v_{eq}} - w^{\circ}_{v_{\infty}}\right)\left(\frac{\sin\theta}{\sqrt{2\cosh\alpha + 2\cos\theta}} \times \int_0^{\infty} \frac{\cosh(\theta\tau)}{\cosh(\pi\tau)} \times P_{-1/2+i\tau}(\cosh\alpha)d\tau + \sqrt{2\cosh\alpha + 2\cos\theta} \times \int_0^{\infty} \tau \frac{\cosh(\theta\tau)}{\cosh(\pi\tau)} \tanh((\pi-\theta)\tau) \times P_{-1/2+i\tau}(\cosh\alpha)d\tau\right) \quad (6\text{-}6)$$

where $J(\alpha,\theta)$ is the evaporation flux at α for a sessile drop with contact angle of θ. It should be noted that α is in the Toroidal coordinates, using Eq. 6-3, the value of evaporation flux at different locations can be presented in cylindrical coordinates *i.e.* $J(\aleph,\theta)$ where $\aleph$ ($= \frac{x}{a}$, see Fig. 6-2). Finding the value of $J(\aleph,\theta)$ requires finding two double integrals (one integral is for the Legendre functions, see Eq. 6-2). Deegan *et al.* [20] proposed the following approximation for finding the value of $J(\aleph,\theta)$:

$$\frac{J(\aleph,\theta)}{J} \approx [1-\aleph^{m}]^{-\lambda} \quad (6\text{-}7)$$

where J is the evaporation flux for a fully spherical drop (see Chapter 4), m and λ are fitting parameters. Deegan *et al.* [20] used 2 for m and did not suggested any particular value for λ, but one may infer from their paper that they used the λ in [17], *i.e.* $\lambda = (180^{o} - 2\theta)/(360^{o} - 2\theta)$. However, the value of λ in [17] is for a different electrostatic problem. In the following, evaporation distribution along the drop surface is calculated and compared with approximate relations. For other approximate relations see [10].

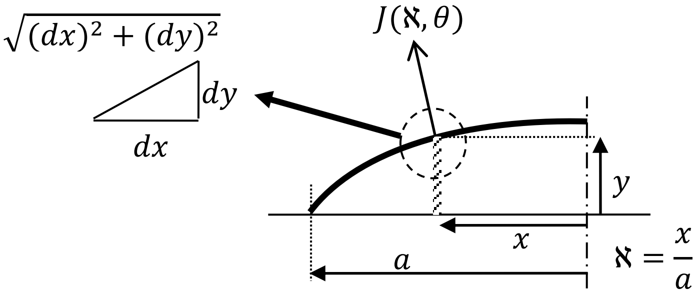

Fig. 6-2 Schematic of a half of a drop viewed from the side. The thick solid line represents the drop surface and the dashed-dotted line shows the plane of symmetry. The evaporation fluxes are shown at the drop apex and at x away from the apex.

As shown in [23], the following relation holds for Legendre integration:

$$\int_0^\infty \frac{\cosh(\theta\tau)}{\cosh(\pi\tau)} \times P_{-1/2+i\tau}(\cosh\alpha)d\tau = \frac{1}{\sqrt{2\cosh\alpha + 2\cos\theta}} \tag{6-8}$$

Using Eqs. 6-6 and 6-8 and knowing that $R = \frac{a}{\sin\theta}$ (see Fig. 1-2), the value of evaporation flux at different locations along the drop surface can be calculated as:

$$J(\alpha,\theta) = -\rho^{\circ} D \frac{w_{v_{eq}}^{\circ} - w_{v_{\infty}}^{\circ}}{R} \tag{6-9}$$

$$\left\{\frac{1}{2} + \frac{2(\cosh\alpha + \cos\theta)^{3/2}}{\pi\sin\theta} \int_0^\infty \frac{\tau\cosh(\theta\tau)\tanh((\pi-\theta)\tau)}{\sinh\,(\pi\tau)} \int_\alpha^\infty \frac{\sin(p\tau)}{\sqrt{\cosh p - \cosh\alpha}} dp\, d\tau\right\}$$

The value of α is in Toroidal coordinates and using Eq. 6-3 can be converted to the Cylindrical coordinates, *e.g.* $J(\aleph,\theta)$. Integrating the $J(\aleph,\theta)$ over the entire drop surface where the area element is $2\pi x\sqrt{(dx)^2+(dy)^2}$ (which is found using some geometry and knowing that $y(x) = \sqrt{(\frac{a}{\sin\theta})^2 - x^2} - a\cot\theta$, see Fig. 6-2) gives the total evaporation rate (**J**) as:

$$\mathbf{J} = 2\pi a^2 \int_0^1 \frac{\aleph}{\sqrt{1-\aleph^2 \sin^2\theta}} J(\aleph,\theta)\, d\aleph \tag{6-10}$$

The relation in Eq. 6-10 has three integrations. As shown in [24] these three integrals can be simplifies to one integral:

$$\mathbf{J} = -\pi a \rho^{\diamond} D \left(w^{\diamond}_{v\,eq} - w^{\diamond}_{v\,\infty}\right) \left\{ \frac{\sin\theta}{1+\cos\theta} + 4\int_0^{\infty} \frac{1+\cosh(2\theta\tau)}{\sinh(2\pi\tau)} \tanh((\pi-\theta)\tau)\, d\tau \right\} \tag{6-11}$$

Solving Eq. 6-11 gives the total evaporation from a sessile drop with taking into account the variation of evaporation flux along the drop surface. It should be noted that by neglecting the evaporation flux variation along the drop surface, using Maxwell's model, knowing that the surface area of a spherical cap shape drop can be calculated as $\frac{2\pi a^2}{1+\cos\theta}$, the total evaporation from a sessile drop would be:

$$\mathbf{J}_{uniform} = -2\pi a \rho^{\diamond} D \left(w^{\diamond}_{v\,eq} - w^{\diamond}_{v\,\infty}\right) \frac{\sin\theta}{1+\cos\theta} \tag{6-12}$$

where $\mathbf{J}_{uniform}$ is the total evaporation assuming the evaporation flux has no variation along the drop surface. Let $\zeta(\theta)$ be the ratio of $\frac{\mathbf{J}}{\mathbf{J}_{uniform}}$, its value can be found as:

$$\zeta(\theta) = \frac{\frac{\sin\theta}{1+\cos\theta} + 4\int_0^{\infty} \frac{1+\cosh(2\theta\tau)}{\sinh(2\pi\tau)} \tanh((\pi-\theta)\tau)\, d\tau}{2\frac{\sin\theta}{1+\cos\theta}} \tag{6-13}$$

The value of $\zeta(\theta)$ shows how much the evaporation value increases when evaporation flux variation along the drop surface is included. The value of $\zeta(\theta)$ is solved numerically, right Riemann sum, using MatLab (MathWorks R2010b) and results are shown in Fig. 6-3. It was found that $\zeta(\theta) \approx 60.27\theta^{-0.92}$. This is very important, as it makes the calculation of the evaporation rate for sessile drops very simple. One can assume a uniform evaporation flux along the drop surface and calculate the evaporation, then multiply the evaporation by $60.27\theta^{-0.92}$ to find the total evaporation with taking into account the evaporation variation along the drop surface.

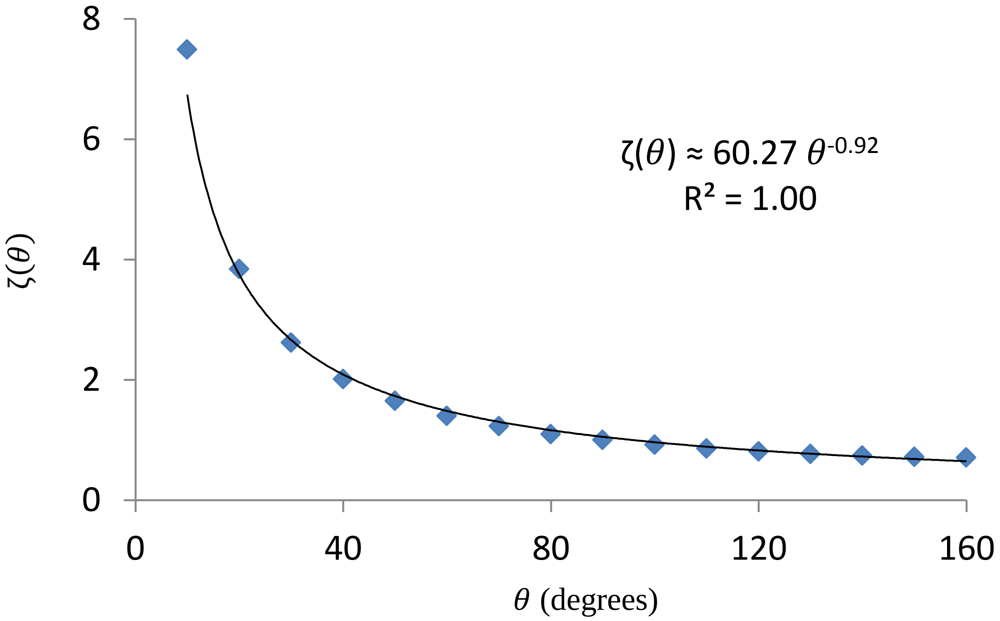

Fig. 6-3 The diamond symbols show the value of $\zeta(\theta)$ in Eq. 6-13. The value of $\zeta(\theta)$ is solved numerically in MatLab (right Riemann sum). The solid line is the $60.27\ \theta^{-0.92}$ which is a proper fit to $\zeta(\theta)$.

Literature studies have used different approaches for finding the value of $\zeta(\theta)$ *e.g.* differential mass balance, transforming the problem to other electrostatic problems or fitting the experimental values (*e.g.* [10, 14, 20-22, 25-31]). Among the literature studies, Picknett and Bexon [31] is the only one which provides an exact formula for taking into account the variation of evaporation flux along the drop surface. The analogy problem solved in Picknett and Bexon [31] study was finding the capacitance of a equiconvex lens formed by sessile drop and its image in the substrate surface. Other relations, (*e.g.* Bourgès-Monnier and Shanahan [11]) are approximate relations. As shown in Fig. 6-4 the value of $\zeta(\theta)$ found in Eq. 6-12 is equal to the value found by Picknett and Bexon [31]. Also Fig. 6-4 shows that by neglecting the variation of evaporation flux along the drop surface (*e.g.* Rowan [32]) the evaporation rate is underestimated.

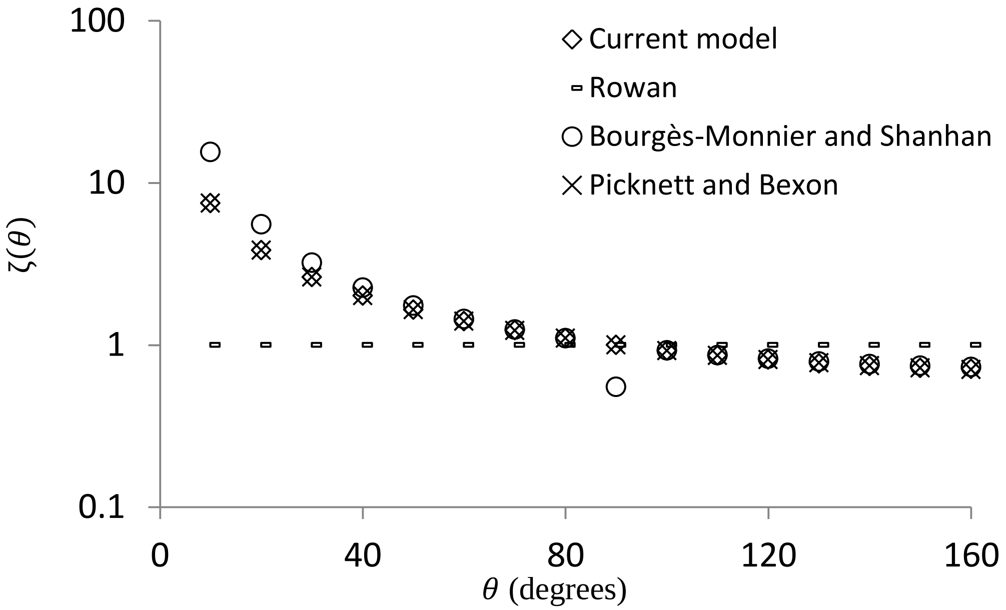

Fig. 6-4 The value of $\zeta(\theta)$ found from Eq. 6-12 is compared with the values found in Rowan *et al.* [32], Bourgès-Monnier and Shanhan [11] and Picknett and Bexon [31]. It should be noted that the model by Bourgès-Monnier and Shanhan has a singularity where contact angle (θ) is 90^o.

6.3 Evaporation Time for Sessile Drops

As discussed in Chapter 4, for spherical drops, using the evaporation flux, a radius versus time relation was found. By setting the radius equal to zero, one can solve the relation for t which is equal to the evaporation time. In the case of sessile drops, three independent parameters (*i.e.* wetted radius, a; drop height, h; and contact angle, θ, exist. As such, finding a relation similar to the one for spherical drops and solving for evaporation time needs more considerations. For spherical cap shape sessile drops, two of the three parameters are sufficient to define the drop volume and interface area *e.g.* see Eq. 6-14. Furthermore, as will be shown in Section 6.3.1, one out of the two independent parameters changes at a time. And the changing parameter can be used to find the evaporation time.

6.3.1 Sessile Drop Shape Change during Evaporation-Evaporation Modes

According to Picknett and Bexon [31], for evaporation of pure sessile drops, the following two drop shape changes or a combination of them is expected: (i) decrease of the wetted area with constant θ; and (ii) constant wetted area with decreasing θ. Each of these drop evolution cases is called an evaporation mode [11, 33-35]. It should be noted that for the evaporation of drops of liquid mixtures which is not the subject of this study, other modes may also occur *e.g.* see [35, 36].

As an aside, for predicting the drop evolution during evaporation, one should know the physical elements affecting the evaporation mode. According to literature, θ [37, 38], contact angle hysteresis, CAH (the difference between advancing, θ_A, and receding, θ_R contact angles) [31], or only θ_R [39], and surrounding air pressure [40, 41] may affect the evaporation mode. However, it is not well understood that which one has the dominant role in determining the evaporation mode, or at all. For example, consider a drop on a surface with $\theta<90^{o}$ and low CAH. For such a case, based on literature studies, predicting the evaporation mode is not possible.

6.3.1.1 Mode 1: Constant Contact Angle

Assuming that the evaporating drop has a spherical cap shape, drop volume (V) as a function of drop wetted radius and contact angle can be found as:

$$V = \frac{\pi(1-\cos\theta)(\cos\theta+2)a^3}{3\sin\theta\,(1+\cos\theta)} \tag{6-14}$$

And the drop surface area (A) as a function of drop wetted radius and contact angle is:

$$A = \frac{2\pi a^2}{1+\cos\theta} \tag{6-15}$$

Using Eqs. 4-2, 4-38, 6-11, 6-12, 6-14 and 6-15 and bearing in mind that $R = \frac{a}{\sin\theta}$, one may find the following relation for the wetted radius a as a function of time:

$$a^2 - {a_0}^2 = -4\frac{\rho^{\diamond} D}{\rho_L}\left(w^{\diamond}_{v\,eq} - w^{\diamond}_{v\,\infty}\right)\frac{\cos\theta + 1}{\cos\theta + 2}\zeta(\theta)t \tag{6-16}$$

where a_0 is the initial wetted radius. This equation can be used to find the evaporation time by setting $a = 0$ and solving for t. It should be mentioned that neglecting the evaporation flux variation along the drop surface one may find the following relation for the wetted radius [10, 37, 42]:

$$a^2 - {a_0}^2 = -4\frac{\rho^{\diamond} D}{\rho_L}(w^{\diamond}_{v\,eq} - w^{\diamond}_{v\,\infty})(\frac{\cos\theta + 1}{\cos\theta + 2})t \tag{6-17}$$

It should be noted that the wetted area change during the evaporation is useful for different applications *e.g.* in PEM fuel cells [43].

Table 6-1 The slope of a^2 versus t for evaporation of sessile water drop. Experimental values are compared with results from the model developed in this study Eq. 6-16.

Slope of a^2 versus t for evaporation of sessile water drops

	RH=60%, Temp.= 25°C, $\theta_{\text{evap}} = 100^0$	RH=53%, Temp.= 21°C, $\theta_{\text{evap}} = 108^0$
Experimental Values	5.55×10^{-10} [42]	$3.55 \pm 0.22 \times 10^{-10}$ [44]
Including the Evaporation flux Variation (Eq. 6-16)	5.21×10^{-10}	3.41×10^{-10}

Regarding the experimental results, the decrease rate of a^2 in t are reproduced using Graph Digitizer. Experimental conditions were: RH, temperature and $\theta_{R,\text{evap}}$ were 60%, 25°C and 100° in [42] and 53%, 21°C and 108° in [44].

6.3.1.2 Mode 2: Constant Wetted Area

Volume of a spherical cap drop can also be calculated as a function of the spherical cap height and wetted radius as:

$$V = \frac{\pi h}{6}(3a^2 + h^2) \tag{6-18}$$

and, the surface area as a function of the spherical cap height and wetted radius is:

$$A = \pi(a^2 + h^2) \tag{6-19}$$

Using Eqs. 4-2, 4-38, 6-10, 6-12, 6-18 and 6-19, one has:

$$\frac{1}{\sin\theta}\left(\frac{1}{1+\cos\theta}\right)\frac{1}{\zeta(\theta)}d\theta = -2\frac{\rho^{\diamond}D}{\rho_L}\frac{\left(w^{\diamond}_{v_{eq}} - w^{\diamond}_{v_{\infty}}\right)}{a^2}dt \tag{6-20}$$

Integration of Eq. 6-20 with respect to θ and t, gives:

$$\int_{\theta_i}^{\theta_f} \frac{1}{\sin\theta\,(1+\cos\theta)\zeta(\theta)}d\theta = -2\frac{\rho^{\diamond}D}{\rho_L}\frac{w^{\diamond}_{v_{eq}} - w^{\diamond}_{v_{\infty}}}{a^2}t \tag{6-21}$$

where θ_i and θ_f are the initial and final contact angles (at the beginning and end of evaporation). For finding the evaporation time, the relation in Eq. 6-21 should be solved.1

As shown in Eqs. 6-16 and 6-21, by knowing the evaporation mode, evaporation time of sessile drops can be calculated. However, the next challenge to be resolved is predicting the evaporation mode. This is further discussed in Chapter 7 (future works).

6.4 Comparing the Evaporation Rate at Different Modes

With a case study, it will be shown that evaporation is faster in CWA mode. Consider a water drop with wetted radius of $a = 1mm$, relative humidity of 20%, $w^{\circ}_{v\,eq} = 0.01789$, $\rho_L = 998.2kg/m^3$, $\rho = 1.097kg/m^3$ and $D = 2.04 \times 10^{-5}$. If this drop evaporates in mode 1 (*i.e.* CCA), and initial contact angle of $\theta_i = 40^o$, the evaporation time is $603.1\,s$ (using Eq. 6-16). If the same drop evaporates in mode 2 (*i.e.* CWA) the evaporation time is $447.4\,s$ (see Fig. 6-4).

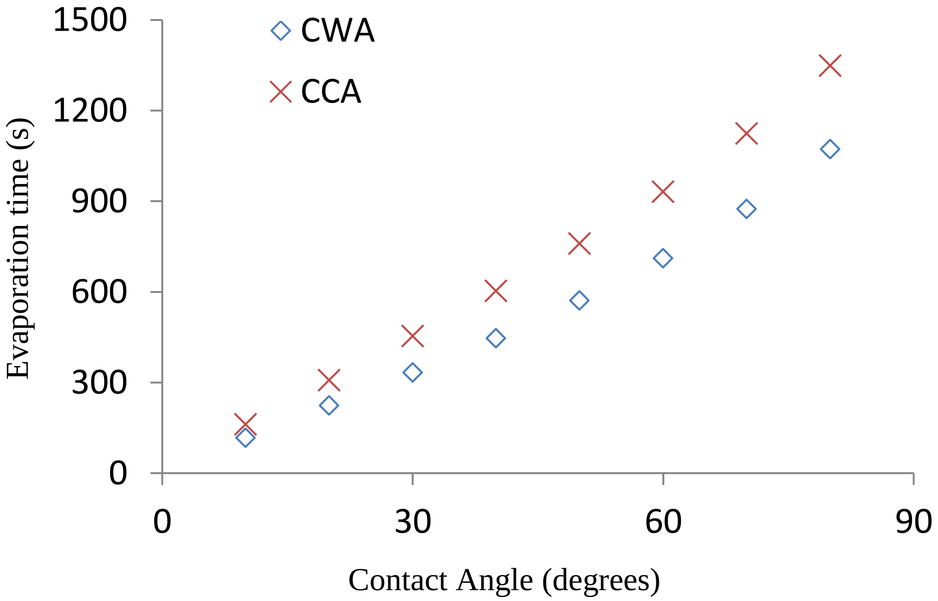

Fig. 6-5 Evaporation time of water drop with wetted radius of $a = 1mm$, relative humidity of 20%, $w^{\circ}_{v\,eq} = 0.01789$, $\rho_L = 998.2kg/m^3$, $\rho = 1.097kg/m^3$ and $D = 2.04 \times 10^{-5}$ at different contact angles and CWA and CCA modes is shown. Evaporation time is smaller in the CWA which means that evaporation is faster in that mode.

6.5 Conclusions

A model is suggested to describe the evaporation rate of micro-liter sessile drops in room condition. For such drops, evaporation is limited by movement of vapor from the drop surface to surrounding and not by the phase change. In chapter 4, evaporation of suspended drops was studied. For sessile drops, existence of a solid surface creates an uneven evaporation flux distribution along the drop surface. Using an electrostatic analogy (exterior Dirichlet) problem, evaporation variation along the drop surface was found. It was found that the ratio of the evaporation rate with including the evaporation flux variation to that with neglecting the evaporation flux variation is a function of contact angle, and can be found using the following exponential relation $60.27\theta^{-0.92}$ (θ is in radians). This relation can make the calculation of sessile drop evaporation very simple. In other words, one can assume uniform evaporation flux along the drop surface and calculate the evaporation, then multiply the value by $60.27\theta^{-0.92}$. It was found that for contact angles smaller and larger than 90 degrees, neglecting the evaporation variation along the drop surface results in underestimating and overestimating the evaporation rate, accordingly. Using the analogy problem; assuming spherical cap shapes for drops, two relations for finding the evaporation time are suggested. It was found that evaporation is faster in constant wetted area mode. The results of this study are in exact agreement with Picknett and Bexon which has used a different analogy problem *i.e.* finding the capacitance of equiconvex lens.

6.6 References

[1] Poulard, C., Guéna, G., and Cazabat, A., 2005, "Diffusion-Driven Evaporation of Sessile Drops," Journal of Physics Condensed Matter, **17**(49) pp. S4213-S4227.

[2] Maxwell, J.C., 1890, "Collected Scientific Papers,"Cambridge, pp. 628.

[3] Guéna, G., Poulard, C., and Cazabat, A., 2007, "The Leading Edge of Evaporating Droplets," Journal of Colloid and Interface Science, **312**(1) pp. 164-171.

[4] Guena, G., Poulard, C., and Cazabat, A., 2007, "The Dynamics of Evaporating Sessile Droplets," Colloid Journal, **69**(1) pp. 1-8.

[5] Langmuir, I., 1918, "The Evaporation of Small Spheres," Physical Review, **12**(5) pp. 368-370.

[6] Poulard, C., Guéna, G., Cazabat, A., 2005, "Rescaling the Dynamics of Evaporating Drops," Langmuir, **21**(18) pp. 8226-8233.

[7] Birdi, K. S., Vu, D. T., and Winter, A., 1989, "A Study of the Evaporation Rates of Small Water Drops Placed on a Solid Surface," Journal of Physical Chemistry, **93**(9) pp. 3702-3703.

[8] Fang, X., Li, B., Petersen, E., 2005, "Factors Controlling the Drop Evaporation Constant," Journal of Physical Chemistry B, **109**(43) pp. 20554-20557.

[9] Dunn, G. J., Wilson, S. K., Duffy, B. R., 2009, "The Strong Influence of Substrate Conductivity on Droplet Evaporation," Journal of Fluid Mechanics, **623**pp. 329-351.

[10] Erbil, H. Y., McHale, G., and Newton, M. I., 2002, "Drop Evaporation on Solid Surfaces: Constant Contact Angle Mode," Langmuir, **18**(7) pp. 2636-2641.

[11] Bourgès-Monnier, C., and Shanahan, M. E. R., 1995, "Influence of Evaporation on Contact Angle," Langmuir, **11**(7) pp. 2820-2829.

[12] Dhavaleswarapu, H. K., Migliaccio, C. P., Garimella, S. V., 2010, "Experimental Investigation of Evaporation from Low-Contact-Angle Sessile Droplets," Langmuir, **26**(2) pp. 880-888.

[13] Widjaja, E., and Harris, M. T., 2008, "Numerical Study of Vapor Phase-Diffusion Driven Sessile Drop Evaporation," Comput. Chem. Eng., **32**(10) pp. 2169-2178.

[14] Barash, L. Y., Bigioni, T. P., Vinokur, V. M., 2009, "Evaporation and Fluid Dynamics of a Sessile Drop of Capillary Size," Phys. Rev. E, **79**(4) .

[15] Xu, C., and Prince, J. L., 1998, "Snakes, Shapes, and Gradient Vector Flow," IEEE Transactions on Image Processing, **7**(3) pp. 359-369.

[16] Deegan, R. D., Bakajin, O., Dupont, T. F., 1997, "Capillary Flow as the Cause of Ring Stains from Dried Liquid Drops," Nature, **389**(6653) pp. 827-829.

[17] Jackson, J.D., 1998, "Classical Electrodynamics,"John Wiley& Sons Inc., pp. 75.

[18] Lebedev, N.N., 1965, "Special Functions and their Applications,"Prentice-Hall Inc., pp. 227.

[19] Berteloot, G., Pham, C. -., Daerr, A., 2008, "Evaporation-Induced Flow Near a Contact Line: Consequences on Coating and Contact Angle," EPL, **83**(1) .

[20] Deegan, R. D., Bakajin, O., Dupont, T. F., 2000, "Contact Line Deposits in an Evaporating Drop," Phys. Rev. E, **62**(1 B) pp. 756-765.

[21] Nguyen, T. A. H., and Nguyen, A. V., 2012, "On the Lifetime of Evaporating Sessile Droplets," Langmuir, **28**(3) pp. 1924-1930.

[22] Nguyen, T. A. H., Nguyen, A. V., Hampton, M. A., 2012, "Theoretical and Experimental Analysis of Droplet Evaporation on Solid Surfaces," Chemical Engineering Science, **69**(1) pp. 522-529.

[23] Prudnikov, A.P., and Brychkov, Y.A., 1992, "Integrals and Series," Gordon and Breach Science Publishers, USA, .

[24] Popov, Y. O., 2005, "Evaporative Deposition Patterns: Spatial Dimensions of the Deposit," Physical Review E - Statistical, Nonlinear, and Soft Matter Physics, **71**(3) pp. 036313/1-036313/17.

[25] Gelderblom, H., Marín, Á. G., Nair, H., 2011, "How Water Droplets Evaporate on a Superhydrophobic Substrate," Physical Review E - Statistical, Nonlinear, and Soft Matter Physics, **83**(2) .

[26] Sobac, B., and Brutin, D., 2011, "Triple-Line Behavior and Wettability Controlled by Nanocoated Substrates: Influence on Sessile Drop Evaporation," Langmuir, **27**(24) pp. 14999-15007.

[27] Hu, H., and Larson, R. G., 2002, "Evaporation of a Sessile Droplet on a Substrate," Journal of Physical Chemistry B, **106**(6) pp. 1334-1344.

[28] Semenov, S., Starov, V. M., Rubio, R. G., 2011, "Evaporation of Sessile Water Droplets: Universal Behaviour in Presence of Contact Angle Hysteresis," Colloids and Surfaces A: Physicochemical and Engineering Aspects, **391**(1-3) pp. 135-144.

[29] Deegan, R. D., 2000, "Pattern Formation in Drying Drops," Phy. Rev. E, **61**(1) pp. 475-485.

[30] Rowan, S. M., McHale, G., Newton, M. I., 1997, "Evaporation of Microdroplets of Three Alcohols," Journal of Physical Chemistry B, **101**(8) pp. 1265-1267.

[31] Picknett, R. G., and Bexon, R., 1977, "The Evaporation of Sessile Or Pendant Drops in Still Air," Journal of Colloid and Interface Science, **61**(2) pp. 336-350.

[32] Rowan, S. M., Newton, M. I., and McHale, G., 1995, "Evaporation of Microdroplets and the Wetting of Solid Surfaces," Journal of Physical Chemistry, **99**(35) pp. 13268-13271.

[33] Shanahan, M. E. R., and Bourgès, C., 1994, "Effects of Evaporation on Contact Angles on Polymer Surfaces," International Journal of Adhesion and Adhesives, **14**(3) pp. 201-205.

[34] Shin, D. H., Lee, S. H., Jung, J. -., 2009, "Evaporating Characteristics of Sessile Droplet on Hydrophobic and Hydrophilic Surfaces," Microelectronic Eng., **86**(4-6) pp. 1350-1353.

[35] Shi, L., Shen, P., Zhang, D., 2009, "Wetting and Evaporation Behaviors of Water-Ethanol Sessile Drops on PTFE Surfaces," Surface and Interface Analysis, **41**(12-13) pp. 951-955.

[36] Liu, C., Bonaccurso, E., and Butt, H., 2008, "Evaporation of Sessile Water/Ethanol Drops in a Controlled Environment," Phys. Chem. Chem. Phys., **10**(47) pp. 7150-7157.

[37] McHale, G., Rowan, S. M., Newton, M. I., 1998, "Evaporation and the Wetting of a Low-Energy Solid Surface," Journal of Physical Chemistry B, **102**(11) pp. 1964-1967.

[38] Song, H., Lee, Y., Jin, S., 2008, "Sessile drop evaporation on surfaces of various wettability," 2008 Proc. ASME Micro/Nanoscale Heat Transfer Int. Conf., MNHT 2008, Anonymous **PART A,** pp. 445-451.

[39] Soolaman, D. M., and Yu, H. Z., 2005, "Water Microdroplets on Molecularly Tailored Surfaces: Correlation between Wetting Hysteresis and Evaporation Mode Switching," Journal of Physical Chemistry B, **109**(38) pp. 17967-17973.

[40] Cioulachtjian, S., Launay, S., Boddaert, S., 2010, "Experimental Investigation of Water Drop Evaporation Under Moist Air Or Saturated Vapour Conditions," Int. J. Thermal Sci., **49**(6) pp. 859-866.

[41] Thomson, W., 1871, "On the Equilibrium of Vapour at a Curved Surface of Liquid," Philos. Mag., **42**(2) pp. 448-452.

[42] Furuta, T., Sakai, M., Isobe, T., 2009, "Evaporation Behavior of Microliter- and Sub-Nanoliter-Scale Water Droplets on Two Different Fluoroalkylsilane Coatings," Langmuir, **25**(20) pp. 11998-12001.

[43] Ous, T., and Arcoumanis, C., 2007, "Visualisation of Water Droplets during the Operation of PEM Fuel Cells," Journal of Power Sources, **173**(1) pp. 137-148.

[44] McHale, G., Aqil, S., Shirtcliffe, N. J., 2005, "Analysis of Droplet Evaporation on a Superhydrophobic Surface," Langmuir, **21**(24) pp. 11053-11060.

Chapter 7 – Conclusions and Future Work

7.0 Summary and Conclusions

In this thesis, drop removal from solid surfaces was studied. For removing a drop from its substrate, the adhesion force between the drop and substrate is needed. In Chapter 2, a model was developed to find the summation of surface tension forces along the contact line or the drop adhesion force in the direction parallel to the substrate. The developed model uses the side view images at different azimuthal angles, to reconstruct the contact line, and the surface tension distribution along the contact line. For non-circular contact lines, reconstructing the contact line introduces some perspective error. The developed model in Chapter 2 corrects this perspective error for any drop and contact line shape as long as there is no concave region on the contact line. As such, the developed model for calculating the summation of surface tensions or the adhesion force is applicable to any shape drop as long as contact line is convex everywhere. In Chapter 2, on a separate segment, the potential perspective error in measuring the contact angle due to the back to front tilt of the camera was discussed. A tilt angle of $4^o - 6^o$ is routine for capturing the contact points in the 2-D side view images. It was found that for 10^o back to front tilt of camera, the maximum contact angle measurement error will be less very small (less than 1^o). As such, correcting the contact angle value is not necessary.

The model developed in Chapter 2 requires the values of left and right contact angles for asymmetrical 2-D drop images. The challenge in contact angle measurements is for asymmetrical 2-D drop images. In Chapter 3, a method (*SPPF*) was developed to measure the contact angle of both symmetric and asymmetric drops for a wide range of contact angles. *SPPF* does not require any liquid property value and is suitable for automated computer implementations. *SPPF* fits a 2^{nd} order polynomial to the drop boundary (near the contact points) and calculates the contact angle as the slope of the fitted curve where it intersects the baseline. Drop boundary and contact points are found in sub-pixel resolutions. Since polynomials were unable to produce accurate results where contact angle was close to 90^{o}, for contact angles between 70^{o} and 110^{o}, *SPPF* rotates the drop boundary and calculates the contact angle with consideration for the rotation. With the above modification, the *SPPF* had a small error of less than 1^{o} in calculating the contact angle of synthetic (symmetric and asymmetric) drops over a wide range of contact angles between 10^{o} and 170^{o}. For naturally symmetric drops, the error for *SPPF* was determined as a relative value, *i.e.* the error was calculated with respect to the mean value of the contact angle values found using *ADSA* and FTÅ and ImageTool, to be less than 3^{o}. The error for *SPPF* when comparing to calibration slides (symmetric) or synthetic drops (symmetric and asymmetric) was less than 1^{o}. This error was lower than the error of all other methods. It should also be mentioned that short processing time (less than 1 second for every single image), usability for all ranges of contact angles, applicability to both symmetric and asymmetric drops and being fully automatic are the main advantages of the *SPPF*.

In some applications, removing the whole drop all at once is not needed, or applying an external load to shed the drop is not desired, *e.g.* printing industry. For such applications, evaporation in room condition can be solution. To minimize the number of factors affecting the evaporation of drops from solid surfaces, in Chapter 4, evaporation of suspended micro-liter drops was studied (existence of the substrate adds extra parameters to the problem). Evaporation of micro-liter drops in room temperature is restricted by movement of vapor from the drop surface, and not the phase change. The vapor movement can be decomposed into diffusion and convection (bulk movement of vapor). Literature studies assume the evaporation process is steady-state and convection is negligible (Maxwell assumptions). In Chapter 4, the Maxwell's assumptions were questioned. It was found that none of the two assumptions are valid. By relaxation of the two assumptions a transient and convective (TC) model was developed. By comparing the TC model with Maxwell based models, it was found that in the range of parameters for micro-liter drops, the effect of transient term cancels the effect of convection. As such, the Maxwell based models, which are easy to apply, produce accurate results. This is important as (i) some studies, for increasing the accuracy, relax either one of the steady-state or non-convective assumptions which may result in inaccurate results; (ii) for the range of variables where transient and convective effect do not cancel each other, the TC model rather than the Maxwell's model should be used.

The convection term discussed above excludes the buoyancy. As different liquids have different vapor weights, buoyance may potentially increase or decrease the convection and evaporation rate, consequently. In Chapter 5, it was found that buoyancy is not a dominant factor on evaporation of drops, for the studied system, and the difference between the evaporation of sessile and pendant drops has a different source. It was shown that iso-butanol which its vapor is heavier than air evaporates faster in sessile conformation. However, due to the buoyancy effect the pendant iso-butanol drop should have evaporated faster. This questions the hypothesis that buoyancy effect is significant. The cause of evaporation rate difference between sessile and pendant drops was found to be related to the evaporation modes. Evaporation occurs in CWA (constant wetted area) and CCA (constant contact angle) modes. Theoretically, it has been shown in literature that evaporation rate is faster in CWA mode [1]. It was found that sessile drops spend more time in the CWA mode compared to pendant drops (with %95 confidence and using t-test). This causes the sessile drops to evaporate faster than pendant drops and buoyancy is not the cause.

In Chapter 4, it was shown that for evaporation of micro-liter drops in a quiescent environment and at room temperature the effects of convective term and transient term cancel each other, and one can use a pure diffusive and steady-state equation to find the evaporation rate of micro-liter drops in room conditions. For sessile drops, existence of a solid surface creates an uneven evaporation flux distribution along the drop surface. The model developed in Chapter 6 included the substrate effect to the model developed in Chapter 4. Using an electrostatic analogy (exterior Dirichlet) problem, evaporation variation along the drop surface was found. It was found that the ratio of the evaporation rate with including the evaporation flux variation to that with neglecting the evaporation flux variation is a function of contact angle, and can be found using the following exponential relation $60.27\theta^{-0.92}$ (θ is in radians). This relation can make the calculation of sessile drop evaporation very simple. In other words, one can assume uniform evaporation flux along the drop surface and calculate the evaporation, then multiply the value by $60.27\theta^{-0.92}$. It was found that for contact angles smaller and larger than 90 degrees, neglecting the evaporation variation along the drop surface results in underestimating and overestimating the evaporation rate, accordingly. Assuming spherical cap shapes for drops, two relations for finding the evaporation time are suggested. One for the CWA mode and one for the CCA mode. The results of this study are in exact agreement with Picknett and Bexon [1] which has used a different analogy problem *i.e.* finding the capacitance of equi-convex lens.

7.1 Future Work

7.1.1 Surface Cooling

Surface cooling is the temperature decrease at the drop surface during the evaporation. In the models developed in Chapters 4 and 6, surface cooling was assumed to be small. As shown in [2], this may not be a valid assumption for some liquids *e.g.* methanol.

Figure 7-1 shows the importance of including the surface cooling in evaporation of methanol drops. Theoretically it can be shown that evaporation rate is slightly faster in CWA mode (*e.g.* Fig. 7-1b). As shown in Fig. 7-1a, evaporation of methanol from Teflon is faster in the CCA mode and decreases by ~2 orders of magnitude in the CWA mode. Methanol drop lost 79% of its weight in only 8% of its lifetime in the CCA mode (see Fig. 7-1a). In the CWA mode (where evaporation rate is expected to become larger [1]) evaporation rate becomes very small (see Fig. 7-1a). For water drops, as expected from the theory [1], evaporation rate was slightly faster in the CWA mode (see Fig. 7-1b). The change in the evaporation rate may support the idea that the drop surface cooling (loss of the surface temperature during evaporation) may play a role in evaporation of methanol drops. During the evaporation, temperature of methanol on its surface decrease. This would decrease the evaporation rate. This matter should be investigated further!

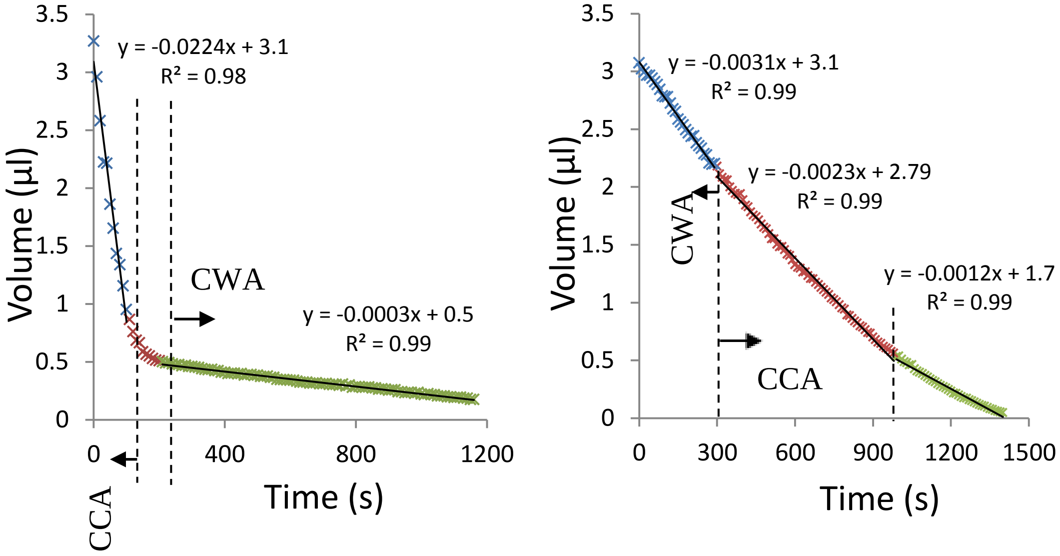

(a) (b)

Fig. 7-1 Volume change of (a) a methanol drop and (b) a water drop, during the evaporation from a Teflon surface is shown. Theoretically, it can be shown that evaporation rate is slightly higher in the CWA mode. Despite the theory results, for methanol, evaporation is slower in the CWA mode (by ~2 orders of magnitude). Surface cooling may be the cause.

7.1.2 Evaporation Modes

As mentioned in Chapter 6, predicting the evaporation mode is important in finding the evaporation time. According to [1, 3], evaporation of pure drops occurs in either one of the CWA and CCA modes. In this study, during the evaporation of methanol from PS coated silicon, a new evaporation mode was observed at which contact angle increased and wetted diameter decreased, see Fig. 7-2. This experiment was repeated 9 times for 3-5 μl methanol drops, and the same trend was observed. It should be mentioned that this mode does not fit into the evaporation modes suggested in literature *e.g.* [4], and never mentioned or observed for evaporation of pure drops in the open literature. This new mode opens a new avenue for evaporation of pure drops.

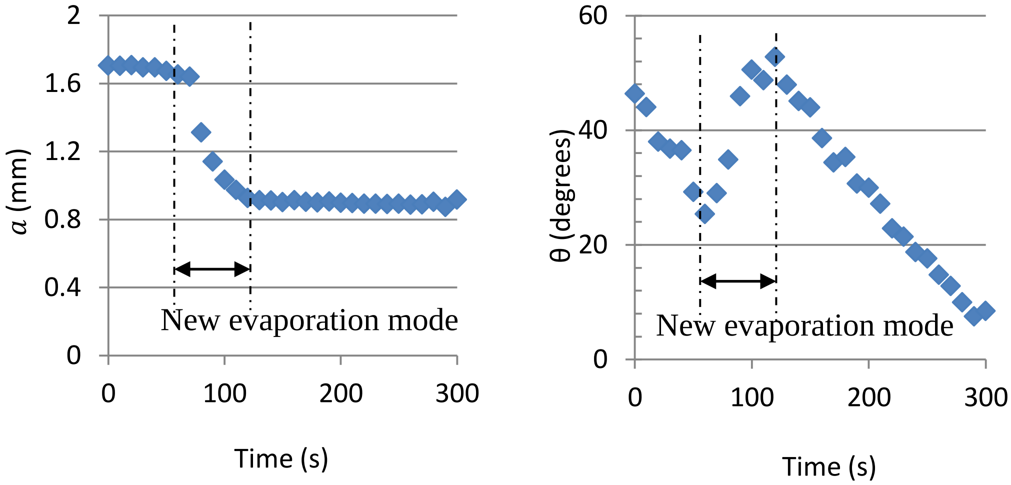

(a) (b)

Fig. 7-2 Change of (a) a and (b) θ during evaporation of a 4 μl methanol drop placed on a PS coated silicon surface is shown. Double sided arrows show a new evaporation mode at which wetted area decreases and contact angle increases.

Eevaporation mode usually switches from CWA mode to CCA mode and it is believed that θ_{evap} is equal to the θ_R, *e.g.*, or Fig. 7-3. However, during the evaporation of methanol from Teflon and PS surfaces, the opposite evaporation mode switch occurred *i.e*. CCA mode to CWA mode and θ_{evap} is equal to θ_A, see Fig. 7-4.

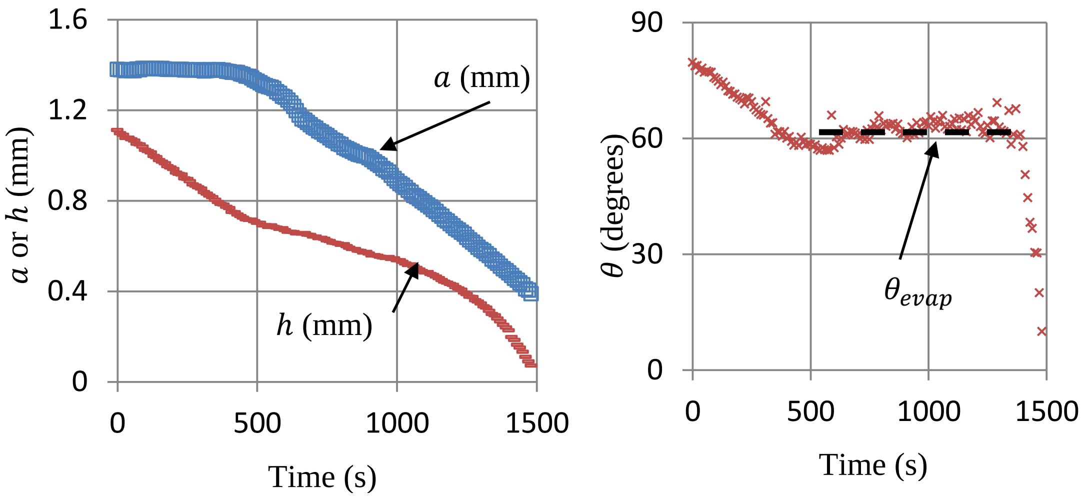

(a) (b)

Fig. 7-3 (a) Change of a, h, and (b) θ during the evaporation for a $4\mu l$ water drop placed on PMMA coated silicon surface is shown. θ_{evap} is the contact angle in mode 1.

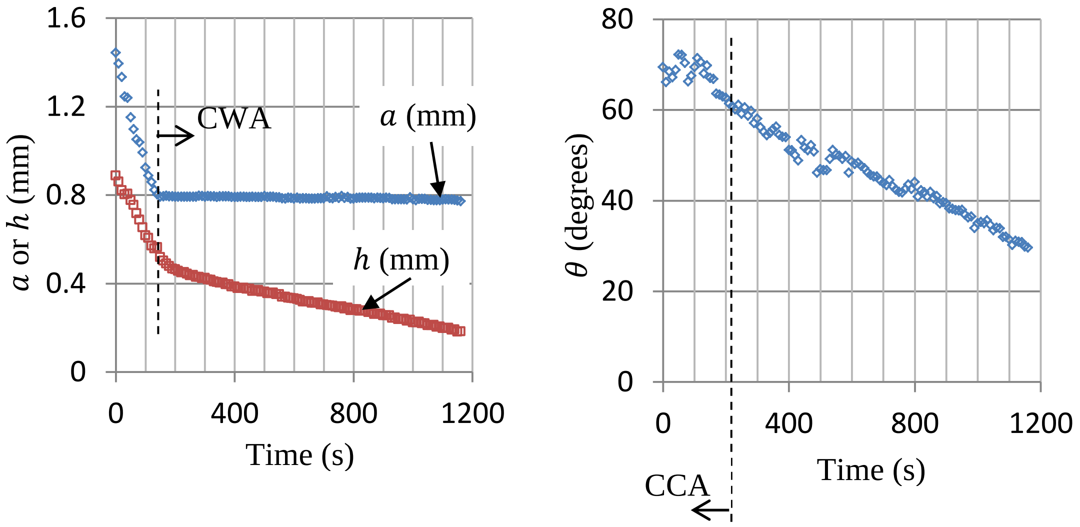

(a) (b)

Fig. 7-4 (a) Change of a, h, and (b) θ during the evaporation for a $4\mu l$ methanol drop placed on a Teflon coated silicon surface is shown.

A comprehensive study on evaporation modes and the physical elements affecting the evaporation mode is lacking in the literature. As shown in Chapter 6, this is important in predicting the evaporation rate of sessile drops.

7.3 References

[1] Picknett, R. G., and Bexon, R., 1977, "The Evaporation of Sessile or Pendant Drops in Still Air," Journal of Colloid and Interface Science, **61**(2) pp. 336-350.

[2] Erbil, H. Y., McHale, G., and Newton, M. I., 2002, "Drop Evaporation on Solid Surfaces: Constant Contact Angle Mode," Langmuir, **18**(7) pp. 2636-2641.

[3] Ous, T., and Arcoumanis, C., 2007, "Visualisation of Water Droplets during the Operation of PEM Fuel Cells," Journal of Power Sources, **173**(1) pp. 137-148.

[4] Kulinich, S. A., and Farzaneh, M., 2009, "Effect of Contact Angle Hysteresis on Water Droplet Evaporation from Super-Hydrophobic Surfaces," Applied Surface Science, **255**(7) pp. 4056-4060.